

The Broad-band X-ray spectra of heavily obscured AGN

Thesis submitted for the degree of
Doctor of Philosophy
at the University of Leicester.

by

Robert Gareth Griffiths
X-ray Astronomy Group
Department of Physics and Astronomy
University of Leicester

September 1999

UMI Number: U594557

All rights reserved

INFORMATION TO ALL USERS

The quality of this reproduction is dependent upon the quality of the copy submitted.

In the unlikely event that the author did not send a complete manuscript and there are missing pages, these will be noted. Also, if material had to be removed, a note will indicate the deletion.



UMI U594557

Published by ProQuest LLC 2013. Copyright in the Dissertation held by the Author.
Microform Edition © ProQuest LLC.

All rights reserved. This work is protected against
unauthorized copying under Title 17, United States Code.



ProQuest LLC
789 East Eisenhower Parkway
P.O. Box 1346
Ann Arbor, MI 48106-1346

Declaration

I hereby declare that no part of this thesis has been previously submitted to this or any other University as part of the requirement for a higher degree. The work described herein was conducted by the undersigned except for contributions from colleagues as acknowledged in the text.

Robert Gareth Griffiths,
September 1999

Acknowledgements

My greatest thanks must go to my supervisor, Bob Warwick, for all his support and guidance throughout my four years as a postgraduate student, and especially for his encouragement over the last few months without which this thesis would have taken even longer to write. I would also like to thank Dave Smith for “showing me the ropes” when I first came to Leicester and Ioannis Georgantopoulos, Chris Done and Tahir Yaqoob for collaborating with me. Thanks also to all my friends here at Leicester University that made the last four years here very enjoyable.

Diolch i mam a dad am bobeth, heb y cymorth, y caredigrwydd a'r cariad y cefais ganddynt hwy ar hyd fy oes fyswn i ddim wedi mynd mor bell ac yr ydw i heddiw. Diolch hefyd i Bethan a Nia am eu cefnogaeth yn ystod y bedair blynedd diwethaf. Yn olaf, diolch i Delyth, y person sydd wedi bod gyda'r cychwyn hyd at y diwedd. Diolch i ti Delyth am ddioddef y nosweithiau hwyr a'r penwythnosau unig yn ystod y flwyddyn diwethaf ac am fy nghroesawu adref bob nos gyda gwen a chusan. Yn sicr, ti yw'r person sydd wedi fy ngalleuogi i gwblhau'r thesis yma.

The Broad-band X-ray spectra of heavily obscured AGN

Robert Gareth Griffiths

ABSTRACT

This thesis presents a study of heavily obscured AGN using data from the *Ginga*, *ASCA* and *ROSAT* X-ray observatories. Chapter 1 provides a brief introduction into the classification of AGN, the Seyfert Unification Theory, the X-ray properties of Seyfert galaxies and possible emission mechanisms that occur in these objects. This is followed by a short discussion of the performance characteristics of the instruments on-board the observatories mentioned above (chapter 2). Chapter 3 focuses on the X-ray properties of the well-known Seyfert 2 galaxy Mrk 3. The utilization of *non-simultaneous Ginga*, *ASCA* and *ROSAT* observations allows the broad-band (0.1- 30.0 keV) X-ray spectrum of this object to be investigated, including the slope and level of the hard continuum, the presence of Compton reflection, iron K_{α} emission and the relatively complex soft X-ray spectrum which comprises an emission feature near 0.9 keV. Following on from this, *non-simultaneous Ginga* and *ASCA* observations are employed to analyse the mid-hard X-ray spectrum of a sample of five heavily obscured (with column density $N_H \gtrsim 10^{23} \text{ cm}^{-2}$) Seyfert 2 galaxies (chapter 4). The main result of these investigations is evidence for large variations in the line-of-sight gas column density in three out of the five objects. The X-ray spectrum of the Seyfert 1.5 galaxy NGC 4151 is also considered in this chapter. Multiple *ASCA* observations of this source show that the X-ray continuum, in the 1-7 keV band, varies with time in a confusing manner that can only be explained as an effect of the complex absorption that is present in the spectrum. A sharp emission feature present in the X-ray spectrum of NGC 4151 at 0.9 keV is investigated in chapter 5. Using models produced by the photoionization code *XSTAR*, this feature is explained as recombination of free electrons directly into the ground state of fully ionized oxygen. In addition, evidence for a feature at 0.9 keV is found for Mrk 348, NGC 4507 and NGC 7582. Chapter 6 discusses the potential of future X-ray satellites such as *Chandra*, *ASTRO-E* and in more detail *XMM* to further the investigations carried out in this thesis.

Publications

A significant amount of the work contained in this thesis has been published elsewhere as:

Griffiths, R.G., Warwick, R.S., Georgantopoulos I., Done C., Smith D.A., 1998, *Mon. Not. R. Ast. Soc.*, **298**, 1159

"The broad-band X-ray spectrum of Mrk 3"

Warwick, R.S., Griffiths R.G., 1998, *Proc. of the First XMM Workshop*, Dahlem, M., eds.

"O VIII Recombination Features in AGN Spectra"

I Mam a Dad

Diolch

Contents

1	Introduction	1
1.1	Classification of AGN	2
1.1.1	Seyferts	4
1.1.2	Quasars	4
1.1.3	NELGs	5
1.1.4	LINERs	5
1.1.5	Radio Loud Objects	5
1.2	Seyfert Unification Theory	6
1.3	X-ray properties of Seyferts	8
1.3.1	The hard X-ray spectrum	8
1.3.2	The soft X-ray spectrum	11
1.4	X-ray emission mechanisms	12
2	Instrumentation and Data Reduction	15
2.1	<i>Ginga</i>	15
2.1.1	The LAC	15
2.1.2	Data Reduction	17
2.2	<i>ROSAT</i>	17

2.2.1	The PSPC	17
2.2.2	The HRI	19
2.3	ASCA	19
2.3.1	GIS	20
2.3.2	SIS	20
2.3.3	Standard Analysis Procedure	23
3	The broad-band X-ray spectrum of a typical Seyfert 2 galaxy: the case of Mrk 3	26
3.1	Introduction	26
3.2	Observations and Data Reduction	28
3.2.1	The <i>Ginga</i> observations	28
3.2.2	The ASCA observations	28
3.2.3	The <i>ROSAT</i> observations	28
3.3	Spectral Analysis	29
3.3.1	The <i>Ginga</i> spectra	29
3.3.2	The ASCA spectra	31
3.3.3	The composite <i>Ginga</i> , ASCA and <i>ROSAT</i> spectra	34
3.4	Discussion	42
3.4.1	Characteristics of the hard X-ray spectrum of Mrk 3	42
3.4.2	The nature of the soft X-ray emission in Mrk 3	45
4	A sample of heavily obscured Seyfert 2 galaxies	49
4.1	Introduction	49
4.2	Spectral analysis of the Seyfert 2 galaxies	50
4.2.1	The <i>Ginga</i> spectra	50

4.2.2	The <i>ASCA</i> spectra	51
4.2.3	The composite <i>Ginga</i> and <i>ASCA</i> spectra	57
4.2.4	Discussion	65
4.3	The complex absorption in NGC 4151	70
4.3.1	Data Analysis	71
4.3.2	Discussion	74
5	Photoionization in Seyfert galaxies	78
5.1	Introduction	78
5.2	The Photoionization code XSTAR	79
5.2.1	Ionization processes	80
5.2.2	Recombination processes	81
5.2.3	Heating processes	81
5.2.4	Cooling processes	82
5.2.5	XSTAR input parameters	82
5.2.6	XSTAR output	84
5.3	The soft X-ray spectrum of NGC 4151	89
5.4	Discussion	95
5.5	Soft X-ray features in Seyfert 2 galaxies	102
6	Future Prospects with XMM	106
6.1	XMM	106
6.1.1	EPIC	107
6.1.2	RGS	107
6.1.3	Chandra	108

6.1.4	ASTRO-E	109
6.2	Future Work with <i>XMM</i>	110
6.2.1	Is O VIII recombination a prominent feature in the soft X-ray spectrum of Seyfert 2 galaxies?	110
6.2.2	What is the temperature of the photoionized scattering medium?	110
6.2.3	The nature of the complex absorption in NGC 4151.	112
6.2.4	The hard X-ray spectrum of Seyfert 2 galaxies.	115
7	Conclusions	118
7.1	Mrk 3	118
7.2	The sample of Seyfert 2 galaxies	119
7.3	NGC 4151	120
	References	122

List of Figures

1.1	The Spectral Energy Distribution of the radio-quiet AGN Seyfert 1 galaxy NGC 3783 (Alloin <i>et al.</i> 1995) and a typical normal galaxy (Elvis <i>et al.</i> 1994) taken from “An introduction to active galactic nuclei” (Peterson 1997).	2
1.2	Optical spectrum of a normal galaxy taken from “Exploring the X-ray Universe” by Charles & Seward (1995). Intensity is plotted against wavelength in nanometers	3
1.3	Optical Spectrum of a Seyfert 1 galaxy (NGC 3227) taken from “Astrophysics of Gaseous Nebulae and Active Galactic Nuclei” by Osterbrock (1989)	3
1.4	The Seyfert Unification Model: A diagram of the nucleus in Seyfert galaxies. Shown are different orientations of the molecular torus with respect to the observer’s line-of-sight when viewing type I and II galaxies.	7
1.5	The Fe K_{α} line profile in MCG-6-30-15 (from Tanaka <i>et al.</i> 1995) and the best-fit model prediction from an accretion disk orbiting a Schwarzschild black hole (Fabian <i>et al.</i> 1989).	10
2.1	The <i>Ginga</i> satellite	16
2.2	The effective area of the <i>Ginga</i> “top-” (solid curve) and “mid-layer” (dashed curve) in the 1-20 keV band.	16
2.3	A schematic of the <i>ROSAT</i> satellite and its instruments.	18
2.4	The <i>ASCA</i> satellite.	20
2.5	The Effective area of one XRT+GIS for different off-axis(θ) and azimuthal (ϕ) angles.	21
2.6	The Effective area of one XRT+SIS at the nominal pointing positions for three different clocking (CCD) modes.	22

3.1	Top panel: The <i>Ginga</i> LAC top-layer (triangles) and mid-layer (circles) count rate spectra for Mrk 3. The solid line corresponds to the best fitting version of Model 1. Bottom panel: The spectral fitting residuals to the <i>Ginga</i> data for Mrk 3 (scaled in terms of the measurement errors).	32
3.2	Top panel: The unfolded composite spectrum of Mrk 3 based on the best-fitting version of Model 3. Bottom panel: The spectral fitting residuals to the composite spectrum for Mrk 3. The data points correspond to <i>Ginga</i> top-layer (circles), <i>Ginga</i> mid-layer (squares), <i>ASCA</i> SIS-0 (crosses) and <i>ROSAT</i> PSPC (triangles). For clarity only the <i>ASCA</i> SIS-0 points are shown.	37
3.3	Modelling of the soft X-ray (0.3–3 keV) spectrum of Mrk 3. (a) As a blend of a soft (scattered) power-law continuum with a ~ 0.7 keV Raymond-Smith component. The spectrum from 0.7–0.9 keV is dominated by O, Fe (L shell) and Ne lines. (b) As an absorbed continuum scattered from a hot photoionized medium plus line emission from the same region. The feature near 0.9 keV is due to O VIII recombination and that at 0.65 keV corresponds to the O VIII L_α line.	40
3.4	Relative fractional abundance for different ionization states of iron in a photoionized medium where $\log \xi \sim 2.8$ and $N_{H_{\text{scat}}} \sim 1.7 \times 10^{23} \text{ cm}^{-2}$	41
4.1	Confidence contours for the photon index (Γ) and column density (N_H) parameters. The contours correspond to $\Delta\chi^2 = 2.30, 4.61$ and 9.21 which is 68, 90 and 99 percent confidence respectively for two interesting parameters. Black, red and green contours represent <i>Ginga</i> , <i>ASCA</i> (1) and <i>ASCA</i> (2) data respectively. . .	56
4.2	The spectral fitting residuals to the composite <i>Ginga</i> / <i>ASCA</i> spectrum for a) Mrk 348, b) NGC 4507, c) ESO 103-G35, d) IC 5063 and e) NGC 7172 using Model 3a but with the column density fixed at the best-fit value obtained by <i>ASCA</i> data alone. The data points correspond to <i>Ginga</i> top-layer (red squares), <i>ASCA</i> (1) SIS-0 (black circles) and <i>ASCA</i> (2) SIS-0 (green stars). Note the large discrepancy between the <i>Ginga</i> and <i>ASCA</i> data for Mrk 348, NGC 4507 and NGC 7172. . . .	59
4.3	The strength of the Fe- K_α line versus the continuum level at the line energy. The solid straight lines are lines of constant EW.	64
4.4	Column density variability for a cloud of gas moving across the line-of-sight to the central X-ray source.	67
4.5	The measured cold column density of a gas with differing ionization parameters. The actual column density of the gas is $2 \times 10^{23} \text{ cm}^{-2}$. The horizontal dotted lines represent the line-of-sight column measured in Mrk 348 by <i>Ginga</i> and <i>ASCA</i> (see Table 4.6).	70
4.6	The best-fit dual-absorber model descriptions for all four <i>ASCA</i> spectra of NGC 4151.	75

4.7	The softness ratios soft1 (crosses) and soft2 (stars) for NGC 4151 with respect to the hard continuum level. See text for definitions of ratios	75
4.8	N_H variability in the stratified warm absorber model.	76
5.1	Ionization processes	80
5.2	The assumed spectral shape of the central ionizing source (from Krolik & Kriss 1995).	83
5.3	Radiative equilibrium curves, produced from the output of XSTAR, of Ξ (left panel) and ξ (right panel) versus T_{warm} for a gas of density $n = 10^6 \text{ cm}^{-3}$ and column $N_H = 10^{23} \text{ cm}^{-2}$. Note that Ξ is a version of the ionization parameter involving the pressure in the photoionized gas and is proportional to $\frac{\xi}{T_{warm}}$	86
5.4	The scattered and intrinsic emission from a photoionized gas (shown respectively as the red and black components). The four panels correspond to $\log \xi$ of (a) 4.0; (b) 3.0; (c) 2.5; (d) 2.0.	88
5.5	The best-fit input spectrum (upper panel) and corresponding count rate residuals (lower panel) to the S0 (filled squares) and S1 (open circles) spectra of NGC 4151 using Model 1.	90
5.6	The best-fit input spectrum (upper panel) and corresponding count rate residuals (lower panel) to the SIS spectra of NGC 4151 using Model 3b.	91
5.7	The best-fit input spectrum (upper panel) and corresponding count rate residuals (lower panel) to the SIS spectra of NGC 4151 using Model 5.	92
5.8	The best-fit input spectrum (upper panel) and corresponding count rate residuals (lower panel) to the SIS spectra of NGC 4151 using Model 6.	93
5.9	For comparison, plots of Models 4(top), 5(middle) and 6(bottom) in the 0.7-10.0 keV band.	94
5.10	The two-phase model in which clouds of relatively cool gas are immersed in pressure equilibrium with a much hotter plasma.	99
5.11	A model consisting of two separate regions, a hot fully ionized inner region and a cooler outer region.	100
5.12	Residuals for PV1 (open squares), PV2 (filled triangles), AO1 (open circles) and AO4 (stars) data when compared to Model 6.	101
5.13	Ratio plot of the data compared the ‘scatter power-law’ model for each object. The data points correspond to <i>Ginga</i> top-layer (open circles), <i>Ginga</i> mid-layer (filled squares) and combined ASCA SIS0+SIS1 (stars).	103

6.1	The effective area of various instruments between 0.1-20.0 keV: EPIC pn (solid curve), <i>Ginga</i> (dashed curve), <i>ASCA</i> SIS (dash-dot curve) and <i>ROSAT</i> PSPC (dot curve).	108
6.2	A 100 ks simulated RGS spectrum for Mrk 3 using either a scattered power-law continuum plus a Raymond-Smith thermal plasma component (Model 4; § 3.3.3) or scattered plus intrinsic emission from a photoionized plasma (Model 5; § 3.3.3). 111	
6.3	40 ks EPIC pn and RGS simulations for NGC 4151. See text for details of model. 112	
6.4	Variation in the χ^2 residuals with respect to the best-fit value as a function of electron temperature for both the EPIC-pn (solid curve) and RGS (dashed curve) data. The dotted vertical line represents the actual temperature used in Model 4 to fake the <i>XMM</i> data.	113
6.5	Top panel: The unfolded EPIC pn spectrum of NGC 4151 between 1.5-10.0 keV (created from the dual-absorber model) and the corresponding best-fit description using the warm-absorber model. Bottom panel: The ratio of the data to the model. 114	
6.6	The competing descriptions of the hard X-ray spectrum of Mrk 3: the Turner <i>et al.</i> (1997b) model (upper panel) and Model 6 (lower panel). Both models consist of a heavily absorbed hard power-law (red curve), a reflection component (green curve), Fe K_α emission (light blue curve) and a soft power-law (dark blue curve).	117

List of Tables

2.1	Degradation of the energy resolution of SIS-1 in 1-CCD mode	21
2.2	Observation log	25
3.1	Spectral fitting of the <i>Ginga</i> data alone	30
3.2	Spectral fitting of the <i>ASCA</i> SIS/GIS data alone	33
3.3	Spectral fitting of the composite <i>Ginga</i> , <i>ASCA</i> and <i>ROSAT</i> spectra for Mrk 3	36
4.1	Model 1 fit to <i>Ginga</i> data	52
4.2	Model 2 fit to <i>Ginga</i> data	52
4.3	Model 1 fit to <i>ASCA</i> SIS/GIS data	54
4.4	Model 3 fit to <i>ASCA</i> SIS/GIS data	55
4.5	Spectral fitting of the composite <i>Ginga</i> and <i>ASCA</i> spectra: Model 3a	60
4.6	Spectral fitting of the composite <i>Ginga</i> and <i>ASCA</i> spectra: Model 3b	61
4.7	Spectral fitting of the composite <i>Ginga</i> and <i>ASCA</i> spectra: Model 3c	62
4.8	Spectral fitting of the composite <i>Ginga</i> and <i>ASCA</i> spectra: Model 3d	63
4.9	The width of the Fe K_{α} emission line	63
4.10	Spectral fitting of the composite <i>Ginga</i> and <i>ASCA</i> spectra: Compton reflection	64
4.11	Estimates on the density, size and distance of an obscuring cloud moving into and out of the line-of-sight to the central X-ray source.	66
4.12	The best-fit parameters of the hard X-ray spectrum of NGC4151 using multi-absorber models	73

4.13	The best-fit parameters of the hard X-ray spectrum of NGC4151 using a warm absorber model.	74
5.1	The element abundances used in XSTAR	84
5.2	Spectral fitting of the SIS spectra of NGC 4151	96
5.3	Parameterisation of the 0.9 keV feature in Seyfert 2 galaxies.	104
5.4	The best-fit ionization parameter and column density of the photoionized gas. . .	105

Chapter 1

Introduction

The total energy output of normal galaxies can be attributed to the stars that inhabit them. They emit nearly all of their power in the visible part of the electromagnetic spectrum. Some galaxies, however, contain Active Galactic Nuclei (AGN) which are up to a thousand times more luminous (bolometric luminosity $L \sim 10^{41} - 10^{48} \text{ erg s}^{-1}$) than normal galaxies. From the variability observed in many AGN, this luminosity is known to emanate from a region smaller than 1 pc in diameter. Furthermore, the Spectral Energy Distribution (SED) of these galaxies show that they are powerful emitters across the whole electromagnetic spectrum, from radio waves through to γ rays (see Figure 1.1). Such vast amounts of energy cannot be accounted for by the typical number of stars, supernovae, X-ray binaries etc. that are present in normal galaxies. Optical spectra also show major differences between normal galaxies (Fig 1.2) and AGN (Fig 1.3). Optical spectra of normal galaxies contain stellar absorption lines and narrow emission lines whereas the emission lines in AGN are strong and often broad.

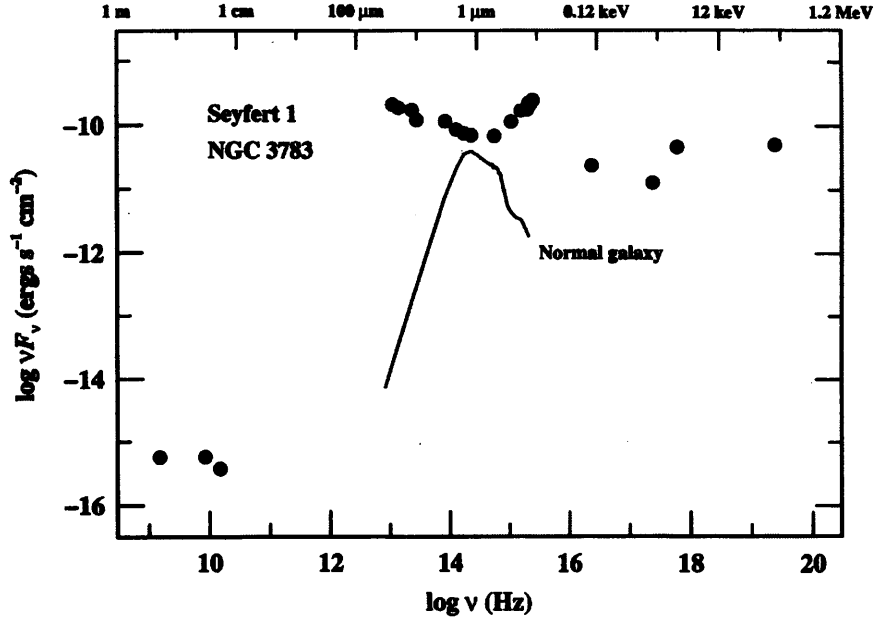


Figure 1.1: The Spectral Energy Distribution of the radio-quiet AGN Seyfert 1 galaxy NGC 3783 (Alloin *et al.* 1995) and a typical normal galaxy (Elvis *et al.* 1994) taken from “An introduction to active galactic nuclei” (Peterson 1997).

The term AGN covers a broad range of objects which have several different properties and are, therefore, subdivided into a multitude of classes and types. However, these classes are not distinct and a large amount of overlap is observed between them. The next section briefly covers most of these classes and highlights the main differences and similarities between them.

1.1 Classification of AGN

One of the major properties used to classify AGN is radio power. Nearly all of the objects discussed in this thesis are Seyfert galaxies which are known to be radio-quiet. The majority of quasars are also radio-quiet, with ~ 10 percent of them being radio-loud. Therefore, different classes of radio quiet objects are considered first followed by a brief discussion of radio-loud AGN.

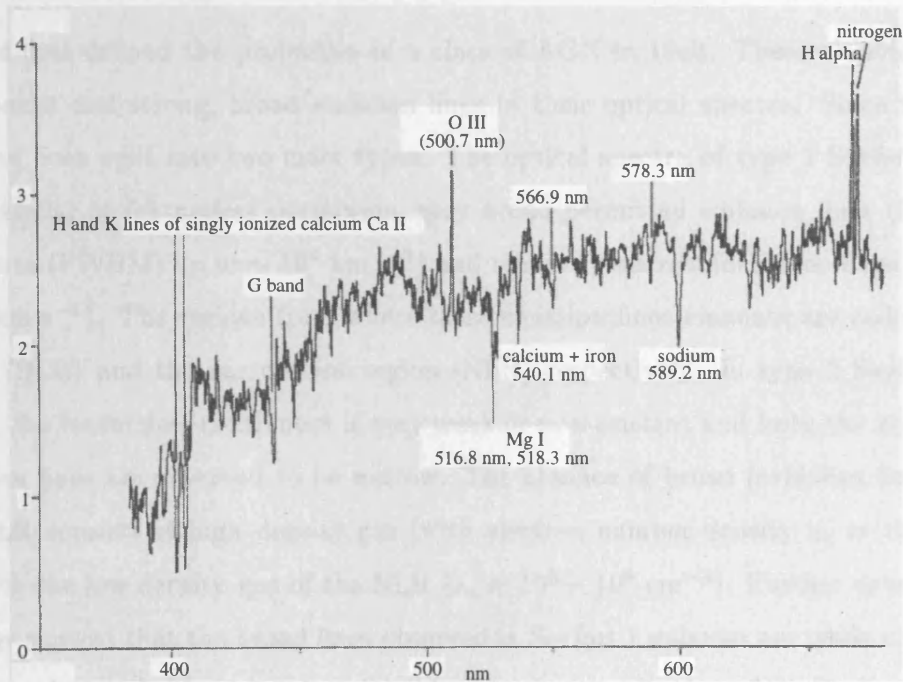


Figure 1.2: Optical spectrum of a normal galaxy taken from “Exploring the X-ray Universe” by Charles & Seward (1995). Intensity is plotted against wavelength in nanometers

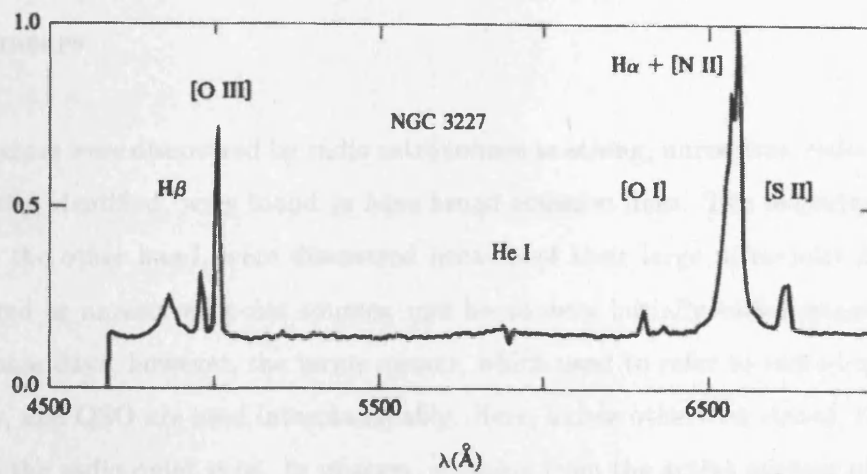


Figure 1.3: Optical Spectrum of a Seyfert 1 galaxy (NGC 3227) taken from “Astrophysics of Gaseous Nebulae and Active Galactic Nuclei” by Osterbrock (1989)

1.1.1 Seyferts

Carl Seyfert first defined the properties of a class of AGN in 1943. These objects had bright point-like nuclei and strong, broad emission lines in their optical spectra. Since then Seyfert galaxies have been split into two main types. The optical spectra of type 1 Seyferts contain a strong non-stellar or featureless continuum, very broad permitted emission lines (full width at half maximum (FWHM) up to $\sim 10^4 \text{ km s}^{-1}$) and relatively narrow forbidden lines (FWHM up to $\sim 1000 \text{ km s}^{-1}$). The regions from where these emission lines emanate are called the broad line region (BLR) and the narrow line region (NLR) respectively. In type 2 Seyferts, on the other hand, the featureless continuum is very weak or non-existent and both the permitted and the forbidden lines are observed to be narrow. The absence of broad forbidden lines indicates that the BLR consists of high density gas (with electron number density $n_e \approx 10^9 \text{ cm}^{-3}$), in contrast with the low density gas of the NLR ($n_e \approx 10^3 - 10^6 \text{ cm}^{-3}$). Further developments in spectroscopy showed that the broad lines observed in Seyfert 1 galaxies are made up of a strong narrow core and a weaker broad pedestal and lead to the introduction of the Seyfert 1.5, 1.8 and 1.9 classification. These classifications are based upon the properties of the Balmer emission lines $H\alpha$ and $H\beta$. In a Seyfert 1.5 galaxy, the broad and narrow components are easily detected in both $H\alpha$ and $H\beta$. The broad component of $H\beta$ is very weak while that of $H\alpha$ is clearly visible in a Seyfert 1.8, whereas for a Seyferts 1.9 the broad component is observed in $H\alpha$ only.

1.1.2 Quasars

The first quasars were discovered by radio astronomers as strong, unresolved radio sources which, when optically identified, were found to have broad emission lines. The majority of radio-quiet quasars, on the other hand, were discovered because of their large ultraviolet flux. Optically, they appeared as unresolved point sources, and hence were initially called quasi-stellar objects (QSOs). These days, however, the terms quasar, which used to refer to radio-loud quasi-stellar objects only, and QSO are used interchangeably. Here, unless otherwise stated, the term quasar will refer to the radio-quiet type. In quasars, emission from the active nucleus often appears to completely swamp the host galaxy, although more recent observations have shown that a faint halo or fuzz sutrounds many of them. The broad lines present in the optical spectra of these objects were found to be hugely redshifted, indicating that quasars are the most distant and

therefore luminous ($M_B < -23.0$, assuming that $H_0 = 50 \text{ km s}^{-1} \text{ Mpc}^{-1}$) objects in the Universe. The optical spectra of quasars and Seyfert 1 galaxies are very similar. It seems that quasars are the luminous counterparts of Seyfert 1s, indeed there is a large degree of overlap between the brightest Seyfert 1s and the faintest quasars.

1.1.3 NELGs

Narrow Emission Line Galaxies (NELGs), also known as Narrow Line X-ray Galaxies (NLXGs) are a group of galaxies which were initially discovered in the early X-ray sky surveys. While many of these newly found X-ray sources were optically identified as Seyfert 1s, there were several which had only narrow highly-ionized emission lines (Ward *et al.* 1978), very much like Seyfert 2 galaxies. The X-ray properties of NELGs and Seyfert 2s are also very similar, hence the term “Seyfert 2 galaxies” very often includes NELGs.

1.1.4 LINERs

Low Ionization Nuclear Emission line Regions (LINERs) are thought to be low-luminosity AGN. Their optical spectra are similar to Seyfert 2s in that they contain strong narrow emission lines, however, the low-ionization lines (e.g. [O I] $\lambda 6300$) are relatively strong compared to the high-ionization lines (e.g. [O III] $\lambda\lambda 4959, 5007$), in contrast to that observed in Seyferts.

1.1.5 Radio Loud Objects

Broad Line Radio Galaxies (BLRGs) and Narrow Line Radio Galaxies (NLRGs) form the radio-loud analogue to the radio-quiet Seyfert 1s and Seyfert 2s respectively. The major difference between these objects and Seyferts, apart from the radio power, is morphological. The majority of Seyferts reside in spiral galaxies whereas radio galaxies generally inhabit ellipticals.

The term blazar covers two types of radio-loud AGN which have unusual or extreme properties. They are BL Lacs and optically violent variable quasars (OVVs). BL Lacs possess a featureless (i.e. no strong emission or absorption lines) continuum spectrum which shows strong polarization and rapid variability. The continuum emission is clearly synchrotron, rising steeply from the

X-ray to infrared with a power-law form and then flattening out into the radio. It is thought that the line-of-sight to these objects is along or close to the axis of a relativistic jet. OVV's have very similar properties to BL Lacs, the major difference being that OVV's have very broad and strong optical emission lines.

1.2 Seyfert Unification Theory

Current unification models claim that the active nuclei in both Seyferts 1 and 2 galaxies are intrinsically the same object. The difference in observational properties are explained as primarily due to obscuration and orientation effects (e.g. Figure 1.4; see Antonucci 1993 for a detailed review on unified models). All AGN are thought to comprise of the following main components:

- a super-massive black hole of order $\sim 10^5 - 10^9 M_{\odot}$.
- an accretion disk.
- a broad-line region (BLR).
- a geometrically and optically thick molecular torus.
- a narrow-line region (NLR).

The enormous amount of energy produced in AGN is attributed to the release of gravitational energy from the accretion of matter onto a super-massive black hole (Rees 1984). There is plenty of indirect evidence for the existence of such objects. For example, HST observations showed that the gas in the central region of M87 is rotating in a keplerian orbit about a central mass $M \sim 2.4 \times 10^9 M_{\odot}$ (Ford *et al.* 1994; Harms *et al.* 1994). A disk structure is the preferred geometry for the accreting material since spherical accretion is inefficient at releasing gravitational energy and the accreting material is likely to have some angular momentum. Observational evidence for such a disk was obtained when the spectra of several Seyfert 1 galaxies and Quasars showed a flattening of their continua in the blue part of the optical spectrum, known as the “big blue bump” (Shields 1978; Malkan & Sargent 1982). This UV excess was well described by simple blackbody emission and interpreted as thermal emission from an accretion disk. Further work to produce more realistic models has been carried out by several authors (Sun & Malkan 1989;

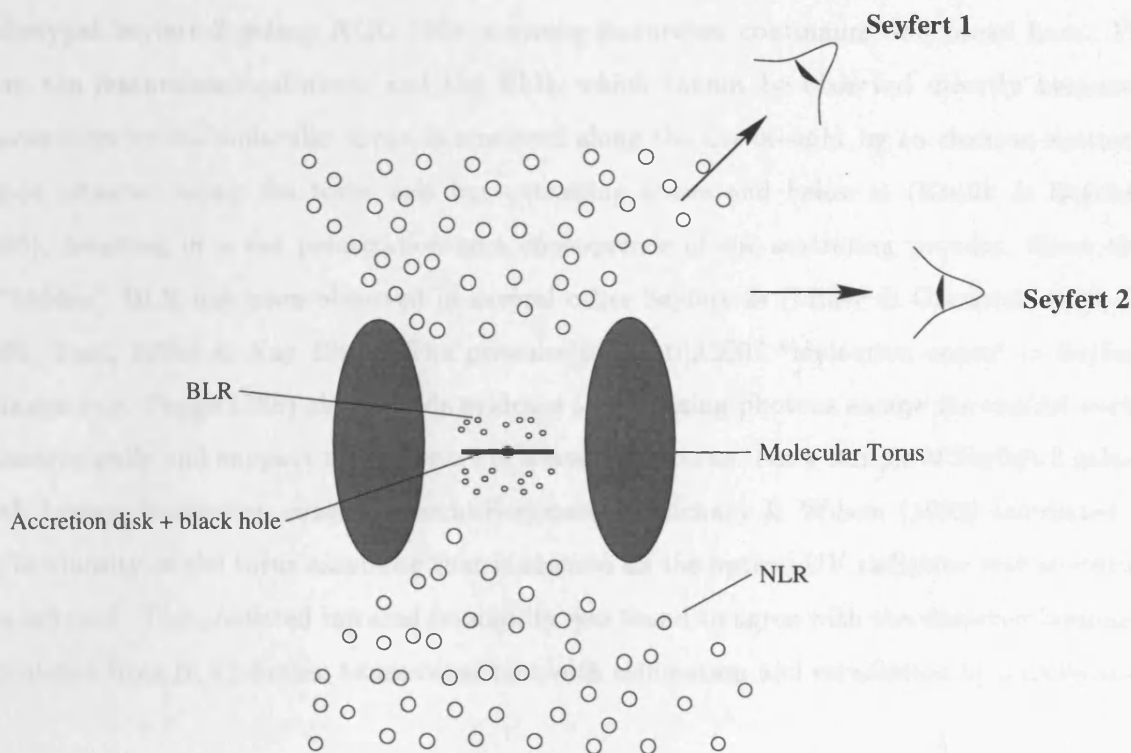


Figure 1.4: The Seyfert Unification Model: A diagram of the nucleus in Seyfert galaxies. Shown are different orientations of the molecular torus with respect to the observer's line-of-sight when viewing type I and II galaxies.

Czerny & Elvis 1987; Laor, Netzer & Piran 1990). Variability studies of ultraviolet lines with respect to the non-stellar continuum (Ulrich *et al.* 1984) have shown that the BLR is located $\lesssim 1$ pc from the continuum source. The BLR is situated within the obscuring region, whereas the NLR extends above and below it (Figure 1.4). The NLR is sufficiently extended to be spatially resolved in the optical for many nearby active galaxies. The morphology of the NLR reveals important information about its distribution and kinematics while the intensity ratios of emission lines from individual ions (e.g. [O III] $\lambda\lambda 4363, 4959, 5007$; [S II] $\lambda\lambda 6716, 6731$) enable the electron densities and temperatures that exist in these regions to be determined. Knowing the physical state and dynamics of the NLR can tell us a lot about the central nucleus itself (see below). According to the unified scheme, we have a relatively clear view of the AGN in a Seyfert 1 galaxy, whereas in Seyfert 2 galaxies the torus is observed at sufficiently high inclination so as to introduce significant obscuration into the direct line-of-sight to the central source. This hypothesis was put forward when Antonucci & Miller (1985) found, in the polarized flux of the

archetypal Seyfert 2 galaxy NGC 1068, a strong featureless continuum and broad lines. Flux from the featureless continuum and the BLR, which cannot be observed directly because of obscuration by the molecular torus, is scattered along the line-of-sight by an electron scattering region situated along the torus axis but extending above and below it (Krolik & Begelman 1986), resulting in a net polarization as a consequence of the scattering process. Since then, a “hidden” BLR has been observed in several other Seyfert 2s (Miller & Goodrich 1990, Kay 1990, Tran, Miller & Kay 1992). The presence of $[\text{O III}]\lambda 5007$ “ionization cones” in Seyfert 2 galaxies (e.g. Pogge 1988) also provide evidence that ionizing photons escape the central nucleus anisotropically and support the existence of a molecular torus. For a sample of Seyfert 2 galaxies with known “ionization cones”, Storchi-Bergmann, Mulchaey & Wilson (1992) calculated the IR luminosity of the torus assuming that it absorbs all the optical-UV radiation and re-emits in the infrared. The predicted infrared luminosity was found to agree with the observed luminosity calculated from IRAS fluxes, hence consistent with collimation and reradiation by a dusty torus.

1.3 X-ray properties of Seyferts

Seyfert galaxies have been observed extensively in the X-ray band to reveal a host of interesting properties. X-ray observations of Seyferts, in general, support unification models (see Mushotzky, Done & Pounds 1993 for a detailed review). Seyfert 1 galaxies are typically much brighter X-ray sources than Seyfert 2s, a result which is explained by obscuration and orientation effects as mentioned above.

1.3.1 The hard X-ray spectrum

Seyfert 1s

The apparent 2-20 keV continuum shape of a typical Seyfert 1 galaxies can be described, simply, by a power-law form $F(E) = AE^{-\alpha}$ erg cm⁻² sec⁻¹ keV⁻¹ with an energy index of $\alpha \sim 0.7$ (Mushotzky 1984; Turner & Pounds 1989). There is little or no evidence for a low energy cut-off which is indicative of line-of-sight absorption by cold gas. However, the detection of Fe K_{α} line emission, with a mean line energy of $E_{K_{\alpha}} \sim 6.4$ keV, from *Ginga* observations of many Seyfert 1s suggested that the hard continuum is reprocessed by cold material in some way. Pounds *et al.*

(1990) superimposed twelve *Ginga* observations of eight bright Seyfert 1 galaxies to produce a composite X-ray spectrum (the *Ginga*-12 spectrum). They found, from the residuals of a simple power-law fit, in addition to the iron line, an absorption dip between 7-10 keV and a “high energy tail” above ~ 12 keV. These two features gave further support to the idea that the primary continuum is reprocessed by optically thick, cold material (possibly an accretion disk) subtending a large solid angle thus producing a “Compton reflection” signal (Lightman & White 1988; George & Fabian 1991; Matt, Perola & Piro 1991). The continuum shape of this reflection spectrum is characterized by a broad “hump” which peaks at ~ 20 keV. The presence of this reflection component implies that the underlying continuum is steeper than initially inferred from earlier *HEAO-1* and *EXOSAT* observations with a mean index of $\alpha \sim 0.9$ (Nandra & Pounds 1994). The low energy resolution of *Ginga* made it difficult to determine whether the iron line in Seyfert 1s was broad or unresolved. However, a long *ASCA* observation, with its moderate spectral resolution, of the Seyfert 1 galaxy MCG-6-30-15 showed the Fe K_α line to be broad and skewed redward of the peak energy of 6.4 keV (Tanaka *et al.* 1995, see Figure 1.5). This characteristic line profile is very well explained by Doppler broadening and gravitational redshift due to an accretion disk orbiting either a non-rotating, Schwarzschild black hole (Fabian *et al.* 1989) or a rotating, Kerr black hole (Laor 1991). Nandra *et al.* (1997) found broad, asymmetric line profiles in the majority of a sample of Seyfert 1 galaxies, providing further evidence of relativistic effects in AGN. The discovery of a broad Fe K_α line in several AGN is now one of the strongest pieces of evidence for the presence of a supermassive black hole at the centre of these objects.

Seyfert 2s

The underlying continuum form of Seyfert 2 galaxies is similar to the canonical value found for Seyfert 1s (Nandra & Pounds 1994). However, the X-ray spectra of Seyfert 2s contain strong Fe K_α emission lines with a broad range of equivalent widths (Awaki *et al.* 1991; Smith & Done 1996) and are strongly cut-off at low-medium energies due to absorption by cold line-of-sight material with a column density $N_H > 10^{22} \text{ cm}^{-2}$. This obscuration of the central source is the reason why Seyfert 2s are fainter X-ray sources than Seyfert 1s and, in some cases, can account for all of the observed iron line intensity if we assume that the absorbing material is uniformly distributed around an isotropic X-ray source (Makishima 1986; Leahy & Creighton 1993). The X-ray spectrum of NGC 1068, the most famous Seyfert 2, on the other hand shows no low-energy

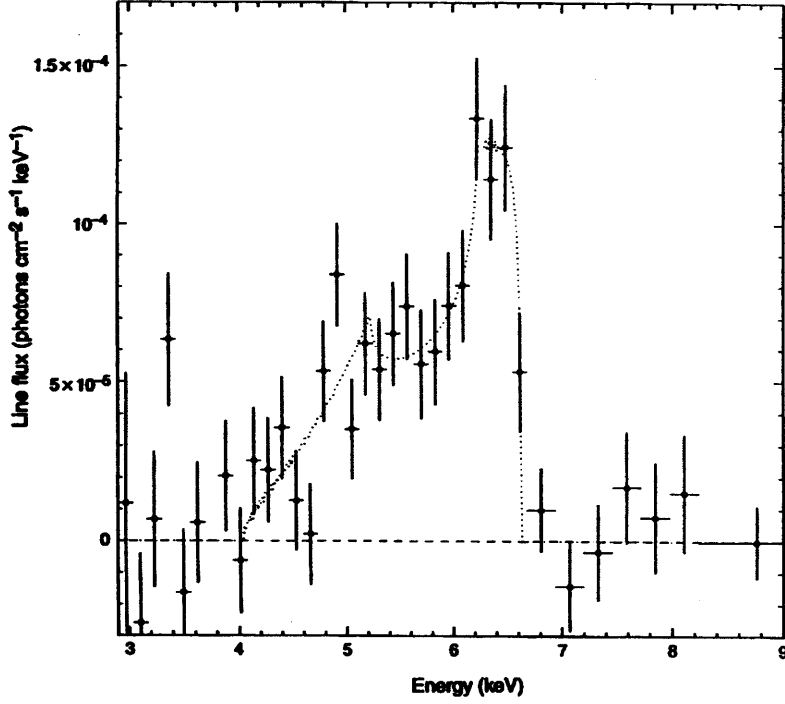


Figure 1.5: The Fe K_{α} line profile in MCG-6-30-15 (from Tanaka *et al.* 1995) and the best-fit model prediction from an accretion disk orbiting a Schwarzschild black hole (Fabian *et al.* 1989).

cut-off, but has very high equivalent width ($EW > 1$ keV) Fe K_{α} emission features (Koyama *et al.* 1989, Marshall *et al.* 1993, Ueno *et al.* 1994). The lack of a low-energy cut-off has led to the suggestion that the line-of-sight absorption towards NGC 1068 is $N_H > 10^{24}$ cm $^{-2}$, high enough to block X-ray photons with energies up to ~ 20 keV. The intrinsic continuum in NGC 1068 is electron scattered into the line-of-sight by a photoionized region that extends beyond the obscuring torus. This region is also where the Fe emission is produced. The fact that the direct flux is not observed explains the high EW of the iron line complex (Krolik & Kallman 1987). The advent of instruments with moderate spectral resolution (*BBXRT* and *ASCA*) showed the Fe K emission in NGC 1068 to be complex (Marshall *et al.* 1993, Ueno *et al.* 1994), consisting of narrow lines from neutral, helium- and hydrogen-like iron. Several other Seyfert 2s have also been shown to have unresolved Fe K emission (Turner *et al.* 1997a), however it is difficult to tell whether the emission is due to one broad line, as is the case for many Seyfert 1 galaxies, or several narrow ones, in the manner of NGC 1068.

1.3.2 The soft X-ray spectrum

Seyfert 1s

The extrapolation of the hard power-law continuum to softer energies ($E < 2$ keV) shows that an excess of flux over and above that expected from the primary continuum is a common feature in Seyfert 1 galaxies (Turner & Pounds 1989). This “soft excess” is steeper than the hard X-ray spectrum ($\Gamma > 3$ when fitted with a power-law) and could be either (i) emission from a distinct soft X-ray component, such as thermal emission from the hot innermost region of an accretion disk (Arnaud *et al.* 1985); (ii) leakage of the intrinsic continuum through a patchy cold absorber (e.g NGC 4151, Holt *et al.* 1980; Pounds *et al.* 1986); or (iii) transmission through a partially ionized absorber. The first evidence for the presence of a warm absorber in the line-of-sight to the central source in AGN was obtained by Halpern (1984) who suggested that the apparent increase in column density to the QSO MR 2251-178, which was observed twice by *EINSTEIN* over a period of 12 months, could be variations in the ionization structure of partially ionized gas. This variable absorption was confirmed by *EXOSAT* observations (Pan, Stewart & Pounds 1990) where a clear anti-correlation between the column density and source flux was found. The requirement for an edge from ionized iron in the Ginga spectra of many Seyfert 1s (Nandra & Pounds 1994) and the detection of an edge, thought to be a blend of O VII and O VIII K-edges, in a *ROSAT* PSPC observation of MCG-6-30-15 (Nandra & Pounds 1992) gave further support to the warm absorber model. *ASCA* data confirmed the presence of highly ionized oxygen edges in the soft X-ray spectrum of MCG-6-30-15 (Fabian *et al.* 1994, Reynolds *et al.* 1995) and detected warm absorbers in many other Seyfert 1 galaxies (Reynolds 1997, George *et al.* 1998). Indeed the increased resolution afforded by *ASCA* enabled the O VII and O VIII edges in MCG-6-30-15 to be resolved. Otani *et al.* (1996) found, from a 4 day observation of this object, that while the column density of the O VIII edge varied on a timescale of $\sim 10^4$ s, in phase with the continuum flux, the optical depth of the O VII edge remained constant throughout. The authors suggested the presence of two warm absorbing regions in this galaxy, one situated near the BLR and the other further out towards the molecular torus or NLR.

Seyfert 2s

If the high column density absorbing material, present in Seyfert 2 galaxies, completely covers

the central X-ray source, no intrinsic soft emission is expected below ~ 1 keV. The soft excess observed in Seyfert 2s (e.g. Mulchaey *et al.* 1993; Turner, Urry & Mushotzky 1993) is therefore a separate component to the hard X-ray flux. While the hard continuum of both Seyfert 1s and 2s exhibits variability on short time-scales (e.g. Grandi *et al.* 1992; Barr & Mushotzky 1986), there is little evidence for rapid variability in the soft X-ray flux of Seyfert 2s. Since the soft band emission of Seyfert 1s varies considerably this soft excess might also be expected to vary were it due to emission from an accretion disk or leakage from either a patchy or partially ionized absorber. The soft flux in Seyfert 2 galaxies is, therefore, currently best explained as a fraction of the intrinsic continuum that is scattered into the line-of-sight by electrons which extend beyond the obscuring material. Any variability of the hard continuum is therefore smoothed out by the scattering process. Using combined *EINSTEIN* SSS+MPC spectra of several Seyfert 2s, Turner *et al.* (1991) suggested that this soft excess emission could be a blend of soft X-ray lines, centered around 0.8 keV. There was also clear evidence, from *BBXRT* observations, for line emission at ~ 900 eV in NGC 1068 and Mrk 3, which Marshall *et al.* (1992) presumed to be unresolved Fe L lines. Band *et al.* (1990) predicted, for NGC 1068, that a significant amount of Fe L emission would be produced in the electron scattering region. However, *ROSAT* HRI observations of NGC 1068 (Wilson *et al.* 1992) showed that ~ 50 percent of the soft X-ray flux observed is extended, making it difficult to separate contributions from the unresolved nucleus and emission from starburst activity. Recent *ASCA* data of Seyfert 2 galaxies have shown several objects to possess line like features between 0.6–3 keV (Ueno *et al.* 1994; Iwasawa *et al.* 1994; Turner *et al.* 1997a).

1.4 X-ray emission mechanisms

The remarkable similarity in the spectral slopes of the hard continuum in Seyfert galaxies suggests that the X-ray flux is produced through one robust emission mechanism. This led to the proposition of several physical models in an attempt to explain the nature of the primary emission in AGN. Two popular types of models that are frequently discussed are non-thermal pair models (for a review see Svensson 1994) and thermal Comptonization models (Fabian 1994).

In non-thermal models the hard X-ray power-law is produced by the inverse Compton scattering of soft X-ray/UV photons by a power-law distribution of relativistic electrons (Zdziarski *et al.*

1990). The source of these seed photons could possibly be an accretion disk. One process that is thought to be important in both thermal and non-thermal models is the creation of electron-positron pairs. These pairs are created in regions where there is an abundance of photons with energy $\epsilon > m_e c^2$ and the photon density is high (i.e. compact regions). The compactness parameter, l , of an object is defined as

$$l \equiv \frac{L}{R} \frac{\sigma_T}{m_e c^3} \quad (1.1)$$

where L is the Luminosity, R is the source size and σ_T is the Thomson scattering cross-section. AGN are known to be very luminous and compact objects. An upper limit on the size of the emission region can be obtained from variability light travel time arguments. Several Seyferts have been shown to have $l > 10$ (Done & Fabian 1989), in which case there is a relatively high probability that two high energy photons will interact to produce an electron-positron pair.

The non-thermal pair models predict (i) a 2-10 keV energy index for the primary power-law, once reflection is taken into account, of $\alpha_{(2-10)} \approx 0.9$ over a wide range of parameters (e.g. compactness parameter, disk temperature and electron energy spectrum); (ii) a hard X-ray break, with a steepening of the spectrum to values of α between $\alpha_{(2-10)} + 0.5$ and $\alpha_{(2-10)} + 1.0$, that moves to lower energies with increasing source luminosity; (iii) an electron-positron annihilation line at 0.511 MeV and (iv) a spectral break at a few MeV. While there is agreement between several of the model predictions and observations, the lack of annihilation lines in Seyfert spectra causes severe problems for purely non-thermal models.

Thermal Comptonization models are similar to non-thermal models in that inverse Compton scattering is the main process of producing hard X-rays in both types of model. In thermal Comptonization models, however, the seed photons are scattered off hot electrons that have a thermal distribution (Sunyaev & Titarchuk 1980). These models predict, after repeated scattering, an X-ray spectrum of power-law form with an energy index that is dependent on the temperature and optical depth of the hot plasma. Haardt & Maraschi (1991) developed a two-phase model consisting of a cold, optically thick accretion disk (phase 1) and a hot corona of electrons (phase 2) that are in thermal equilibrium and situated above the disk. A large fraction

of the gravitational power is assumed to be channelled into the heating of the electrons. The thermal emission from the accretion disk provides the soft photons to be scattered by, and hence cool, the corona of hot electrons situated above the disk. Approximately half of the hard X-rays produced go into heating up the accretion disk. Because of this coupling between the hot corona and the cooler accretion disk an energy index of $\alpha \sim 1$ is obtained for a broad range of optical depths and temperature. In contrast to non-thermal models an annihilation line should not be observable from a hot thermal plasma and the spectrum is expected to roll over at energies $\sim 50\text{-}500$ keV (Haardt & Maraschi 1993).

Recent OSSE observations of Seyfert galaxies (e.g. Johnson *et al.* 1997; Zdziarski *et al.* 1995) have shown that the X- γ ray spectra of Seyfert galaxies are well described by a power-law of index $\alpha \sim 0.9$ which is exponentially cutoff at \approx several hundred keV. Thus far the simplest physical interpretation of these observations is Comptonization of UV photons in an optically thin, relativistic, thermal plasma. However, it is likely that in reality both thermal and non-thermal emission mechanisms contribute to the observed spectra of Seyfert galaxies (Zdziarski, Lightman & Maciolek-Niedźwiecki 1993).

Chapter 2

Instrumentation and Data Reduction

2.1 *Ginga*

Ginga, initially called ASTRO-C (Makino *et al.* 1987), was the third Japanese X-ray astronomy satellite. It was launched on February 5th 1987 and stayed in a low orbit (initial apogee and perigee of 770 km and 510 km respectively) until November 1st 1991. During this time a total of approximately 350 sources were observed including 36 Seyfert 2 galaxies. There were three scientific instruments on board *Ginga* (Figure 2.1); the large area proportional counter (LAC), an all-sky monitor (ASM) and a gamma-ray burst detector (GBD).

2.1.1 The LAC

The LAC, which was designed and built by a UK team led by Leicester University, was the main scientific instrument on *Ginga*, and consisted of 8 identical collimated proportional counters with a total effective area of 4000 cm². The field of view had a FWHM of 1°x 2°. Each detector had a top- and a mid-layer which provided spectral coverage across nominal 2-30 keV and 6-30 keV energy bands respectively. The overall spectral resolution (FWHM) of the LAC was 18% at 6 keV and scaled as $E^{-0.5}$ over the full energy range. A plot of the effective areas of both the top- and mid-layers is given in Figure 2.2. A detailed technical description of the LAC is given by Turner *et al.* (1989).

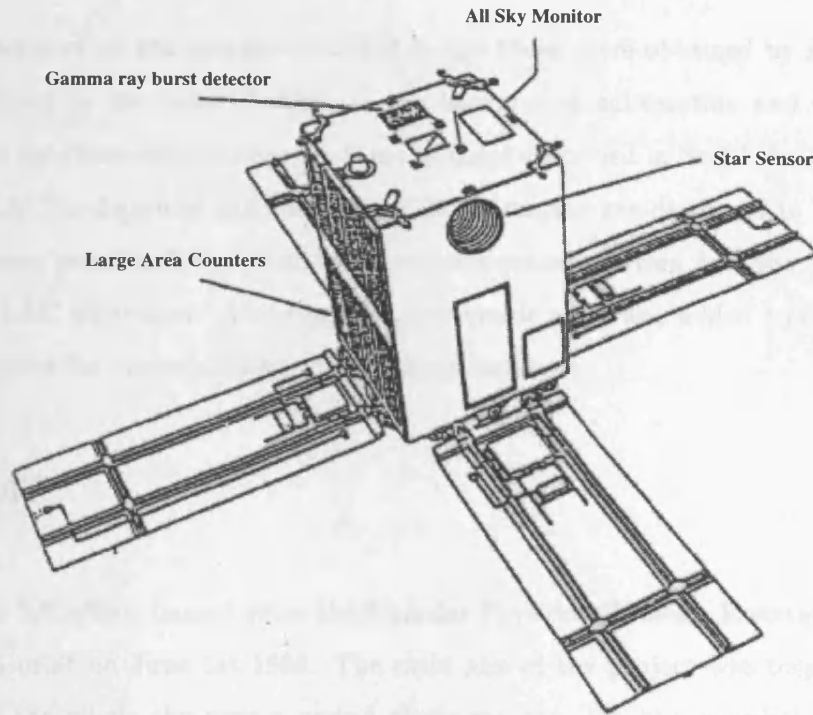


Figure 2.1: The *Ginga* satellite

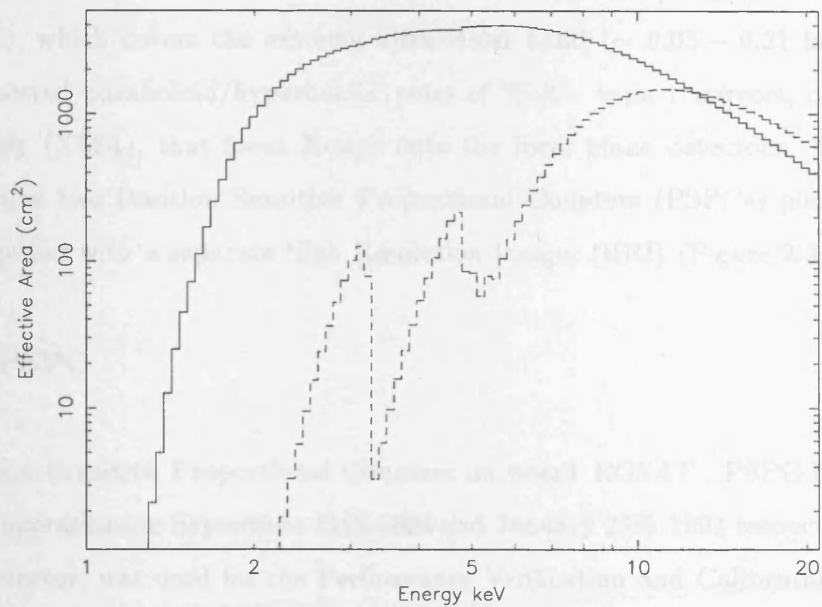


Figure 2.2: The effective area of the *Ginga* “top-” (solid curve) and “mid-layer” (dashed curve) in the 1-20 keV band.

2.1.2 Data Reduction

The Ginga spectra of all the galaxies analysed in this thesis were obtained by D.A. Smith. The methods employed in the data selection, in the background subtraction and in correcting for pointing offsets for these objects were the same as those described in Smith & Done (1996). The origin of the LAC background and methods of its estimation are discussed in Hayashida *et al.* (1989). Whenever possible X-ray pulse-height spectra extracted from *both* the “top-” and “mid-layers” of the LAC were used. A one percent systematic error was added to each pulse-height channel to account for uncertainties in the detector response.

2.2 ROSAT

The ROentgen SATellite, named after the German Physicist Wilhelm Roentgen was launched into low Earth orbit on June 1st 1990. The main aim of the project was to provide an X-ray slew survey of the whole sky over a period of six months. On the completion of this survey *ROSAT* was operated in Pointed Observation mode until December 18th 1998 when operations were finally terminated and the satellite was placed in safe-mode. *ROSAT* consists of the main X-ray telescope (XRT), which is sensitive in the $\sim 0.1 - 2.4$ keV range, and the Wide Field Camera (WFC), which covers the extreme ultra-violet band ($\sim 0.05 - 0.21$ keV). The XRT includes four nested paraboloid/hyperboloid pairs of Wolter type 1 mirrors, called the X-ray Mirror Assembly (XMA), that focus X-rays onto the focal plane detectors. The focal plane assembly contains two Position Sensitive Proportional Counters (PSPCs) plus an associated filter wheel together with a separate High Resolution Imager (HRI) (Figure 2.3).

2.2.1 The PSPC

The two Position Sensitive Proportional Counters on board *ROSAT*, PSPC-B and PSPC-C, ceased routine operations in September 11th 1994 and January 25th 1991 respectively. PSPC-C, the primary detector, was used for the Performance Verification and Calibration phase (PVC) and all the six-month all-sky survey, except for the last week, when a computer malfunction caused the satellite to slew across the sun, burning a hole in the detector window, hence de-

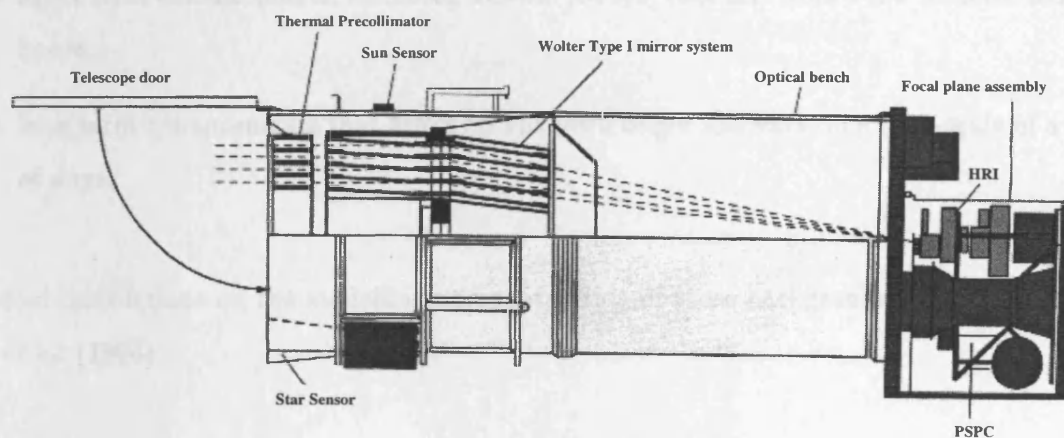


Figure 2.3: A schematic of the *ROSAT* satellite and its instruments.

stroying it. The PSPC-B detector was used subsequently until it ran out of gas and was shut down.

The PSPC is a multi-wire proportional counter with a field of view of 2° . It is sensitive in the 0.1 - 2.0 keV range and has a spectral resolution $\Delta E/E = 0.43(E/0.93)^{-0.5}$. The combined XMA+PSPC on-axis effective area is $\sim 200 \text{ cm}^2$ at 1 keV. The PSPC has moderate spatial resolution that is dependent on both photon energy and off-axis angle. For example, for an on-axis source the radius enclosing 50 percent of the photons is $\sim 14 \text{ arcsec}$ and 26 arcsec at 1 keV and 0.2 keV respectively (see Hasinger *et al.* 1992a; Hasinger *et al.* 1992b).

The PSPC Background

The X-ray background of the PSPC can be split into two main categories, cosmic and non-cosmic. The non-cosmic background consists of five separate components:

- a particle induced background from high-energy charged particles and γ rays (i.e. cosmic rays).
- afterpulses, which are secondary, low energy events following higher energy events such as particle background events.

- solar X-rays which are scattered into the line-of-sight by the Earth's atmosphere.
- short term enhancements, including auroral X-rays, that last from a few minutes to several hours.
- long term enhancements that are of an unknown origin and vary on a time-scale of a couple of days.

Detailed instructions on the modelling and subtraction of these backgrounds are given in Snowden *et al.* (1994).

2.2.2 The HRI

The *ROSAT* High Resolution Imager is made up of two cascaded micro-channel plates (MCPs) with a crossed grid charge detector and was in operation for almost nine years. It has a field of view of 38 arcminutes and a nominal FWHM spatial resolution of 1.7 arcsec. The on-axis Point Spread Function (PSF) of the XMA+HRI combination, however, has a FWHM of 4.6 arcsec. The HRI is sensitive in the 0.1 - 2.4 keV band but has very limited spectral resolution.

2.3 ASCA

ASCA (ASTRO-D), the fourth and latest Japanese X-ray astronomy satellite, superseded *Ginga* on February 20th 1993 when it was launched into a low earth orbit (Tanaka, Inoue & Holt 1994). The ASCA observatory (Figure 2.4) consists of four identical, co-aligned telescopes, each of which has 120 nested gold-plated conical foil mirrors, that focus X-rays onto four detectors. The PSF of the X-ray telescope (XRT) has a characteristic Maltese cross shape with a sharp core (FWHM \sim 50 arcsec) but very broad wings (Half Power Diameter (HPD) of 3 arcmin). The detectors on-board ASCA include two Solid-State Imaging Spectrometers (SIS-0 and SIS-1) and two Gas Imaging Spectrometers (GIS-2 and GIS-3).

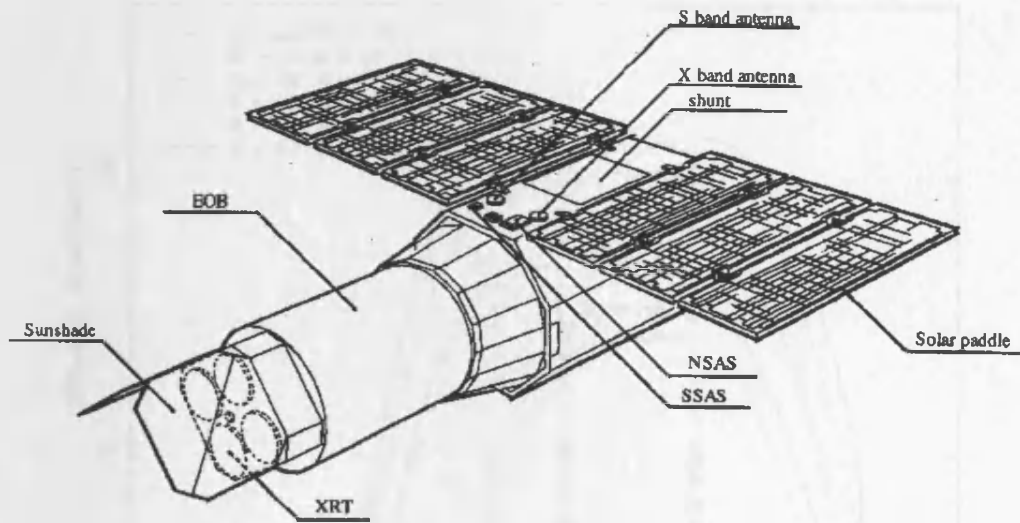


Figure 2.4: The ASCA satellite.

2.3.1 GIS

The GIS is an imaging gas scintillation proportional counter. It has a circular field of view of 50 arcmin and is sensitive between 0.7 - 10.0 keV (Figure 2.5). The spectral resolution of the GIS is $\sim 8\%$ at 6 keV and varies as $E^{-0.5}$. The PSF of the GIS is gaussian in shape, has a FWHM ~ 70 arcsec at 6 keV, which is comparable to that of the XRT, and is proportional to $E^{-0.5}$ (Ohashi *et al.* 1996; Makishima *et al.* 1996). All of the GIS observations in this thesis were taken in the same mode called the pulse height (PH) mode.

2.3.2 SIS

Each SIS has four CCD chips in a 2x2 configuration and each CCD is made up of 420x422 pixels giving a maximum field of view for the SIS of $\sim 20 \times 20$ arcmin. The response of the SIS is softer than the GIS, with an energy range between 0.4 - 10.0 keV (Figure 2.6). The PSF of the SIS is negligible compared to that of the XRT. The energy resolution of the SIS is dependent on the mode of operation during the observation (see below) and has been degrading since launch due to radiation damage (see Table 2.1). During an observation the SIS operate in two concurrent

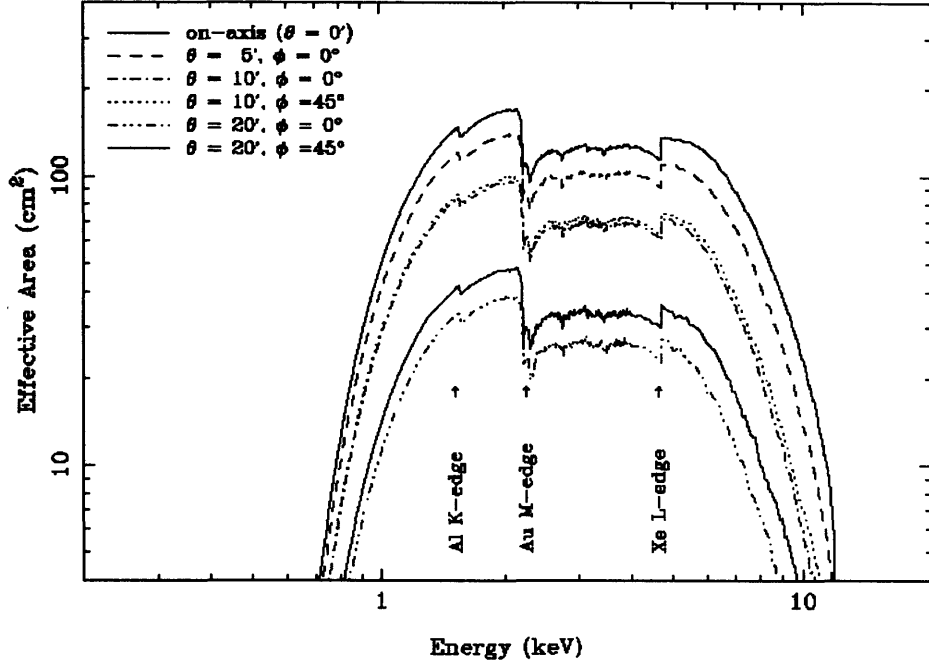


Figure 2.5: The Effective area of one XRT+GIS for different off-axis(θ) and azimuthal (ϕ) angles.

modes: the clocking mode (or CCD mode) and the data mode.

Time after launch (yrs)	$\Delta E/E$ at 5.9 keV (%)
0	2.1
1	2.8
2	3.4
3	3.8
4	4.3
5	4.7

Table 2.1: Degradation of the energy resolution of SIS-1 in 1-CCD mode

CCD Modes

There are four clocking modes which determine the timing resolution and the field of view available to each observation: 4-CCD, 2-CCD, 1-CCD and the parallel sum mode. In 4-CCD mode all four pixels are exposed, giving the maximum field of view but the worst timing resolution. It takes 4 seconds to readout one CCD row by row, pixel by pixel, hence the timing resolution in 4-CCD mode is 16 s. Two CCDs are exposed in 2-CCD mode, halving the field of view and

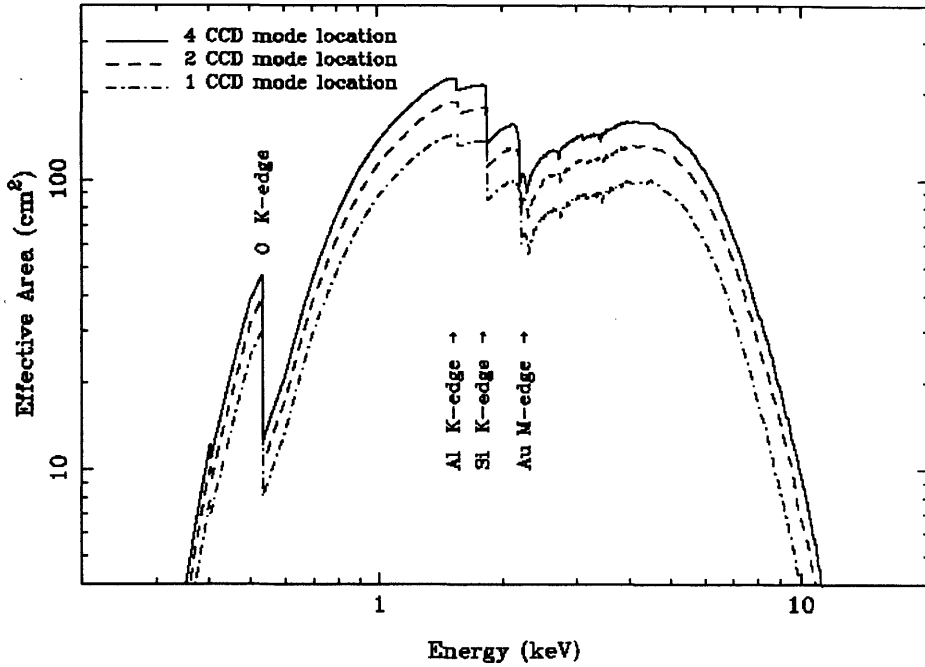


Figure 2.6: The Effective area of one XRT+SIS at the nominal pointing positions for three different clocking (CCD) modes.

giving a timing resolution of 8 s. Any pair of CCDs can be used in this mode. Predictably, only one CCD is exposed in 1-CCD mode giving a quarter of the maximum possible field of view and a time resolution of 4 s. Any one of the four chips can be used, however chip 1 on SIS-0 and chip 3 on SIS-1 are better calibrated and therefore almost always used in this mode. The parallel sum mode is used in conjunction with the FAST data mode (see next section).

Data Modes

There are three data modes which describe how the charge cloud, produced by an X-ray photon is analyzed and telemetered to the ground: FAINT, BRIGHT and FAST. FAST mode data sacrifices spatial information for a temporal resolution of 15.625 ms. Every object mentioned here was taken in either FAINT or BRIGHT mode, therefore FAST mode is not discussed further.

- **FAINT mode:** This mode provides the greatest amount of information about an event. For each event, the position of the central pixel plus its pulse height is given coupled

with the pulse height in the surrounding eight pixels. The pulse height of each event is converted into one of 4096 spectral channels.

- **BRIGHT mode:** Only 2048 spectral channels are available in this mode. The central pixel position is given, as in FAINT mode, however a grade defines how the charge cloud is distributed about the central pixel.

Once telemetered to the ground, FAINT mode data can be converted into BRIGHT or BRIGHT2 mode. Converted BRIGHT and true BRIGHT mode can be combined to increase the signal-to-noise ratio for relatively faint objects. The conversion of FAINT mode data to BRIGHT2 mode allows for the correction of the “echo” and “DFE” effects which slightly degrades the energy resolution of the SIS data taken in BRIGHT mode (see the *ASCA ABC Guide* for more details). However, out of all the objects analysed in this thesis, it was advantageous to use BRIGHT2 data for only one of them, namely object NGC 4507.

2.3.3 Standard Analysis Procedure

The *ASCA* data of all the objects analysed in this thesis were selected on the basis of the following screening criteria (keywords relating to the criterion are given in brackets) :

- Grade describes the shape of the charge cloud, created by an event, about a central pixel in the CCDs. Only events of grade 0,2,3 and 4 were used here since this combination provides the best compromise between spectral resolution and signal-to-noise.
- Was the data taken outside the South Atlantic Anomaly (SAA)?
The weakness of the Earth’s magnetic field in the SAA allows cosmic rays to penetrate further into the Earth’s atmosphere than usual, hence the particle background in the SAA is extremely high. Events recorded inside the SAA were therefore discarded.
- The time since or before passage through the SAA (T_SAA) or a satellite day/night transition (T_DY_NT).

Data taken as the satellite enters or clears the SAA or a day/night transition should be ignored, because of inaccuracies in the dark frame map, until 4 readout times (i.e. 16 s, 32 s, 64 s for 1-CCD, 2-CCD, and 4-CCD modes respectively; see § 2.3.2) have elapsed.

- The elevation angle to the Earth (ELV).

This is the angle between the Earth's limb and the satellites pointing direction. To prevent X-rays from the target source being absorbed or scattered by the Earth's atmosphere the elevation angle had to be greater than 5° .

- The magnetic cut-off rigidity (COR).

The COR is the threshold momentum a cosmic ray requires to penetrate as far as the satellite's orbit. In order to keep the particle induced background as low as possible data taken when the cut-off rigidity was less than 6 GeV/c were ignored.

- The root mean square deviation of the satellite from the nominal pointing position (ANG_DIST) had to be less than 0.01° .

- The bright Earth angle (BR_EARTH).

The BR_EARTH is similar to the ELV, however it is the angle between the Earth's limb and the pointing direction when the Earth is illuminated. Optical, UV and soft X-rays from the Sun can be scattered by the Earth's atmosphere and degrade the data quality hence the criteria used was that the bright Earth angle had to be greater than 20° .

- The number of CCD pixels per second that are registered as active (Sx_PIXLy).

Pixels are labelled active if events exceed a certain threshold, which again depends on the clocking mode.

In the subsequent spectral analyses spectral data sets were obtained from each telescope by integrating events within a circular region (radius ~ 4 and ~ 6 arcmin for the SIS and GIS respectively) centered on the source position, the background was estimated from source-free regions in the same observation. All SIS and GIS data below 0.6 and 0.8 keV respectively were ignored since the uncertainty in the calibration is highest in these low energy channels. The pulse-height spectra were binned so as to give at least 20 counts per spectral channel and, unless otherwise stated, the data from all four detectors were fitted simultaneously.

The observation log for all of the objects analysed in this thesis is given in Table 2.2.

Table 2.2: Observation log

Name	Position ^a		Ginga	Observation Date		ROSAT	Ginga	Exposure time (ks)				ROSAT	Redshift ^a	N _{Gal} ^b (10 ²⁰ cm ⁻²)
	R.A. (2000)	Dec. (2000)		ASCA(1)	ASCA(2)			ASCA(1) SIS	GIS	ASCA(2) SIS	GIS			
Mrk 348	00 48 47.1	+31 57 25	13/05/87	04/08/95			46	42	48				0.015	5.7
Mrk 3	06 15 36.4	+71 02 15	27/09/89	21/04/93		8/03/93	24	30	42			15	0.014	8.7
NGC 4507	12 35 36.9	-39 54 36	08/07/90	12/02/94			13	25	33				0.012	7.0
ESO 103-G35	18 38 20.4	-65 25 41	11/04/91	03/09/94	26/09/95		24	11	12	3	3		0.013	6.5
IC 5063	20 52 02.0	-57 04 09	2/10/90	25/04/94	27/04/94		14	10	9	26	26		0.011	4.9
NGC 7172	22 02 01.7	-31 52 18	27/10/89	12/05/95	17/05/96		48	11	15	25	29		0.008	1.7
NGC 7582	23 18 23.3	-42 22 16		14/11/94				19	20				0.005	1.9
			PV1	PV2	AO1	AO4		PV1 ^c	PV2 ^c	AO1 ^c	AO4 ^c			
NGC 4151	12 10 32.7	+39 24 21	24/05/93	05/11/93	04/12/93	10/05/95		7	16	33	98		0.003	2.0

^a Taken from the Simbad database operated at CDS, Strasbourg.^b The Galactic HI column density derived from 21cm measurements of Stark *et al.* (1992)^c Exposure times for ASCA SIS only.

Chapter 3

The broad-band X-ray spectrum of a typical Seyfert 2 galaxy: the case of Mrk 3

3.1 Introduction

X-ray observations of Seyfert galaxies have been used to investigate several interesting properties of their spectra including (i) the temporal and spectral properties of the hard X-ray continuum produced close to the super-massive blackhole, (ii) the low-energy cut-off of the intrinsic continuum, usually observed in Seyfert 2 galaxies, due to heavy absorption by cold gas, (iii) the presence of a Compton reflection component from optically thick matter situated close to the central source, (iv) the intensity and profile of the iron K_{α} line (especially the broad line profile associated with predicted gravitational redshifts and Doppler broadening effects), and (v) evidence of highly ionized material whether viewed directly against the continuum source as a warm-absorber or, indirectly, via scattered nuclear emission in those sources where the direct soft X-ray continuum is strongly cut-off due to line-of-sight absorption. The X-ray regime is the part of the electromagnetic spectrum which is least affected by the obscuration and orientation effects that are, according to the Unified scheme, the main reasons that Seyfert 1s and 2s appear different in the optical band. X-ray observations of Seyfert galaxies, therefore, provide powerful tools to test the Unified theory and yield valuable information on the innermost parts of the central engine. Mrk 3 was one of the first Seyfert 2 galaxies in which a hidden BLR was detected in polarized flux (Miller & Goodrich 1990) and is a relatively strong X-ray source.

However, one particular point of interest in the case of Mrk 3 is that it appears to have a rather flat hard X-ray continuum form compared to Seyfert 1s. The *Ginga* observations (Awaki *et al.* 1990; Awaki *et al.* 1991) reveal a power-law index $\alpha \approx 0.5$, which is somewhat harder than is typical of Seyfert 1 galaxies (e.g. Nandra & Pounds 1994) and fairly extreme amongst the sample of ~ 16 Seyfert 2s studied by *Ginga* (Smith & Done 1996). In principle the observation of anomalously flat power-law slopes, even in a subset of Seyfert 2 galaxies (NGC5252 provides a further example; Cappi *et al.* 1996) could be interpreted as contradicting unification models. Flat spectrum populations are also of general interest in terms of their potential contribution to the cosmic X-ray background (XRB).

The work presented in this chapter has been published in a scientific journal (Griffiths *et al.* 1998) and includes contributions from R.S. Warwick, I. Georgantopoulos, C. Done and D.A. Smith. It focuses on the X-ray properties of the Seyfert 2 galaxy Mrk 3, using *non-simultaneous Ginga*, *ASCA* and *ROSAT* observations to secure broad (0.1–30 keV) spectral coverage of this object. Although Mrk 3 has previously been studied in some detail on the basis of the individual datasets (Awaki *et al.* 1990; Awaki *et al.* 1991; Iwasawa *et al.* 1994; Turner, Urry & Mushotzky 1993; Smith & Done 1996; Turner *et al.* 1997a; Turner *et al.* 1997b), the combination of the data from the three satellites provides clear benefits in terms of spectral modelling. For example, the *ASCA* instruments, despite their superior spectral resolution, do not have the spectral bandwidth to constrain the slope of the underlying hard X-ray continuum in a source, such as Mrk 3, where this continuum is strongly cut-off in the soft X-ray regime. However, once the continuum form is reasonably specified by the inclusion of *Ginga* data, then the *ASCA* observations provide tight constraints on sharp emission features. Similarly the inclusion of *ROSAT* data extends the spectral coverage below ~ 0.6 keV to give additional leverage when modelling the soft X-ray spectral form. The consideration of the composite spectrum also allows the possibility of spectral variability to be investigated in a consistent manner.

This chapter is organised as follows. Brief details of the observations and data reduction methods are presented in section 3.2. The next section describes the approach taken in modelling the various spectral datasets, including the use of the photoionization code *XSTAR* (Kallman & Krolik 1997) to calculate the emergent spectrum from a partially photoionized scattering medium. Finally, section 3.4 discusses the implications of the results in the context of other, recently published studies on the X-ray spectral properties of Seyfert 2 galaxies.

3.2 Observations and Data Reduction

3.2.1 The *Ginga* observations

Mrk 3 was observed with the LAC on board the *Ginga* satellite during the period September 27–28, 1989. The effective integration time was 24 ks and the average count rate was 4.6 count s^{-1} and 2.4 count s^{-1} in the top and mid-layer counters respectively. In the spectral analysis, data below 4.5 keV were ignored because of the presence of anomalous line features at ~ 3 –4 keV (possibly identified with argon K and xenon L lines in the LAC background; see Smith & Done 1996), and high energy channels above 27 keV were excluded due to their susceptibility to background subtraction errors.

3.2.2 The *ASCA* observations

ASCA observed Mrk 3 during the period April 21–22, 1993. The SIS data were taken in 4-CCD FAINT and BRIGHT modes. FAINT mode data (after conversion to BRIGHT mode) was combined with true BRIGHT mode data ($\sim 40\%$ more counts were obtained by using the combined true and converted BRIGHT mode data rather than the FAINT mode data alone). The events lists have been screened using the standard *ASCA* analysis procedure described in § 2.3.3. This resulted in 30 (42) ks of good SIS (GIS) data for Mrk 3. The average background-subtracted count rates for Mrk 3 were $0.05 \text{ count s}^{-1}$ and $0.04 \text{ count s}^{-1}$ in the SIS and GIS systems respectively.

3.2.3 The *ROSAT* observations

Mrk 3 was observed with the X-ray Telescope (XRT) and Position Sensitive Proportional Counter (PSPC) combination on board *ROSAT* during the period March 8–10, 1993. Data were rejected when the Master Veto rate exceeded a threshold of 170 count s^{-1} , which resulted in a total exposure time of ~ 15 ks. The background region was taken from an annulus with an inner radius of $9'$ and outer radius of $15'$, centred on Mrk 3, with all the confusing sources masked out. The observed 0.1–2.4 keV PSPC count rate was $0.06 \text{ count s}^{-1}$.

3.3 Spectral Analysis

In this section firstly the *Ginga* and *ASCA* spectra are considered separately so as to allow direct comparison with earlier studies and then more detailed spectral models are applied to the composite *Ginga*, *ASCA* and *ROSAT* spectra. The spectral analysis was conducted using XSPEC version 10.0.

There is a faint X-ray source detected $\sim 1.7'$ West of Mrk 3 in both the *ROSAT* PSPC (Turner, Urry & Mushotzky 1993) and HRI (Morse *et al.* 1995) images. The source flux is only $\sim 4.4\%$ of the flux from Mrk 3 in the 0.1–2.4 keV PSPC band. The presence of this faint source within the *Ginga* LAC field of view and in the *ASCA* “on-source” region is very unlikely to produce a significant effect in terms of the analysis of the Mrk 3 spectrum. (Furthermore the centroid of the source lies in the inter-chip gap for both the SIS0 and SIS1 detectors). Iwasawa *et al.* (1994) and Turner *et al.* (1997a) also report the detection of a BL Lac object, $10.6'$ NW of Mrk 3 in the *ASCA* data; this source also lies within the *Ginga* field of view. Based on the *ASCA* data an estimation of the count rate from the BL Lac object is roughly 2% of that of Mrk 3 in the 4–10 keV band, hence the impact of this confusing source on the *Ginga* measurements will be small.

3.3.1 The *Ginga* spectra

The first model used to fit the *Ginga* LAC spectra comprised a single hard power-law continuum, with energy index α and normalisation A_{Ginga} , which is heavily cut-off at low energy due to absorption by cold solar abundance gas of column density, N_H . This simple model is given by the equation:

$$F(E) = A_{Ginga} \times E^{-\alpha} \times e^{-(\sigma(E)N_H)} \text{ keV cm}^{-2} \text{ s}^{-1} \text{ keV}^{-1} \quad (3.1)$$

$\sigma(E)$ is the photoelectric absorption cross-section of the gas at energy E (keV).¹ An iron K_α emission line of intensity $A_{K\alpha}$ at an energy $E_{K\alpha}$ was also included with a width fixed at $\sigma_{K\alpha}$

¹Element abundances and absorption cross-sections adopted by Morrison & McCammon (1983) are used unless otherwise stated.

Table 3.1: Spectral fitting of the *Ginga* data alone

Parameter	Model 1	Model 2
α	$0.37^{+0.15}_{-0.14}$	$0.65^{+0.20}_{-0.19}$
A_{Ginga}^a	$0.6^{+0.3}_{-0.2}$	$1.5^{+1.1}_{-0.6}$
N_H^b	58 ± 7	69 ± 9
$E_{K\alpha}^c$	6.39 ± 0.10	$6.33^{+0.19}_{-0.21}$
$A_{K\alpha}^d$	7.9 ± 1.4	$4.0^{+2.2}_{-2.4}$
E_{edge}^c	-	$8.1^{+0.4}_{-0.5}$
τ_{edge}	-	0.24 ± 0.10
χ^2	56.0	42.1
d.o.f.	56	54

^a 10^{-2} photon $\text{cm}^{-2} \text{s}^{-1} \text{keV}^{-1}$.

^b 10^{22}cm^{-2} .

^c keV.

^d 10^{-5} photon $\text{cm}^{-2} \text{s}^{-1}$.

= 0.1 keV (this value is used throughout, see section 3.4). This model (Model 1) provides a good match to the *Ginga* data for Mrk 3; Table 3.1 lists the best-fit parameters and associated errors.² The parameter values derived on the basis of Model 1 agree reasonably well with earlier analyses of the *Ginga* (top-layer only) spectra (Awaki *et al.* 1990; Awaki *et al.* 1991). Specifically, on the basis of the *Ginga* data alone, the rather hard continuum spectrum is confirmed (i.e. $\alpha = 0.37^{+0.15}_{-0.14}$). However, one apparent discrepancy is that Smith & Done (1996) obtained $\alpha = -0.15^{+0.13}_{-0.19}$ for Mrk 3, which is a very much flatter continuum slope than quoted here. The origin of this problem can be traced to the fact that Smith & Done restricted their analysis to the 2–18 keV energy range whereas here the 4.5–27 keV band is used. Employing Model 1 to fit the *Ginga* 2–18 keV top-layer data for Mrk 3 also results in a peculiar spectral index. This emphasises the value of the high energy data, particularly that from the LAC mid-layer. (The mid-layer has a larger effective area than the top-layer above ~ 10 keV (see Figure 2.2) and therefore provides useful additional constraints on the slope of the hard X-ray continuum).

²The errors quoted throughout this thesis are 90 per cent confidence limits for one interesting parameter following the prescription of Lampton, Margon & Bowyer (1976).

The measured *Ginga* count rate spectra, the best-fitting spectral model and the spectral fitting residuals are shown in Fig. 3.1. The residuals suggest the possible presence of an additional absorption edge at ~ 8 keV. When such a feature is included a reduction in χ^2 of ~ 14 is obtained with two additional parameters, the edge energy E_{edge} and optical depth τ_{edge} (Model 2, Table 3.1), which in terms of the F-test is significant at the > 99 % level. One effect of this additional iron absorption is to steepen the continuum by $\Delta\alpha \approx 0.3$. The measured edge energy, $E_{edge} = 8.1^{+0.4}_{-0.5}$ keV, is consistent with the K-edge of iron in an ionization state in the range Fe xv-xxiii (Makishima 1986), implying the presence of highly ionized gas in the line-of-sight to the hard X-ray source in addition to the large column density of relatively cold gas. The possibility of additional line-of-sight absorption by photoionized gas is discussed further in § 3.3.3.

3.3.2 The ASCA spectra

Mrk 3 exhibits excess soft X-ray emission over and above that expected given the heavy absorption evident in the *Ginga* passband. To account for this soft X-ray emission the spectral form used to fit the ASCA SIS and GIS data was basically that of Model 1 (with free parameters α , A_{ASCA} , N_H , $A_{K\alpha}$, $E_{K\alpha}$) plus a second power-law with the same spectral slope as the intrinsic hard continuum but with a different normalisation (A_{soft}). Hereafter this will be referred to as the soft power-law component. In physical terms this soft power-law could be flux leakage from a partially covered source with an *uncovered* fraction $f = A_{soft}/A_{ASCA}$. Alternatively f could represent the fraction of the continuum flux which is directed into the line of sight by an extended electron scattering region where $f \equiv f_{scat}$ (see § 1.3.2). Here, this latter interpretation is pursued. The soft power-law component is assumed to be absorbed only by the Galactic foreground HI column density of $N_{Gal} = 8.7 \times 10^{20} \text{ cm}^{-2}$ (Stark *et al.* 1992).

The above spectral prescription provides only a modestly successful fit to the ASCA data (Model 3, Table 3.2). Significant residuals are evident at a variety of energies in the ASCA detectors. Previously Iwasawa *et al.* (1994) have reported the presence of line-like features at ~ 0.75 keV, 0.9 keV and possibly ~ 7.0 keV in the SIS spectra of Mrk 3 (in addition to the 6.4 keV line included in Model 3). Similarly Turner *et al.* (1997a) found that the addition of narrow lines at 1.85, 2.45, 6.4 and 6.96 keV (corresponding to Si xiii, S xv, Fe i-xvi and Fe xxvi respectively) to their best-fitting double power-law continuum model, significantly improved the fit to the

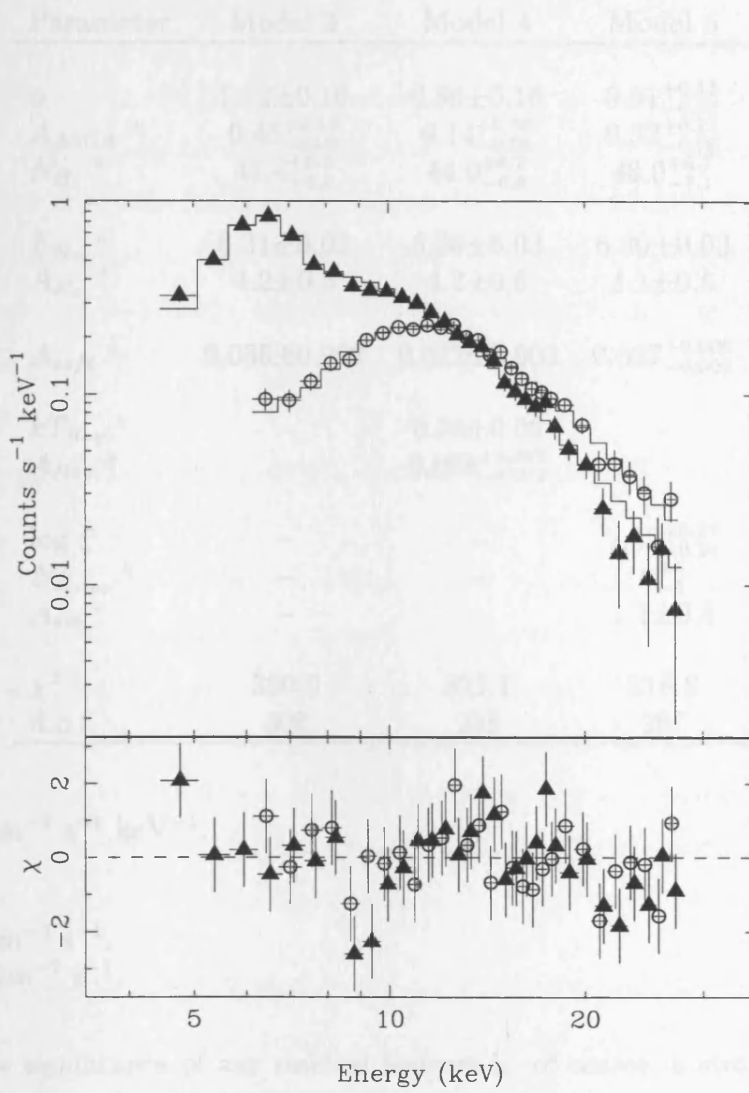


Figure 3.1: Top panel: The *Ginga* LAC top-layer (triangles) and mid-layer (circles) count rate spectra for Mrk 3. The solid line corresponds to the best fitting version of Model 1. Bottom panel: The spectral fitting residuals to the *Ginga* data for Mrk 3 (scaled in terms of the measurement errors).

Table 3.2: Spectral fitting of the ASCA SIS/GIS data alone

Parameter	Model 3	Model 4	Model 5
α	1.12 ± 0.10	0.56 ± 0.16	$0.91^{+0.11}_{-0.12}$
A_{ASCA}^a	$0.45^{+0.12}_{-0.09}$	$0.14^{+0.06}_{-0.05}$	$0.32^{+0.11}_{-0.08}$
$N_{H_1}^b$	$41.4^{+6.0}_{-5.3}$	$44.0^{+8.2}_{-6.8}$	$48.0^{+8.7}_{-7.1}$
$E_{K_\alpha}^c$	6.31 ± 0.03	6.30 ± 0.03	6.30 ± 0.03
$A_{K_\alpha}^d$	4.2 ± 0.6	4.2 ± 0.6	4.1 ± 0.6
A_{soft}^a	0.035 ± 0.002	0.022 ± 0.003	$0.037^{+0.006}_{-0.005}$
kT_{Ray}^c	–	0.74 ± 0.06	–
A_{Ray}^a	–	$0.008^{+0.002}_{-0.002}$	–
$\log \xi$	–	–	$2.42^{+0.27}_{-0.24}$
$N_{H_{scat}}^b$	–	–	6^{+5}_{-3}
A_{em}^e	–	–	1.1 ± 0.4
χ^2	390.0	321.1	318.8
d.o.f.	300	298	297

^a 10^{-2} photon $\text{cm}^{-2} \text{s}^{-1} \text{keV}^{-1}$.

^b 10^{22}cm^{-2} .

^c keV.

^d 10^{-5} photon $\text{cm}^{-2} \text{s}^{-1}$.

^e 10^{-12} photon $\text{cm}^{-2} \text{s}^{-1}$.

ASCA data. The significance of any residual features is, of course, a strong function of the continuum model fitted (see Turner *et al.* 1997a).

An improved fit is obtained if a solar-abundance Raymond-Smith component (temperature kT_{Ray} and normalisation A_{Ray}) is included *in addition to* the soft power-law (Model 4, Table 3.2). One aspect to note is that Model 4 gives a much flatter power-law slope than Model 3. The difference appears to arise from the fact that in Model 3 the intrinsic and soft power-laws are constrained to have the same spectral index and the steepness of the soft excess tends to pull the overall continuum form to a steeper slope, whereas when the Raymond-Smith component is included this linkage is much weaker. However, the soft X-ray power-law component is still essential since

fits of Model 4 with A_{soft} set to zero give a worse result than even Model 3 ($\chi^2/\text{d.o.f.} = 443/299$ compared to $\chi^2/\text{d.o.f.} = 390/300$).

The next section goes on to consider the possibility of fitting some of the line-like features with a model which includes the effects of photoionization on the putative scattering medium (and hence removes the requirement for a Raymond-Smith component). For completeness the results of fitting such a model to the *ASCA* -only data are included as Model 5 in Table 3.3 (details of this model are explained in the next section). The fact that this photoionization model gives a rather similar χ^2 to Model 4 suggests that it is difficult to distinguish between the two descriptions at the limits of the sensitivity and spectral resolution afforded by *ASCA* .

3.3.3 The composite *Ginga* , *ASCA* and *ROSAT* spectra

Since the *Ginga* , *ASCA* and *ROSAT* observations were not recorded contemporaneously (the observations were, in fact, made over a period of ~ 4 years) this analysis is based on the assumption that the spectral form of Mrk 3 is largely invariant. Thus in the spectral analysis only the normalisation of the intrinsic power-law continuum and the flux of the iron K_α line are allowed to vary between the *Ginga* and *ASCA* datasets; the spectral parameters used to model the *ROSAT* PSPC spectrum were identical to those applied to the *ASCA* data. This assumption will be checked later when considering the quality of the model fit to the composite spectra.

Table 3.3 gives the results of fitting Models 3 and 4 to the composite spectra for Mrk 3. The results generally mirror those obtained from the *ASCA* spectra alone, although as noted earlier the *Ginga* data prefer a rather harder power law and this influence is evident from a comparison of the results in Table 3.3 with those in Table 3.2. By way of illustration Fig. 3.2 shows the unfolded spectral data based on Model 3 and the corresponding count rate residuals to the composite spectrum. Interestingly the residual feature near 0.9 keV identified by Iwasawa *et al.* (1994) appears to be present both in the *ASCA* and *ROSAT* data. This is also consistent with the report by Turner, Urry & Mushotzky (1993) of the presence of a blend of soft X-ray lines below ~ 1 keV in the *ROSAT* PSPC spectrum of Mrk 3. Other distinctive line features are less obvious. For example, both Iwasawa *et al.* (1994) and Turner *et al.* (1997a) report the presence of a line near 7.0 keV which could be K_α emission from hydrogen-like iron. The presence of a narrow line at 6.87 keV (i.e. the redshifted energy of the Fe XXVI line) was investigated but it

was found that this line is at best ~ 20 times weaker than the 6.4 keV line and that its inclusion gives no significant improvement in the spectral fitting. Iwasawa *et al.* (1994) note that in their analysis this line is only marginally detected. It seems that this is a case where the continuum model has a crucial bearing on the inferred significance of a line feature.

The inclusion of the solar-abundance Raymond-Smith component in addition to the soft power-law continuum (Model 4) provides a dramatic improvement in the fit to the soft X-ray spectrum of Mrk 3. Figure 3.3(a) illustrates the form of this spectral model in the 0.3–3 keV band. With the *ASCA* spectral resolution, the line emission from the ~ 0.7 keV thermal component gives rise to a broad spectral enhancement in the range 0.7–1.0 keV in rough accord with that observed. As a trial the elemental abundance in the Raymond-Smith model were reduced to 0.2 solar and the spectra refit. The effect was to increase the contribution of the thermal continuum to the soft X-ray spectrum, particularly below 0.6 keV. As a result, the slope of the power-law continuum flattens somewhat from $\alpha \approx 0.45$ to $\alpha \approx 0.37$ giving a slightly improved fit ($\Delta\chi^2 \sim 7$).

As discussed earlier the soft power-law component in Models 3 and 4 can be interpreted as the fraction of the intrinsic hard X-ray continuum which is electron scattered into our line of sight. The excellent agreement between *ROSAT* PSPC and *ASCA* data at soft X-ray energies could be seen as supportive of this interpretation rather than partial covering, however the *ROSAT* and *ASCA* observations are only separated by six weeks and nothing is known about the behaviour of the hard continuum during this time. Therefore while a scattered continuum interpretation is probably the best bet, and is the assumption that the rest of the models discussed here are based on, a partial covering description of the soft flux cannot be ruled out with the current data. Unless the scattering region is completely photoionized by the incident nuclear flux, some absorption features, imprinted on the scattered flux, plus line emission, emanating from the photoionized medium, would be expected. Thus the possibility of extending Model 3 to include both absorption features in the scattered continuum and intrinsic emission from the scattering region is now considered.

The photoionization code used to model the emission and absorption of a cloud of photoionized gas was XSTAR (Kallman & Krolik 1997; see also chapter 5). This photoionization code calculates the emission and absorption spectra produced by a gas cloud in the vicinity of a point source of continuum radiation. The assumed spectrum of the central ionizing source is the same one used

Table 3.3: Spectral fitting of the composite *Ginga*, *ASCA* and *ROSAT* spectra for Mrk 3

Parameter	Model 3	Model 4	Model 5	Model 6	Model 7
α	0.88 ± 0.06	0.45 ± 0.08	0.66 ± 0.07	$0.80^{+0.07}_{-0.11}$	0.69 ± 0.07
A_{Ginga}^a	$2.58^{+0.47}_{-0.40}$	$0.77^{+0.20}_{-0.16}$	$1.39^{+0.29}_{-0.25}$	$1.62^{+0.29}_{-0.33}$	$1.63^{+0.26}_{-0.28}$
A_{ASCA}^a	$0.64^{+0.14}_{-0.12}$	$0.17^{+0.06}_{-0.04}$	$0.29^{+0.08}_{-0.07}$	$0.36^{+0.08}_{-0.09}$	$0.34^{+0.08}_{-0.07}$
N_H^b	$83.4^{+3.6}_{-3.5}$	66.4 ± 4.1	77.0 ± 4.0	$71.4^{+4.6}_{-4.8}$	$66.8^{+6.6}_{-3.7}$
$E_{K\alpha}^c$	6.29 ± 0.03	6.30 ± 0.03	6.29 ± 0.03	6.29 ± 0.03	6.28 ± 0.03
$A_{K\alpha}(Ginga)^d$	$6.0^{+1.4}_{-1.5}$	7.6 ± 1.4	7.0 ± 1.4	5.7 ± 1.5	5.2 ± 1.5
$A_{K\alpha}(ASCA)^d$	3.8 ± 0.6	4.1 ± 0.6	3.9 ± 0.6	$3.8^{+0.6}_{-0.5}$	3.8 ± 0.6
A_{soft}^a	0.033 ± 0.001	0.021 ± 0.002	0.038 ± 0.004	0.039 ± 0.004	$0.039^{+0.005}_{-0.004}$
kT_{Ray}^c	—	$0.69^{+0.07}_{-0.05}$	—	—	—
A_{Ray}^a	—	$0.0085^{+0.0018}_{-0.0011}$	—	—	—
$\log \xi$	—	—	2.81 ± 0.13	$2.61^{+0.23}_{-0.08}$	$2.78^{+0.12}_{-0.19}$
$N_{H_{scat}}^b$	—	—	17^{+6}_{-5}	10^{+7}_{-3}	16^{+5}_{-6}
A_{em}^e	—	—	0.9 ± 0.2	0.9 ± 0.2	0.9 ± 0.2
$N_{H_{warm}}^b$	—	—	—	—	39^{+1}_{-18}
R	—	—	—	0.8 ± 0.5	—
χ^2	581.0	417.6	405.6	397.0	391.2
d.o.f.	378	376	375	374	374

^a 10^{-2} photon $\text{cm}^{-2} \text{s}^{-1} \text{keV}^{-1}$.

^b 10^{22}cm^{-2} .

^c keV.

^d 10^{-5} photon $\text{cm}^{-2} \text{s}^{-1}$.

^e 10^{-12} photon $\text{cm}^{-2} \text{s}^{-1}$.

* reached upper limit of model.

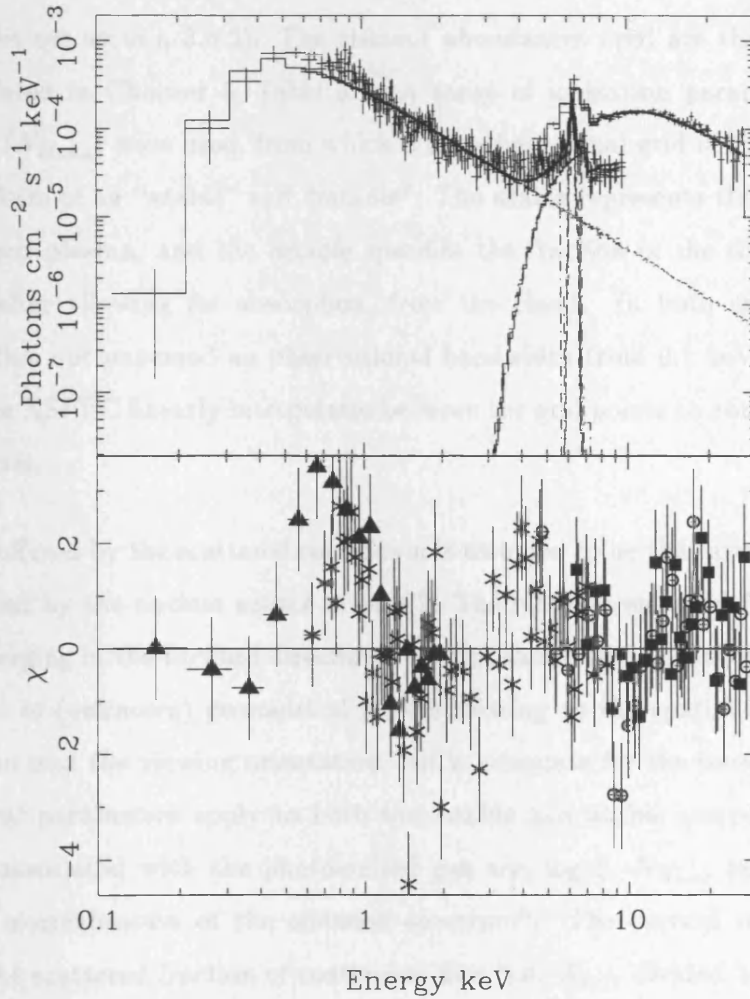


Figure 3.2: Top panel: The unfolded composite spectrum of Mrk 3 based on the best-fitting version of Model 3. Bottom panel: The spectral fitting residuals to the composite spectrum for Mrk 3. The data points correspond to *Ginga* top-layer (circles), *Ginga* mid-layer (squares), ASCA SIS-0 (crosses) and ROSAT PSPC (triangles). For clarity only the ASCA SIS-0 points are shown.

by Krolik & Kriss (1995) (Figure 5.2) and is typical of Seyfert 1 galaxies and low-luminosity quasars. The state of the gas cloud is described by the ionization parameter $\xi = L/nr^2$ where L is the source luminosity in the 0.0136 – 13.6 keV bandpass in erg s^{-1} , n is number of hydrogen atoms/ions in the gas per cm^3 and r is the distance of the inner edge of the cloud to the central source in cm. In the XSTAR models a density of $n = 10^6 \text{ cm}^{-3}$ and a gas temperature of 10^6 K is used (but see section 3.4.2). The element abundances used are the default values in XSTAR and are listed in Chapter 5, Table 5.1. A range of ionization parameters ($\log \xi$) and column densities ($N_{H_{\text{cat}}}$) were used, from which a two-dimensional grid of spectral models was produced in the form of an “atable” and “mtable”. The atable represents the intrinsic emission of the photoionized plasma, and the mtable specifies the fraction of the scattered power-law which emerges, after allowing for absorption, from the cloud. In both cases the tabulated spectral information encompassed an observational bandwidth from 0.1 keV up to 40 keV. In the spectral fitting XSPEC linearly interpolates between the grid points to obtain the best-fitting spectral parameters.

The absorption suffered by the scattered continuum is assumed to be that arising in a slab of gas directly illuminated by the nuclear source in Mrk 3. The intrinsic emission from the scattering region is that emerging in the forward direction from this same slab. Clearly this approximation ignores a number of (unknown) geometrical factors relating to the spatial distribution of the scattering medium and the viewing orientation, but is adequate for the present purpose. Thus one set of spectral parameters apply to both the mtable and atable components. The three free parameters associated with the photoionized gas are, $\log \xi$, $N_{H_{\text{cat}}}$ and A_{em} , the latter representing the normalisation of the emission spectrum³. The current modelling does not directly couple the scattered fraction of continuum flux (i.e. A_{soft} divided by either A_{ASCA} or A_{Ginga}) with A_{em} (see § 3.4.2 and 5.2.6).

The results of fitting this photoionization model are given as Model 5 in Table 3.3 (and also in Table 3.2). This model gives a slightly better fit to the Mrk 3 spectrum than is the case for pure electron scattering plus a Raymond-Smith component (Model 4, Table 3.3). The form of the spectrum in 0.3–3 keV band is shown in Figure 3.3(b). The best-fitting model has $\log \xi \approx 2.8$ and reproduces the observational feature near 0.9 keV as recombination directly into the K-shell of a completely stripped oxygen atom, a process which has a threshold energy of 0.87 keV. In

³See the XSTAR manual (Kallman & Krolik 1997) or Chapter 5 for the definition of this normalisation parameter.

Fig. 3.3(b) this O VIII recombination continuum feature is significantly broadened (FWHM = 70 eV) by the thermal energies of the free electrons in the 10^6 K photoionized medium.

The derived slope of the intrinsic power-law continuum in Models 4 and 5 remains relatively flat ($\alpha \approx 0.45$ and ≈ 0.66 respectively). One possible explanation for the apparent hardness of the underlying continuum in Mrk 3 is that Compton reflection makes a significant contribution to the observed flux above ~ 6 keV as appears often to be the case for Seyfert 1 galaxies (Pounds *et al.* 1990). This possibility was investigated by including a Compton reflection component in the spectral analysis; specifically the XSPEC “pexrav” model (Magdziarz & Zdziarski 1995) was employed. The reflection component is subject to absorption in the cold gas column density represented by N_H . In pexrav the parameter R represents the relative strength of the reflected signal, with a value of unity corresponding to reflection from a semi-infinite flat disk of cold material which is irradiated by an isotropic power-law continuum source. Here, for simplicity, the inclination angle of the disk is fixed at $i = 60^\circ$ and the same value of R is assumed to apply to both the *Ginga* and *ASCA* observations, implying that, on time-scales of a few years, the reflection component varies in phase with the hard continuum. The results of including reflection in the photoionized scattering model are listed in Table 3.3 as Model 6. The best-fitting version of Model 6 requires $R \sim 0.8$, (in the F-test the reduction in χ^2 of ~ 9 is significant at the $> 99\%$ level for one additional parameter). Alternatively, when the relative strength of the reflected signal is frozen at $R = 1$ and the inclination angle of the disk allowed to vary, we obtain a best-fit value of $i = 71^{+13}_{-16}$ deg. The inclusion of reflection in the spectral model leads to a value for the spectral index of the hard continuum in Mrk 3 of $\alpha \approx 0.8$, close to the canonical value of 0.9 measured similarly in Seyfert 1 galaxies (Nandra & Pounds 1994; Reynolds 1997; George *et al.* 1998).

The earlier discussion of the *Ginga* spectrum of Mrk 3 (§ 3.3.1) noted the evidence for additional line-of-sight absorption (over and above that represented by N_H) in the form of an edge feature near ~ 8 keV. If attributable to iron-K edge absorption, the implied ionization state of the absorbing gas is Fe XV-XXIII. This is rather close to the state of the iron in the photoionized scattering region (see Fig 3.4) and suggests a possible model in which the scattering zone extends not only directly above the nuclear source (i.e. along the axial direction of the nuclear region) but also sufficiently close to the plane of the system to intercept the line of sight (the presumption being that the nucleus is viewed at a fairly high inclination in the case of this “classical” Seyfert

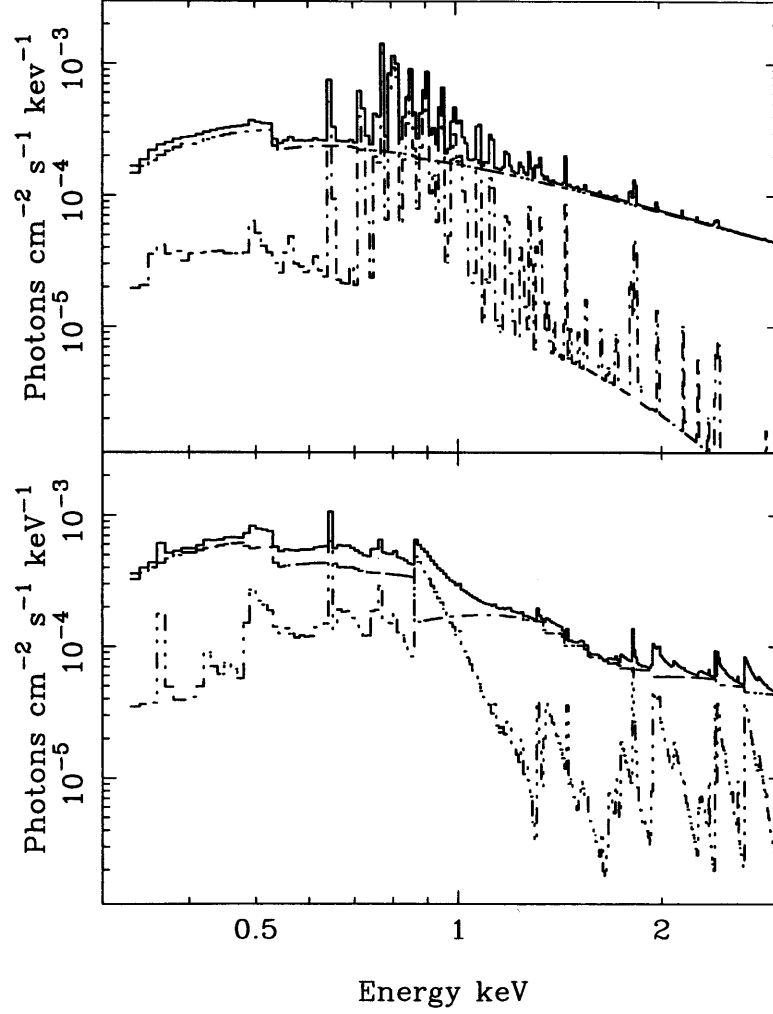


Figure 3.3: Modelling of the soft X-ray (0.3–3 keV) spectrum of Mrk 3. (a) As a blend of a soft (scattered) power-law continuum with a ~ 0.7 keV Raymond-Smith component. The spectrum from 0.7–0.9 keV is dominated by O, Fe (L shell) and Ne lines. (b) As an absorbed continuum scattered from a hot photoionized medium plus line emission from the same region. The feature near 0.9 keV is due to O VIII recombination and that at 0.65 keV corresponds to the O VIII L_{α} line.

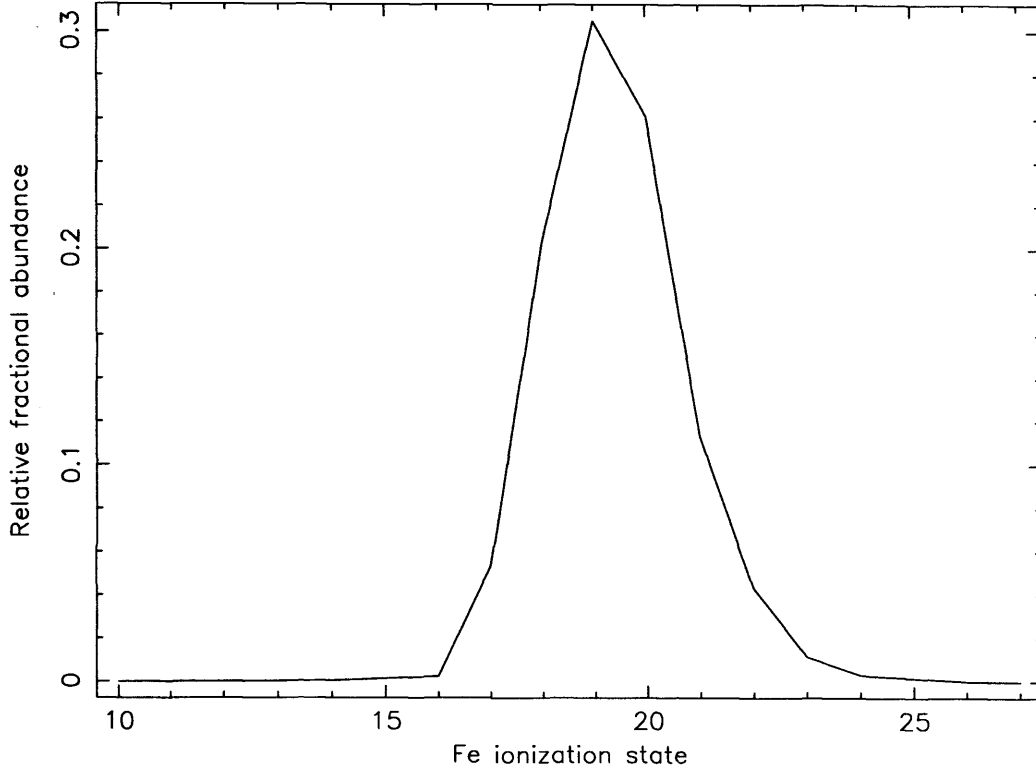


Figure 3.4: Relative fractional abundance for different ionization states of iron in a photoionized medium where $\log \xi \sim 2.8$ and $N_{H_{\text{scat}}} \sim 1.7 \times 10^{23} \text{ cm}^{-2}$.

2 galaxy). This “warm absorbing” medium would presumably lie inside the colder medium responsible for the bulk of the soft X-ray cut-off, a situation which is quite plausible if the cold gas distribution is associated with a molecular torus in Mrk 3. This twin absorbing-zone model was investigated by including a warm column density $N_{H_{\text{warm}}}$ in addition to the cold column N_H in a revised version of Model 5. Again for simplicity the same mtable as described earlier was used and the ionization parameter of the warm absorber was tied to that of the scattering medium. The results of this analysis are given in Table 3.3 as Model 7. Note that the fit is an improvement on both Models 5 and 6. The inferred spectral index of the hard continuum in this “no-reflection” scenario is $\alpha \approx 0.7$; a value which was considered typical of the underlying hard continuum in Seyfert 1 galaxies prior to the realisation of the importance of the Compton reflection process (e.g. Turner & Pounds 1989). Finally, the requirement for a warm-absorber is not diminished if a reflection component is added to Model 7; however, this model has not been pursued further given its complexity in relation to the quality of the available data.

3.4 Discussion

3.4.1 Characteristics of the hard X-ray spectrum of Mrk 3

Gross spectral variability in Mrk 3 might, in principle, be revealed as a mismatch between the *Ginga*, *ASCA* and *ROSAT* spectral datasets. In fact a rather good fit is obtained to the composite spectrum without the need for any cross-instrument scaling factors (this also demonstrates that the instrument calibrations are not too far out of line). Thus the initial assumption that the spectral form of Mrk 3, within the limitations of the available observations, is largely invariant turns out to be correct. Specifically the soft X-ray spectrum of Mrk 3 (below ~ 3 keV) shows no significant change over the six week period separating the *ROSAT* and *ASCA* observations and similarly the form of the spectral cut-off due to photoelectric absorption of the hard continuum flux remained relatively constant over the 3.5 year period between the *Ginga* and *ASCA* observations. In combination the *Ginga* and *ASCA* data give reasonably tight constraints on the spectral slope of the hard continuum, α , albeit in a model dependent way (as illustrated by the spread in values in Table 3.3). In practice we cannot exclude modest temporal variations in α on the basis of the available datasets.

The two “untied” parameters in the spectral fitting were the normalisation of the intrinsic power-law continuum and the flux of the iron K_α line. The inferred absorption corrected flux of the hard X-ray source in the 2–10 keV band at the time of the *Ginga* observations is 6.1×10^{-11} erg cm $^{-2}$ s $^{-1}$, whereas in the *ASCA* observations the value is 1.3×10^{-11} erg cm $^{-2}$ s $^{-1}$ (these and subsequent values quoted in this section are based on Model 5). Thus variability in the continuum level by a factor ~ 4.7 is implied. As previously noted by Iwasawa *et al.* (1994), an observation by BBXRT (Marshall *et al.* 1992) made roughly 14 months after the *Ginga* observation gave an X-ray flux a factor 2 below the *Ginga* level.

The observed iron-line flux decreased by a factor of 1.8 between the *Ginga* and *ASCA* observations, substantially less than the corresponding continuum variation. Consequently the observed equivalent width of the iron K_α line (measured relative to the *absorbed* continuum) shows an increase from 425 to 1110 eV over the same interval. The measured iron-line energy, corrected for a redshift $z = 0.0137$, is $E_{K_\alpha} = 6.38 \pm 0.03$ keV consistent with neutral iron. A possible origin for the iron K_α emission is in the fluorescence of an extensive distribution of cold gas surrounding

the nucleus of Mrk3, possible in the form of a torus. Our specific line of sight to the the source of the hard X-ray continuum gives a column density $N_H = 7.7 \times 10^{23} \text{ cm}^{-2}$, which if applicable over 4π steradians implies an iron-line equivalent width of $\sim 500 \text{ eV}$ (Leahy & Creighton 1993). Given the uncertainty as to whether the *Ginga* or *ASCA* continuum level is more representative of the average long-term luminosity of Mrk 3 and the lack of detailed knowledge concerning both the coverage fraction and iron abundance of the fluorescing gas, it is plausible that the bulk of the observed iron line emission originates in this fashion. However, Compton reflection from the surfaces of optically thick media, such as a putative accretion disk or the inner walls of sections of the torus, may also contribute to the 6.4 keV iron line. Comparison of the *Ginga* and *ASCA* data demonstrates that hard X-ray variability is seen down to $\sim 4.5 \text{ keV}$ (see Fig. 3.2) in Mrk 3 and suggests a direct view of the power-law continuum (albeit with some losses due to the line-of-sight absorption) down to this energy. In this case the predicted contribution to the equivalent width of the iron line measured with respect to the observed continuum is $\lesssim 300 \text{ eV}$ (e.g. George & Fabian 1991; Krolik, Madau & Życki 1994; Ghisellini, Haardt & Matt 1994). The observed decline of the iron line flux between the *Ginga* and *ASCA* observations demonstrates that this line does show some response on time-scales of a few years, which in turn requires at least one of the line emitting regions to have a dimension not much more than about a light year. It would seem more likely that this scale size corresponds to an accretion disk or inner (optically thick) cloud structure rather than the inner extent of the putative molecular torus. In any event, milliarcsec resolution will be required to image this spatial structure.

The profile of the iron K_α line in Mrk 3 is probably complex. For example, in the archetypal Seyfert 2 galaxy, NGC 1068, up to four line components have been spectrally resolved in the 6–7 keV energy band in *ASCA* observations (with a summed line photon flux which is ~ 3 times higher than is the case for Mrk 3) (Ueno *et al.* 1994; Iwasawa, Fabian & Matt 1997). The identified line features include a 6.4 keV line, probable He-like and H-like iron K_α components and also the hint of a “Compton shoulder” feature on the 6.4 keV line (Iwasawa, Fabian & Matt 1997). The He-like and H-like lines have been attributed to a warm scattering region (Marshall *et al.* 1993; Matt, Brandt & Fabian 1996) which is probably smaller in extent than the optical/UV mirror in this source (Iwasawa, Fabian & Matt 1997). Some evidence for underlying complexity in the iron K_α line is provided, in the case of Mrk 3, by the fact that in the spectral fitting χ^2 is minimized when the width of the 6.4 keV is fixed at a measurable value, namely $\sigma_{K_\alpha} = 0.1$

keV. (In Model 5, Table 3.3 the χ^2 increased by ~ 6 when the line-width was reduced by a factor of 2). The origin of such broadening could be due to gravitational redshift and Doppler effects in an accretion disk (e.g. Tanaka *et al.* 1995; Yaqoob *et al.* 1995; Nandra *et al.* 1997) or the superposition of different line components. For example, our photoionized scatterer model predicts up to 20% of the iron K_α flux observed by ASCA will be in the form of Fe XVII - XXIII, although this does not account for all of the apparent line broadening in Mrk 3.

Although previous studies have suggested that the power-law continuum in Mrk 3 is unusually hard (e.g. Awaki *et al.* 1990; Awaki *et al.* 1991; Smith & Done 1996) as discussed in § 3.3.3, a value for the energy spectral index of $\alpha \sim 0.8$, obtained from this work, is well within the range of values seen in Seyfert 1 galaxies (Nandra & Pounds 1994; Reynolds 1997; George *et al.* 1998). Even without reflection an $\alpha \sim 0.7$ is required if an inner warm-absorber is included to reproduce the ~ 8 keV absorption edge apparent in the *Ginga* spectra. The best fitting reflection model (Model 6, Table 3.3) requires a reflection component of only modest strength (i.e. $R \sim 0.8$), which contributes significantly to the observed spectrum only above 10 keV. Recently, Georgantopoulos *et al.* (1999) reported the results of 12 monitoring observations of Mrk 3 with the Rossi X-ray Timing Explorer (RXTE). A model, similar to Model 6 above, consisting of a power-law, with α fixed at 0.8, and reflection component, both of which were absorbed by cold gas, plus Fe K_α emission gave a very good fit to PCA data in the 4 - 20 keV range (however see below). The inferred column density for the cold gas of $N_H = 7.5 \pm 3.0 \times 10^{23} \text{ cm}^{-2}$ is in very good agreement with that obtained from *Ginga* /ASCA data (Model 6, Table 3.3).

An alternative description of the hard X-ray spectrum of Mrk 3 was suggested by Turner *et al.* (1997b) in which the reflection component is effectively free of absorption and contributes the bulk of the observed flux between 3–10 keV. In this model the intrinsic power-law continuum suffers line-of-sight absorption by a cold gas column density $N_H \approx 1.3 \times 10^{24} \text{ cm}^{-2}$ (roughly a factor of 2 higher than reported here) and is thus strongly suppressed below ~ 6 keV. In fact, Georgantopoulos *et al.* (1999) claimed that the RXTE data preferred this model to the absorbed reflection model previously mentioned, although the quality of the data was not good enough to be able to exclude either model in favour of the other. Cappi *et al.* (1999a) also found that the Turner *et al.* (1997b) model (consisting of an absorbed hard power-law continuum, unabsorbed reflection, Fe K_α emission and a soft power-law component) gave the best description to new broad-band (0.6 - 150 keV) observations of Mrk 3 obtained with BeppoSAX. These authors point

out the difficulty of fitting the complex spectrum of Mrk 3 using data of only limited bandpass. They showed that a model, consisting of a hard, absorbed power-law and a second scattered power-law, fit to data below 10 keV was, when extrapolated to higher energies, inconsistent with PDS data. They did not attempt to fit the absorbed reflection model to the hard (5 - 150 keV) X-ray spectrum of Mrk 3 hence it seems that this ambiguity between differing interpretations still exists. The current analysis demonstrates that continuum variability is observed in Mrk 3 down to ~ 4.5 keV with little evidence for a changing spectral form. If the continuum above 4.5 keV represents the combination of reflection and a very heavily obscured power-law component, as in the Turner *et al.* model, this would require the reflection component to track the power-law at a rate at least comparable to the intrinsic variability time-scale (i.e. a time-scale shorter than \sim a year). One advantage of the Turner *et al.* (1997b) model is that the large iron-line equivalent width measured by ASCA can be readily explained; however, as discussed earlier, when the continuum variability is taken into account, the ASCA measurement can also be reconciled with the current model in which the power-law component is observed directly down to ~ 4.5 keV.

3.4.2 The nature of the soft X-ray emission in Mrk 3

The soft X-ray excess in the spectrum of Mrk 3 (which dominates the spectrum below ~ 3 keV) has been modelled either as a blend of an electron scattered power-law continuum with a soft thermal component (Model 4) or an absorbed continuum scattered from a hot photoionized medium, with line emission from the same region superimposed (Model 5). These scenarios are now considered in turn.

In Model 4, a substantial fraction of the soft X-ray luminosity is explained as emission from a Raymond-Smith plasma at a temperature of ~ 0.7 keV. A possible origin of this emission is in shock heated gas associated with a nuclear starburst in Mrk 3. The ROSAT HRI measurements of Morse *et al.* (1995) constrain the X-ray emitting region in Mrk 3 to be < 4 kpc, and thus do not exclude the presence of a nuclear starburst. In a recent study of the ASCA spectra of a large sample of Seyfert 2/Narrow Emission Line Galaxies, Turner *et al.* (1997a) used far infrared luminosities to estimate an upper limit to the fraction of the soft X-ray flux that could arise from starburst activity (following the method first discussed by David, Jones & Forman 1992). On this basis Turner *et al.* (1997a) concluded that in Mrk 3 no more than 6×10^{40} erg s $^{-1}$ in the

0.5–4.5 keV band could be thermal emission powered by starbursts, which represents only 5% of the total 0.5–4.5 keV luminosity of the source. The thermal component in Model 4 has a 0.5–4.5 keV luminosity of $2.1 \times 10^{41} \text{ erg s}^{-1}$ (corrected for Galactic absorption), a factor 3.5 higher than the prediction. However the scatter in the correlation between the soft X-ray and far-infrared luminosity in the sample of normal and starburst galaxies studied by David, Jones & Forman (1992) is of the same order; hence a starburst origin for the thermal emission is not excluded. An alternative possibility is that the thermal emission arises in gas which is energised by the radio jet in Mrk 3 and possibly associated with the small-scale bar ($0.35'' \times 1''$) of continuum emission seen in the recent *HST* observation of Mrk 3 (Capetti *et al.* 1995).

The Raymond-Smith component contributes 23% of the observed 0.3–3 keV emission (see Fig. 3.3(a)) with the electron scattered component accounting for the remainder. The scattered fraction, f_{scat} , of the hard continuum flux is $A_{\text{soft}}/A_{\text{Ginga}} \approx 2.7\%$ (or as high as $\approx 12\%$ if the level of the hard continuum in the ASCA observation is more representative of the time averaged behaviour of the source). For comparison Schmidt & Miller (1985) estimate that the scattered fraction is $< 10\%$ based on the degree of polarization in the optical spectrum of Mrk 3. The column density of the scattering medium can be estimated from the fraction f_{scat} , since $f_{\text{scat}} = \frac{\Omega}{4\pi} \tau_s$ where Ω is the solid angle subtended by the scatterer (as viewed from the continuum source) and τ_s is the electron scattering optical depth given by $\tau_s = 1.2 \sigma_T N_{H_{\text{scat}}}$, where σ_T is the Thomson electron scattering cross-section and is equal to $6.6 \times 10^{-25} \text{ cm}^2$. Using the lower of the two estimates for the scattered fraction and taking $\frac{\Omega}{4\pi} = 0.25$ then $N_{H_{\text{scat}}} \sim 1.3 \times 10^{23} \text{ cm}^{-2}$.

Turning to the alternative description of the soft X-ray spectrum of Mrk 3, in Model 5 the scattering region is not completely photoionized and thus imprints both absorption and emission features on the emergent spectrum. The value for the column density, $N_{H_{\text{scat}}} \sim 1.7 \times 10^{23} \text{ cm}^{-2}$, obtained from the spectral fitting is consistent with the previous estimate of a scattered fraction of $\sim 3\%$. The ionization parameter of $\log \xi \sim 2.8$ corresponds to iron ionization states in the range Fe XVII - XXIII and oxygen either in a hydrogenic or fully ionized form (O VIII - IX) (see Fig 3.4; Kallman & McCray 1982). Although this is on the high side of the range, it is not totally atypical of the degree of ionization inferred for the warm absorbers seen in Seyfert 1 galaxies (Reynolds 1997; George *et al.* 1998). The plasma temperature was assumed to be 10^6 K , which is hotter than the warm scattering medium that acts as an optical/UV mirror in NGC 1068 (Miller, Goodrich & Mathews 1991). This is also above the limit of thermally stability

in the photoionization models considered by Netzer (1993) and Netzer (1996). However, the plasma state is similar to the case considered by Krolik & Kriss (1995) (their model a), where the scattering region is identified as an X-ray heated wind which is in ionization equilibrium but not necessarily radiative equilibrium. Empirically reducing the plasma temperature to either $10^{5.5}$ or 10^5 K produces a set of photoionization models which provides a somewhat poorer best fit to the observational data, particularly near the 0.9 keV feature (see below), although many of the details of the spectral model are similar for plasma temperatures in the range 10^{5-6} K. Tran (1995) notes that the observed FWHM of the polarized broad $H\beta$ in Mrk 3 is 6000 km s^{-1} , implying that the temperature of the electrons which scatter the optical light is less than 4×10^5 K. The confirmation of a 10^6 K component through X-ray spectroscopy might thus require thermal stratification of the scattering medium.

The observed feature in the *ASCA* spectrum near ~ 0.9 keV is explained as recombination directly into the K-shell of fully ionized oxygen atoms; the resulting O VIII recombination continuum is broadened by the thermal energies of the electrons in the 10^6 K plasma. Fig. 3.3(b) (and also Fig. 3.3(a)) also shows a prominent line feature at 0.65 keV due to the O VIII $\text{Ly}\alpha$ line, with an equivalent width of ~ 30 eV. The observational evidence for this feature is marginal given that when the line is removed from the spectral model the result is a change in the χ^2 of less than 1. Similarly the model also predicts weak spectral features in the energy band from 1.8–3 keV due to silicon and sulphur which are currently at the limit of detectability with *ASCA*.

The scale of the X-ray scattering region in Mrk 3 can be estimated from the derived value of the ionization parameter and the model assumptions. We obtain a radius $r = 5 \times 10^{17} n_6^{-0.5} \text{ cm} \sim 0.2 n_6^{-0.5} \text{ pc}$ (where n_6 is the density in units of $n = 10^6$ hydrogen nuclei cm^{-3}). The measured column density through the scattering region leads to an estimate of the thickness of the scatterer of $l = 1.7 \times 10^{17} n_6^{-1.0} \text{ cm}$. Then requiring that $l \lesssim r$, it follows that $n_6 \gtrsim 0.1$. The implied scale of the scattering region (\sim a light year) is comparable to the inner extent of the cold fluorescing gas as inferred from the variability in the iron-line flux.

Finally, a complication that should be noted is that the predicted normalisation of the emission spectrum is a factor ~ 2 times higher than the best fitting value. This apparent preference for scattered continuum as opposed to intrinsic emission from the photoionized region may reflect

the fact that the representation of the spectral form of the incident continuum in the soft X-ray band, as a straight downward extrapolation of the hard power-law, may not be adequate. For example, the (hidden) intrinsic nuclear spectrum in Mrk 3 may show an upturn somewhere in the 0.3–3 keV band similar to that seen in some unobscured Seyfert 1 nuclei (e.g. George *et al.* 1998). Alternatively, a fraction of the scattered continuum could come from a region which is either closer to the central source or less dense and completely ionized.

Chapter 4

A sample of heavily obscured Seyfert 2 galaxies

4.1 Introduction

Hard X-ray spectroscopy has revealed that all X-ray detected Seyfert 2s have large column densities ($N_H > 10^{22} \text{cm}^{-2}$) of cold material in the line-of-sight to the central continuum source (e.g. Awaki *et al.* 1991; Smith & Done 1996). Furthermore, most of them have strong fluorescent Fe K_α line emission which is indicative of reprocessing of the intrinsic continuum, with typical Seyfert 2 galaxies having equivalent widths (EW) of several hundred eV and Compton thick sources, such as NGC 1068, having $\text{EW} \sim 1.3 \text{ keV}$ (Awaki *et al.* 1991). There is still much to be learnt about properties such as geometry, distance from central engine and the physical state of this obscuring material which seems ubiquitous in Seyfert 2 galaxies. Possible variability in the column density of this material has only been reported for two Seyfert 2s so far, namely ESO 103-G35 (Warwick, Pounds & Turner 1988) and NGC 7582 (Warwick *et al.* 1993; Xue *et al.* 1999). Warwick, Pounds & Turner (1988), from multiple *EXOSAT* observations, reported a factor of two variation in the line-of-sight column to ESO 103-G35, which they interpreted as broad-line clouds moving out of the line-of-sight to the X-ray source. Warwick *et al.* (1993) reported a large increase in N_H towards NGC 7582 ($\sim 3 \times 10^{23} \text{ cm}^{-2}$) over a 4 year period between *EXOSAT* and *Ginga* observations. Xue *et al.* (1999) also detected column density variability in NGC 7582, an increase of $4 \times 10^{22} \text{ cm}^{-2}$ ($\sim 44\%$) during the two years between *ASCA* observations, consistent with the scenario that the absorbing material is a “patchy torus” made up of many individual

clouds with dimensions large enough to cover the X-ray source. Other sources that show evidence of N_H variability are Cen A (Morini, Anselmo & Molteni 1989), MR 2251-179 (Halpern 1984) and NGC 4151 (e.g. Yaqoob *et al.* 1993 and references therein; see also § 4.3). In addition Malizia *et al.* (1997), using a catalog of published high-energy spectra, reported evidence for N_H variability in several other Seyfert galaxies.

Here *non-simultaneous* *Ginga* and *ASCA* observations are used to analyse the mid - hard (1.5 - 20.0 keV) X-ray spectrum of the Seyfert 2 galaxies Mrk 348, NGC 4507, ESO 103-G35, IC 5063 and NGC 7172 (the observation log for these objects is given in Table 2.2). This chapter focuses on the hard X-ray spectrum and heavy absorption observed in these galaxies, which were selected from the *Ginga* sample of ~ 16 Seyfert 2 galaxies because they all had an inferred column density $10^{23} < N_H < 10^{24} \text{ cm}^{-2}$. In these cases the benefits of combining data from both *Ginga* and *ASCA* are maximised. The energy ranges of *Ginga* and *ASCA* overlap at the point where the hard continuum is strongly cut-off by obscuring material; hence the combined spectra enable tighter constraints to be obtained on both the spectral index of the intrinsic continuum and line-of-sight column. Using the same approach as for Mrk 3 (chapter 3) the *Ginga* and *ASCA* spectra are considered separately before analysing the combined datasets. The complex and varying X-ray spectrum of the Seyfert 1.5 galaxy NGC 4151 is also analysed using multiple *ASCA* observations.

4.2 Spectral analysis of the Seyfert 2 galaxies

4.2.1 The *Ginga* spectra

Just as with Mrk 3 (§ 3.3.1), the first model used to fit the *Ginga* LAC spectra of all five Seyfert 2 galaxies was a single power-law continuum attenuated by a high column density ($N_H \gtrsim 10^{23} \text{ cm}^{-2}$) of cold gas plus an iron K_α line with a fixed width of $\sigma_{K_\alpha} = 0.1 \text{ keV}$. The spectrum of NGC 4507 showed evidence for an over-subtraction of the Cosmic X-ray Background (CXB) in the top-layer of the LAC which resulted in a negative count-rate below $\sim 4 \text{ keV}$. This over-subtraction is a consequence of fluctuations in the CXB (see Hayashida *et al.* 1989; Butcher *et al.* 1997). When modelling the *Ginga* spectrum of NGC 4507, therefore, a fluctuation spectrum is included, which can be described as a power-law of energy index $\alpha = 0.8$ and normalisation

which is allowed to vary between -1.0×10^{-3} and 1.0×10^{-3} photons $\text{cm}^{-2} \text{sec}^{-1} \text{keV}^{-1}$ at 1 keV. The best-fit parameters and associated errors for all five sources (i.e. 90% confidence for one interesting parameter) using the above model (Model 1) are listed in Table 4.1. The Model 1 fit is very good for NGC 4507 and IC 5063 but unsatisfactory for Mrk 348, ESO 103-G35 and NGC 7172. The fitting residuals for Mrk 348 indicate that the top- and mid-layer data are inconsistent below ~ 10 keV. Ignoring mid-layer data below 10 keV significantly improved the fit ($\chi^2/\text{dof} = 48.6/40$) but had virtually no impact on the best-fit parameter values, hence the mid-layer data < 10 keV in any future analysis of Mrk 348 is ignored. This action does not diminish the benefits of using mid-layer data because the effective area of the mid-layer drops off rapidly below 10 keV compared to the top-layer (see Figure 2.2). The mid-layer data of ESO 103-G35, however, is inconsistent with the top-layer above and below 10 keV and is therefore not used at all. The residuals of both ESO 103-G35 (top-layer only) and NGC 7172 show a deficit of flux between ~ 7 -10 keV and seem to require additional iron K absorption (edge of energy E_{edge} and optical depth τ_{edge}). The iron-K edge and emission line energies were fixed at values corresponding to $E_{\text{edge}} = 7.11$ keV and $E_{\text{K}\alpha} = 6.4$ keV in the source's rest frame, representing absorption and emission from cold/low ionization gas. This model (Model 2; Table 4.2) gives a much improved fit and implies an Fe abundance relative to solar of ~ 1.6 and 1.5 for ESO 103-G35 and NGC 7172 respectively. The parameter values derived on the basis of either Model 1 or 2 agree reasonably well with earlier analyses of the *Ginga* (top-layer only) spectra (Awaki *et al.* 1991; Warwick *et al.* 1993; Smith & Done 1996). All five objects can be confirmed to have inferred column densities $N_H \gtrsim 10^{23} \text{cm}^{-2}$. The energy indices, α , of the power-law continuum derived for Mrk 348, ESO 103-G35, IC 5063 and NGC 7172 are consistent with those typically observed for Seyfert 1 galaxies (Nandra & Pounds 1994) while the continuum slope derived for NGC 4507 is somewhat harder.

4.2.2 The ASCA spectra

Several of the objects studied here have complex soft X-ray spectra and show evidence of sharp emission features at ~ 1 keV. Therefore, for the purpose of this analysis, data below 1.5 keV is ignored. The very interesting soft X-ray spectra of these objects is discussed in chapter 5 (§ 5.5). Table 4.3 gives the best-fit parameters to the ASCA SIS and GIS data using Model 1 where all five parameters mentioned in the previous section were allowed to vary. Because of

Table 4.1: Model 1 fit to Ginga data

Parameter	Mrk 348	NGC 4507	ESO 103-G35	IC 5063	NGC 7172
α	0.61 ± 0.11	$0.27^{+0.15}_{-0.14}$	0.69 ± 0.07	$0.40^{+0.19}_{-0.21}$	0.82 ± 0.03
A_{Ginga}^a	$0.47^{+0.14}_{-0.10}$	$0.60^{+0.31}_{-0.19}$	$1.02^{+0.20}_{-0.16}$	$0.31^{+0.19}_{-0.13}$	$2.17^{+0.16}_{-0.15}$
N_H^b	$10.5^{+1.6}_{-1.5}$	$35.7^{+5.9}_{-5.3}$	$18.9^{+1.4}_{-1.3}$	$21.0^{+4.4}_{-4.5}$	10.4 ± 0.4
$E_{K\alpha}^c$	$6.24^{+0.32}_{-0.30}$	6.29 ± 0.10	6.18 ± 0.10	6.14 ± 0.19	$6.38^{+0.50}_{-0.60}$
$A_{K\alpha}^d$	$3.1^{+2.1}_{-1.8}$	$12.7^{+2.6}_{-2.7}$	9.9 ± 1.8	$6.2^{+2.5}_{-2.3}$	2.5 ± 1.9
χ^2	74.7	26.2	88.4	38.8	63.0
d.o.f.	47	48	46	47	46

^a 10^{-2} photon $\text{cm}^{-2} \text{s}^{-1} \text{keV}^{-1}$.

^b 10^{22}cm^{-2} .

^c keV.

^d 10^{-5} photon $\text{cm}^{-2} \text{s}^{-1}$.

Table 4.2: Model 2 fit to Ginga data

Parameter	ESO 103-G35	NGC 7172
α	$0.84^{+0.08}_{-0.04}$	0.80 ± 0.03
A_{Ginga}^a	$1.53^{+0.33}_{-0.27}$	$2.14^{+0.15}_{-0.14}$
E_{edge}^c	7.11 (fixed)	7.11 (fixed)
τ_{edge}	0.15 ± 0.06	$0.06^{+0.04}_{-0.03}$
N_H^b	21.9 ± 1.4	10.4 ± 0.3
$E_{K\alpha}^c$	6.40 (fixed)	6.40 (fixed)
$A_{K\alpha}^d$	$6.3^{+1.7}_{-2.1}$	$1.8^{+2.0}_{-1.8}$
χ^2	17.7	54.9
d.o.f.	24	46

^a 10^{-2} photon $\text{cm}^{-2} \text{s}^{-1} \text{keV}^{-1}$.

^b 10^{22}cm^{-2} .

^c keV.

^d 10^{-5} photon $\text{cm}^{-2} \text{s}^{-1}$.

the increased energy resolution of the ASCA instruments compared to *Ginga*, the width of the iron line is fixed at 0.05 keV, which is smaller than the instruments' spectral resolution at ~ 6 keV. The presence of additional soft X-ray flux over and above the amount predicted by a simple cut-off power-law is obvious in almost all of the observations, the exception being that this soft excess seems to be present in only one out of the two ASCA observations of NGC 7172. To account for this soft excess a second power-law is added to Model 1 with the same energy index as that of the hard continuum but a different normalisation, A_{soft} . The best-fit values for the six free parameters in this model (Model 3) are listed in Table 4.4. The ASCA data for the majority of these objects, apart from Mrk 348 and the second observations of ESO 103-G35 and NGC 7172, have also been analysed by Turner *et al.* (1997a). The results of Model 3, which is analogous to the Scattering/Partial-Covering model in Turner *et al.* (1997a), are consistent with those obtained by these authors. However, when the individual fits obtained using *Ginga* are compared with those of ASCA, there does seem to be some discrepancies between the energy indices and/or column densities derived from the two instruments for Mrk 348, NGC 4507 and NGC 7172. The confidence contours for the photon index, $\Gamma (\equiv \alpha + 1)$, and column density are given in Figure 4.1; these show that for Mrk 348, NGC 4507 and NGC 7172 it is not possible to obtain values for the spectral index *and* column that are consistent with both the *Ginga* and ASCA data. The 2-10 keV flux of NGC 7172 is a factor > 3 less during the second ASCA observation ($F_{2-10} \sim 1.3 \times 10^{-11}$ erg cm $^{-2}$ s $^{-1}$) than during the first ASCA or the *Ginga* observation ($F_{2-10} \sim 4.3 \times 10^{-11}$ and 4.1×10^{-11} erg cm $^{-2}$ s $^{-1}$ respectively). Because of the poorer S/N ratio the spectral index and N_H obtained from the second ASCA observation are less tightly constrained and therefore are consistent, at the 90% level, with those derived from the *Ginga* and first ASCA dataset. However, it is obvious that the earlier ASCA and *Ginga* data are inconsistent at even the 99% confidence level. It is important to note that because of the limited energy band-width of the ASCA instruments and the fact that the hard continuum of these objects are heavily cut-off at soft X-ray energies it is very difficult to constrain the slope of the intrinsic continuum using ASCA data alone. In an attempt to better understand the X-ray spectra of these objects and iron out any disparity between the different datasets the best approach is to fit the *Ginga* and ASCA data simultaneously.

Table 4.3: Model 1 fit to ASCA SIS/GIS data

Parameter	Mrk 348	NGC 4507	ESO 103-G35		IC 5063		NGC 7172	
			1	2	1	2	1	2
α	$0.39^{+0.17}_{-0.25}$	$0.26^{+0.16}_{-0.15}$	$0.58^{+0.25}_{-0.24}$	$0.53^{+0.42}_{-0.38}$	$0.35^{+0.21}_{-0.47}$	$0.45^{+0.17}_{-0.18}$	0.65 ± 0.09	$0.53^{+0.14}_{-0.14}$
A_{ASCA}^a	$0.12^{+0.08}_{-0.02}$	$0.66^{+0.27}_{-0.18}$	$0.7^{+0.51}_{-0.30}$	$0.7^{+0.91}_{-0.42}$	$0.37^{+0.28}_{-0.21}$	$0.52^{+0.25}_{-0.17}$	$1.53^{+0.29}_{-0.23}$	$0.37^{+0.10}_{-0.07}$
N_H^b	$12.5^{+2.1}_{-1.9}$	$27.5^{+2.0}_{-1.9}$	$19.4^{+1.1}_{-2.2}$	$15.9^{+3.3}_{-3.0}$	$18.9^{+2.5}_{-4.1}$	$19.1^{+1.4}_{-1.7}$	8.2 ± 0.4	$8.1^{+0.7}_{-0.6}$
$E_{K\alpha}^c$	6.27 ± 0.07	$6.32^{+0.04}_{-0.02}$	$6.47^{+0.18}_{-0.10}$	6.25 ± 0.08	$6.34^{+0.15}_{-0.14}$	6.30 ± 0.06	6.40 ± 0.08	6.32 ± 0.07
$A_{K\alpha}^d$	$1.5^{+0.5}_{-0.6}$	$8.5^{+1.4}_{-1.2}$	$5.5^{+1.7}_{-2.2}$	$10.4^{+5.2}_{-3.2}$	3.5 ± 1.9	$3.6^{+0.8}_{-1.6}$	$5.4^{+3.4}_{-1.9}$	2.8 ± 1.0
χ^2	346.8	897.2	224.1	52.9	164.6	514.3	668.6	420.2
d.o.f.	313	425	205	80	134	408	631	452

^a 10^{-2} photon cm^{-2} s^{-1} keV^{-1} .^b 10^{22} cm^{-2} .^c keV.^d 10^{-5} photon cm^{-2} s^{-1} .

Table 4.4: Model 3 fit to ASCA SIS/GIS data

Parameter	Mrk 348	NGC 4507	ESO 103-G35		IC 5063		NGC 7172	
			1	2	1	2	1	2
α	$0.69^{+0.10}_{-0.19}$	$0.61^{+0.15}_{-0.14}$	$0.68^{+0.28}_{-0.27}$	$0.78^{+0.46}_{-0.44}$	$0.57^{+0.36}_{-0.35}$	$0.64^{+0.18}_{-0.17}$	$0.65^{+0.10}_{-0.09}$	0.65 ± 0.15
A_{ASCA}^a	$0.22^{+0.14}_{-0.08}$	$1.47^{+0.53}_{-0.37}$	$0.9^{+0.6}_{-0.4}$	$1.3^{+1.9}_{-0.7}$	$0.61^{+0.66}_{-0.31}$	$0.79^{+0.35}_{-0.24}$	$1.54^{+0.31}_{-0.22}$	$0.47^{+0.15}_{-0.11}$
N_H^b	$16.4^{+1.8}_{-1.5}$	$35.2^{+1.8}_{-1.7}$	$20.9^{+2.5}_{-2.4}$	$19.4^{+4.2}_{-4.0}$	$23.6^{+3.5}_{-3.4}$	22.4 ± 1.7	$8.2^{+0.5}_{-0.4}$	9.1 ± 0.9
$E_{K\alpha}^c$	6.27 ± 0.07	$6.32^{+0.04}_{-0.02}$	$6.47^{+0.19}_{-0.10}$	6.26 ± 0.08	$6.34^{+0.19}_{-0.16}$	6.30 ± 0.06	$6.40^{+0.07}_{-0.08}$	6.32 ± 0.07
$A_{K\alpha}^d$	1.32 ± 0.5	$7.1^{+1.4}_{-1.3}$	5.1 ± 1.9	10.1 ± 4.1	3.0 ± 1.9	2.9 ± 1.1	6.1 ± 2.5	2.7 ± 1.0
A_{soft}^a	$0.0041^{+0.0015}_{-0.0014}$	0.016 ± 0.002	0.004 ± 0.003	$0.014^{+0.015}_{-0.011}$	$0.010^{+0.005}_{-0.003}$	0.008 ± 0.002	$0.0004^{+0.0047}_{-0.0004}$	0.0045 ± 0.0027
χ^2	306.2	489.3	218.0	48.2	129.7	442.3	668.3	412.6
d.o.f.	312	424	204	79	133	407	630	451
$\Delta\chi^2$								

^a 10^{-2} photon $\text{cm}^{-2} \text{s}^{-1} \text{keV}^{-1}$.^b 10^{22}cm^{-2} .^c keV.^d 10^{-5} photon $\text{cm}^{-2} \text{s}^{-1}$.

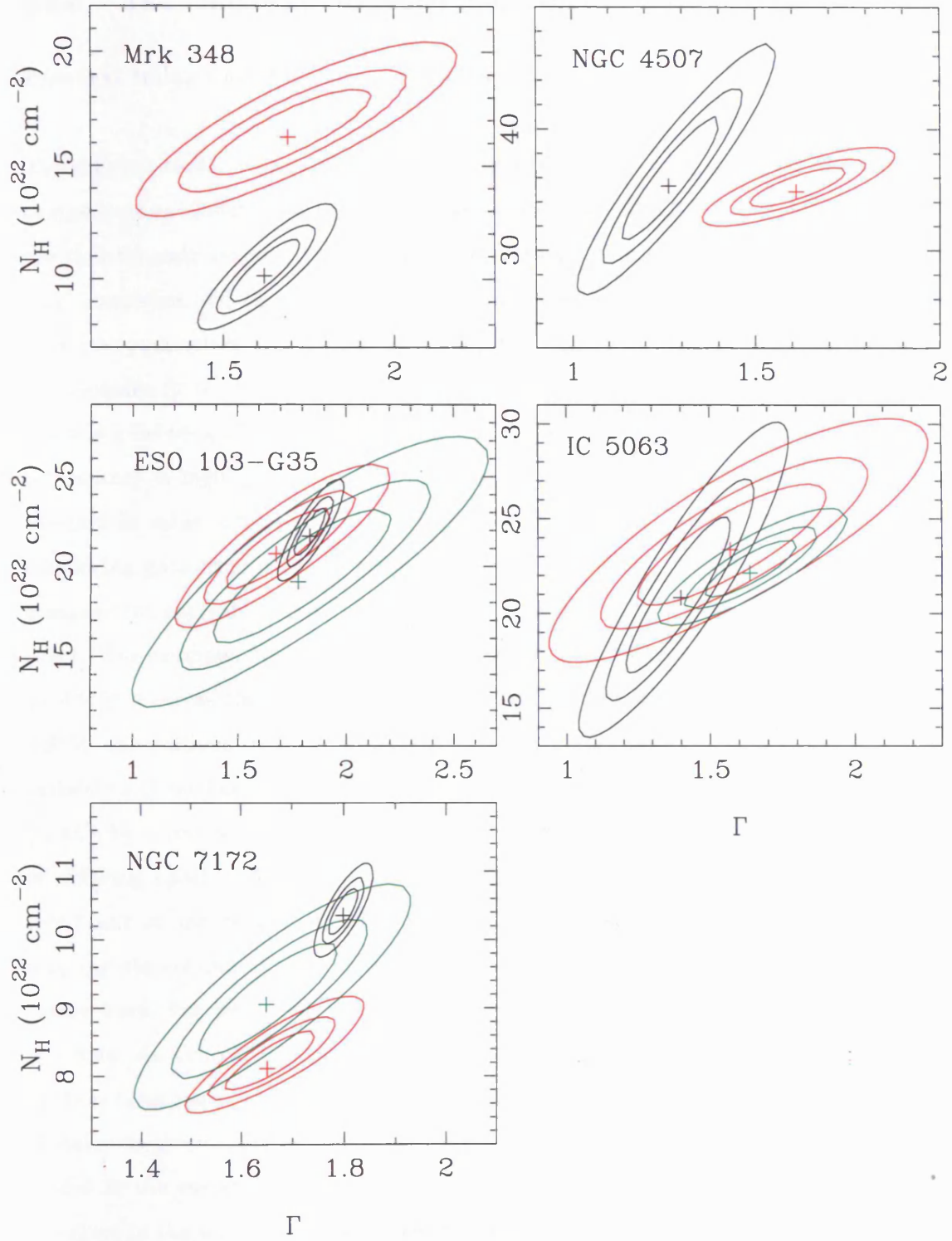


Figure 4.1: Confidence contours for the photon index (Γ) and column density (N_H) parameters. The contours correspond to $\Delta\chi^2 = 2.30, 4.61$ and 9.21 which is 68, 90 and 99 percent confidence respectively for two interesting parameters. Black, red and green contours represent *Ginga*, ASCA (1) and ASCA (2) data respectively.

4.2.3 The composite *Ginga* and *ASCA* spectra

Spectral Index and Absorbing Column

The simplest model used to describe the composite *Ginga*/*ASCA* spectra is made up of the same components as Model 3. Once again, as was the case with Mrk 3 (§ 3.3.3), the initial assumptions are that the only spectral features that vary between observations are the normalisation of the hard power-law and the flux of the Fe K $_{\alpha}$ line. This model (hereafter Model 3a) has between 8–10 free parameters, the best-fit values of which are listed in Table 4.5. While Model 3a gives a reasonable fit to the data of all five galaxies, it is obvious from the residuals that there is a difference between *Ginga* and *ASCA* at soft X-ray energies (< 4 keV) in several objects. This discrepancy is highlighted when we fix the column density observed by *Ginga*, $N_{H\text{ }Ginga}$, to the best-fit value obtained by *ASCA* alone (see Figure 4.2). An important point to note when comparing data from different instruments is the possibility of a systematic offset because of cross-instrument calibration. As can be seen in Figure 4.2 there is no evidence of such an effect. For example, the *Ginga* data of Mrk 348 prefers more flux at soft energies compared to *ASCA* whereas the *Ginga* data of NGC 7172 prefers less flux. In contrast the *Ginga* and *ASCA* observations of IC 5063 agree very well. The observed effects can be attributed to variability of the line-of-sight absorption to the central nucleus. Model 3b (Table 4.6) accounts for this by allowing the column density of the cold absorber to be untied between observations of differing epoch. Model 3b gives an improvement in χ^2 which, in terms of the F-test, is significant at the $> 99.9\%$ level for Mrk 348, NGC 4507 and NGC 7172. Also note that allowing the column to vary between *Ginga* and *ASCA* observations of NGC 4507, while still rather hard, has produced a significant increase in the energy index of $\Delta\alpha \sim 0.17$ to give $\alpha \sim 0.44$. As a check, two other possible sources of discrepancy between *Ginga* and *ASCA* data of these three sources were investigated, namely variability of either (i) the spectral slope of the intrinsic continuum (Model 3c; Table 4.7) or (ii) the soft X-ray flux (Model 3d; Table 4.8). In Model 3c the energy index of the hard power-law between *Ginga* and *ASCA* is untied, while the slope of the soft power-law is tied to that of the hard power-law derived by *Ginga*.¹ While both models give a better fit to the data than Model 3a, Model 3b still gives the best-fit for the Mrk 348 and NGC 7172 data. Hence it seems that the best explanation for the low-energy

¹The assumption made here is that any change in the spectral shape of the intrinsic continuum is not observed in the soft power-law component over the observational time-scales of several years.

disparity between *Ginga* and *ASCA* observations of Mrk 348 and NGC 7172 is column density variability. This rather simple modelling of the NGC 4507 data, however, does seem to prefer a change in spectral slope (Model 3c) rather than in column density (Model 3b), although the difference is marginal. According to Model 3c the inferred energy index of the hard continuum for NGC 4507, during the *Ginga* epoch, is $\alpha \sim 0.3$, such an intrinsically hard continuum would be very difficult to explain with current unification models. One interesting point to note is that the deviation between the *Ginga* and *ASCA* residuals for NGC 4507 (see Figure 4.2) is a slow function of energy in comparison with those of Mrk 348 and NGC 7172. Hence an alternative possibility is that the column change is more complex. For example there could be more than one absorbing component, such as is observed in the X-ray spectrum of NGC 4151 (see § 4.3). Complex absorption could also account for the flat spectral index obtained from the *Ginga* data. A fraction of the continuum source attenuated by a column $N_H \gtrsim 10^{24} \text{ cm}^{-2}$ would have the effect of making the observed *Ginga* continuum appear hard but have no significant effect on the *ASCA* continuum. The view taken, therefore, is that the analysis presented here provides evidence for column density variability in NGC 4507, although this interpretation is ambiguous.

Fe K_α emission and Compton reflection

The measured iron-line energy in all of five of the Seyfert 2 galaxies, when corrected for redshift, is consistent with $E_{K\alpha} \approx 6.4 \text{ keV}$ (unless otherwise stated we use the results of Model 3b for Mrk 348, NGC 7172 and NGC 4507, and Model 3a for ESO 103-G35 and IC 5063), implying neutral/lightly ionized iron (Fe I-XVI). The range of observed iron EW is between ~ 35 -220 eV (see figure 4.3), which is, for the column densities observed in each object, consistent with a spherical distribution of gas that surrounds the continuum source as a possible origin for the iron emission (Leahy & Creighton 1993). As can be seen from the large error bars in figure 4.3 the Fe-K EW are only loosely constrained. However, one interesting result is that the EW in both Mrk 348 and ESO 103-G35 is consistent with being constant (EW $\sim 126 \text{ eV}$ and 171 eV respectively) between observations even though the intrinsic flux varies. This implies that the Fe emission in these two objects is produced in a region which lies relatively close to the X-ray source at a distance $d \lesssim 2.5$ and $\lesssim 0.3 \text{ pc}$ for Mrk 348 and ESO 103-G35 respectively. A possible origin for the Fe K_α emission is an accretion disk in which the line flux might be expected to vary in accordance with the hard X-ray flux on time-scales of much shorter than a year. The profile

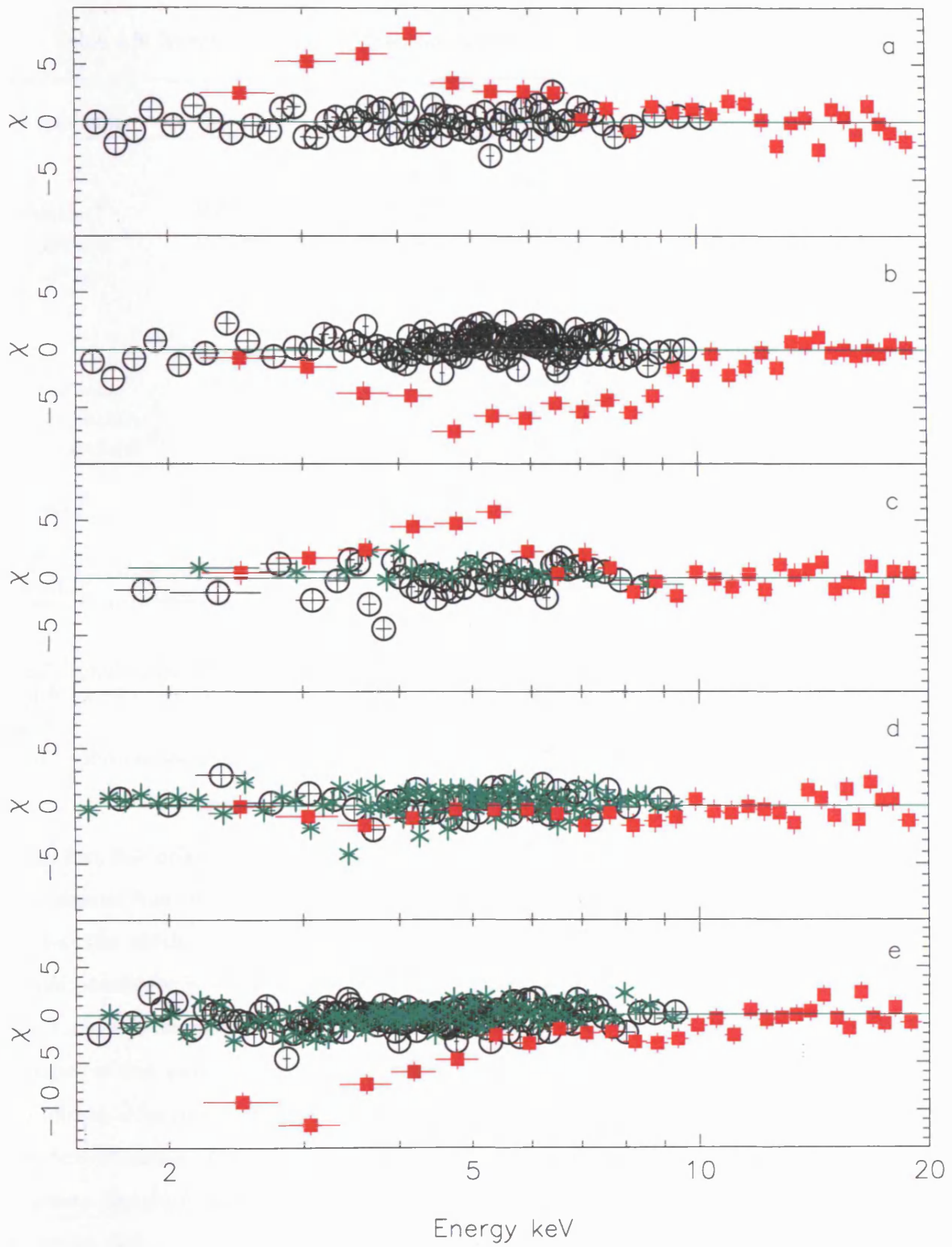


Figure 4.2: The spectral fitting residuals to the composite *Ginga* /*ASCA* spectrum for a) Mrk 348, b) NGC 4507, c) ESO 103-G35, d) IC 5063 and e) NGC 7172 using Model 3a but with the column density fixed at the best-fit value obtained by *ASCA* data alone. The data points correspond to *Ginga* top-layer (red squares), *ASCA* (1) SIS-0 (black circles) and *ASCA* (2) SIS-0 (green stars). Note the large discrepancy between the *Ginga* and *ASCA* data for Mrk 348, NGC 4507 and NGC 7172.

Table 4.5: Spectral fitting of the composite *Ginga* and *ASCA* spectra: Model 3a

Parameter	Mrk 348	NGC 4507	ESO 103-G35	IC 5063	NGC 7172
α	$0.85^{+0.07}_{-0.09}$	$0.27^{+0.07}_{-0.05}$	0.85 ± 0.07	0.47 ± 0.1	0.75 ± 0.02
A_{Ginga}^a	0.84 ± 0.17	$0.59^{+0.02}_{-0.01}$	$1.47^{+0.27}_{-0.22}$	$0.36^{+0.10}_{-0.08}$	$1.85^{+0.10}_{-0.09}$
$A_{ASCA(1)}^a$	0.27 ± 0.05	$0.74^{+0.13}_{-0.11}$	$1.15^{+0.21}_{-0.17}$	$0.48^{+0.12}_{-0.09}$	1.95 ± 0.10
$A_{ASCA(2)}^a$	-	-	$1.57^{+0.29}_{-0.24}$	$0.58^{+0.14}_{-0.11}$	0.55 ± 0.03
N_H^b	$15.3^{+0.9}_{-1.1}$	$32.8^{+1.4}_{-0.7}$	$21.3^{+1.2}_{-1.1}$	$21.7^{+1.3}_{-1.2}$	9.4 ± 0.2
$E_{K\alpha}^c$	6.28 ± 0.06	6.31 ± 0.03	$6.33^{+0.06}_{-0.09}$	6.30 ± 0.06	6.35 ± 0.06
$A_{K\alpha Ginga}^d$	$0.9^{+2.1}_{-0.9}$	11.7 ± 2.5	7.8 ± 1.6	5.3 ± 2.0	$4.8^{+1.8}_{-1.7}$
$A_{K\alpha ASCA(1)}^d$	1.7 ± 0.5	7.4 ± 1.3	$4.7^{+2.0}_{-1.9}$	3.2 ± 1.8	4.7 ± 2.5
$A_{K\alpha ASCA(2)}^d$	-	-	$9.2^{+4.1}_{-4.3}$	2.7 ± 1.1	3.0 ± 1.0
A_{soft}^a	$0.0044^{+0.0013}_{-0.0014}$	0.012 ± 0.001	$0.0050^{+0.0027}_{-0.0026}$	0.0076 ± 0.0014	$0.0052^{+0.0021}_{-0.0018}$
χ^2	387.9	540.1	316.0	621.1	1199.2
d.o.f.	354	472	314	594	1133

^a 10^{-2} photon $\text{cm}^{-2} \text{s}^{-1} \text{keV}^{-1}$.

^b 10^{22}cm^{-2} .

^c keV.

^d 10^{-5} photon $\text{cm}^{-2} \text{s}^{-1}$.

of an iron line originating from the inner regions of accretion disk is expected to be broadened and skewed from doppler, gravitational and Compton scattering effects. For all of the above models the width of the Fe $K\alpha$ line was fixed at $\sigma_{K\alpha} = 0.05$ keV. The results of making $\sigma_{K\alpha}$ a free parameter is shown in Table 4.9. The iron line energy is fixed at the previous best-fit value and it is assumed that the width of the iron line does not vary between observations. The number of free parameters, therefore, does not change. Allowing $\sigma_{K\alpha}$ to vary freely makes a significant difference for only one object out of five, interestingly this object is ESO 103-G35, the best-fit sigma being $\sigma_{K\alpha} \sim 0.35$. The constant Fe $K\alpha$ EW plus the preference for a broad gaussian therefore supports the view that the iron emission in ESO 103-G35 comes from the accretion disk.

From the results of Tables 4.5 and 4.6 the derived slopes for NGC 4507 and IC 5063 of $\alpha \sim 0.45$ and $\alpha \sim 0.47$ respectively are harder than the canonical value observed for Seyfert 1 galaxies

Table 4.6: Spectral fitting of the composite *Ginga* and *ASCA* spectra: Model 3b

Parameter	Mrk 348	NGC 4507	ESO 103-G35	IC 5063	NGC 7172
α	$0.67^{+0.07}_{-0.11}$	$0.45^{+0.06}_{-0.07}$	0.84 ± 0.08	$0.57^{+0.13}_{-0.12}$	0.80 ± 0.03
A_{Ginga}^a	$0.52^{+0.09}_{-0.12}$	$0.97^{+0.31}_{-0.23}$	$1.44^{+0.31}_{-0.25}$	$0.47^{+0.19}_{-0.13}$	$2.12^{+0.14}_{-0.13}$
$A_{ASCA(1)}^a$	0.21 ± 0.04	$1.02^{+0.26}_{-0.20}$	$1.20^{+0.23}_{-0.19}$	$0.60^{+0.18}_{-0.14}$	2.04 ± 0.11
$A_{ASCA(2)}^a$	-	-	$1.38^{+0.28}_{-0.23}$	$0.69^{+0.21}_{-0.15}$	0.62 ± 0.04
$N_H^{Ginga}^b$	$11.1^{+1.2}_{-1.7}$	$42.0^{+3.4}_{-3.2}$	$21.1^{+1.5}_{-1.4}$	$25.7^{+3.6}_{-3.4}$	10.3 ± 0.4
$N_H^{ASCA(1)}^b$	$16.3^{+1.1}_{-1.3}$	$33.4^{+1.5}_{-1.4}$	$22.5^{+1.5}_{-1.4}$	$23.1^{+2.2}_{-2.0}$	8.9 ± 0.2
$N_H^{ASCA(2)}^b$	-	-	$18.7^{+1.8}_{-1.6}$	$21.9^{+1.4}_{-1.3}$	9.8 ± 0.4
$E_{K\alpha}^c$	6.27 ± 0.07	6.31 ± 0.03	$6.32^{+0.06}_{-0.10}$	6.30 ± 0.06	6.37 ± 0.06
$A_{K\alpha Ginga}^d$	$3.1^{+2.2}_{-1.8}$	10.8 ± 2.4	7.9 ± 1.7	4.7 ± 2.1	2.7 ± 1.9
$A_{K\alpha ASCA(1)}^d$	1.3 ± 0.5	8.2 ± 1.5	$4.0^{+2.0}_{-2.1}$	3.0 ± 1.8	6.6 ± 2.5
$A_{K\alpha ASCA(2)}^d$	-	-	$10.9^{+4.3}_{-4.2}$	2.8 ± 1.1	2.9 ± 1.0
A_{soft}^a	$0.0044^{+0.0011}_{-0.0012}$	$0.0137^{+0.0017}_{-0.0015}$	$0.0052^{+0.0027}_{-0.0026}$	$0.0083^{+0.0016}_{-0.0015}$	$0.0052^{+0.0022}_{-0.0021}$
χ^2	354.9	523.1	306.8	615.5	1154.9
d.o.f.	353	471	312	592	1131
$\Delta\chi^2$	33.0	17.0	9.2	5.6	44.3

^a 10^{-2} photon $\text{cm}^{-2} \text{s}^{-1} \text{keV}^{-1}$.

^b 10^{22}cm^{-2} .

^c keV.

^d 10^{-5} photon $\text{cm}^{-2} \text{s}^{-1}$.

(Nandra & Pounds 1994; Reynolds 1997; George *et al.* 1998). One possible explanation for this hardness is the presence of a Compton reflection component which flattens an otherwise steep spectrum. The contribution from reflection turns over at ~ 30 keV giving the characteristic Compton reflection ‘hump’. The use of *Ginga* data is, therefore, essential in order to obtain any kind of constraint on the amount of possible reflection present. To represent Compton reflection the XSPEC model ‘pexrav’ (Magdziarz & Zdziarski 1995) is used as an additional component to either Model 3a or 3b for each object. As is the case for the hard power-law continuum, the reflection component is also assumed to be absorbed by the cold gas of column density N_H . The inclination angle of the disk is fixed at $i = 60^\circ$ and the strength of the reflection component, relative to the hard power-law, is assumed to be invariable. The best-fitting values for the energy index, the preferred amount of reflection and the corresponding decrease in χ^2 is

Table 4.7: Spectral fitting of the composite *Ginga* and *ASCA* spectra: Model 3c

Parameter	Mrk 348	NGC 4507	NGC 7172
α_{Ginga}	$0.78^{+0.09}_{-0.07}$	$0.28^{+0.07}_{-0.06}$	0.76 ± 0.03
$\alpha_{ASCA(1)}$	$0.33^{+0.16}_{-0.12}$	$0.69^{+0.13}_{-0.11}$	$0.91^{+0.08}_{-0.07}$
$\alpha_{ASCA(2)}$	-	-	$0.73^{+0.08}_{-0.09}$
A_{Ginga}^a	$0.69^{+0.14}_{-0.12}$	$0.62^{+0.13}_{-0.10}$	$1.91^{+0.13}_{-0.11}$
$A_{ASCA(1)}^a$	$0.11^{+0.04}_{-0.03}$	$1.71^{+0.67}_{-0.48}$	$2.50^{+0.36}_{-0.28}$
$A_{ASCA(2)}^a$	-	-	0.54 ± 0.08
N_H^b	$13.0^{+1.4}_{-1.3}$	$36.5^{+1.8}_{-1.7}$	9.7 ± 0.3
$E_{K\alpha}^c$	6.27 ± 0.07	6.31 ± 0.03	6.37 ± 0.6
$A_{K\alpha Ginga}^d$	$1.8^{+2.2}_{-1.7}$	12.7 ± 2.4	$4.2^{+1.8}_{-1.9}$
$A_{K\alpha ASCA(1)}^d$	1.4 ± 0.5	7.7 ± 1.5	6.5 ± 2.6
$A_{K\alpha ASCA(2)}^d$	-	-	$2.7^{+1.0}_{-1.1}$
A_{soft}^a	$0.0039^{+0.0015}_{-0.0011}$	$0.0122^{+0.0013}_{-0.0012}$	$0.0067^{+0.0015}_{-0.0029}$
χ^2	367.1	514.2	1182.3
d.o.f.	353	471	1131
$\Delta\chi^2$	20.8	25.9	16.9

^a 10^{-2} photon $\text{cm}^{-2} \text{s}^{-1} \text{keV}^{-1}$.

^b 10^{22}cm^{-2} .

^c keV.

^d 10^{-5} photon $\text{cm}^{-2} \text{s}^{-1}$.

listed in Table 4.10. The NGC 4507 data prefers a significant amount of reflection ($R \sim 0.74$) although this value is rather unconstrained. Recent broad-band (0.1-100 keV) observations of NGC 4507 with BeppoSAX (Bassani *et al.* 1998) also shows some evidence for reflection ($R = 0.4 \pm 0.2$). The BeppoSAX results however, although only preliminary, require a relatively steep hard continuum of energy index $\alpha \sim 1.0$ and a column density of $\sim 7.0 \times 10^{23} \text{cm}^{-2}$, about twice that measured by *Ginga* /*ASCA* implying a huge change in column.

Table 4.8: Spectral fitting of the composite *Ginga* and *ASCA* spectra: Model 3d

Parameter	Mrk 348	NGC 4507	NGC 7172
α	0.80 ± 0.08	0.26 ± 0.07	0.76 ± 0.03
A_{Ginga}^a	$0.71^{+0.19}_{-0.14}$	$0.57^{+0.08}_{-0.09}$	$1.89^{+0.02}_{-0.05}$
$A_{ASCA(1)}^a$	$0.27^{+0.06}_{-0.04}$	$0.71^{+0.10}_{-0.09}$	$1.97^{+0.06}_{-0.10}$
$A_{ASCA(2)}^a$	-	-	0.56 ± 0.03
N_H^b	16.4 ± 1.2	$32.5^{+1.3}_{-1.4}$	$9.5^{+0.1}_{-0.2}$
$E_{K\alpha}^c$	6.28 ± 0.07	6.31 ± 0.03	6.36 ± 0.06
$A_{K\alpha Ginga}^d$	1.9 ± 1.9	$11.7^{+1.3}_{-2.0}$	$4.8^{+1.7}_{-1.8}$
$A_{K\alpha ASCA(1)}^d$	1.4 ± 0.5	8.3 ± 1.4	4.8 ± 2.4
$A_{K\alpha ASCA(2)}^d$	-	-	3.0 ± 1.0
$A_{soft\ Ginga}^a$	$0.051^{+0.016}_{-0.015}$	$0.0^{+0.025}_{-0.0}$	$0.0^{+0.003}_{-0.0}$
$A_{soft\ ASCA(1)}^a$	0.0047 ± 0.0013	0.012 ± 0.001	0.010 ± 0.001
$A_{soft\ ASCA(2)}^a$	-	-	0.005 ± 0.002
χ^2	366.3	539.1	1189.0
d.o.f.	353	471	1131
$\Delta\chi^2$	21.6	1.0	10.2

^a 10^{-2} photon $\text{cm}^{-2} \text{s}^{-1} \text{keV}^{-1}$.

^b 10^{22}cm^{-2} .

^c keV.

^d 10^{-5} photon $\text{cm}^{-2} \text{s}^{-1}$.

Table 4.9: The width of the Fe K_{α} emission line

Parameter	Mrk 348	NGC 4507	ESO 103-G35	IC 5063	NGC 7172
$\sigma_{K\alpha}$ (keV)	$0.005^{+0.197}_{-0.005}$	0.09 ± 0.05	$0.35^{+0.15}_{-0.14}$	$0.04^{+0.26}_{-0.04}$	$0.50^{+0.43}_{-0.27}$
χ^2	354.3	522.8	306.2	621.1	1152.0
$\Delta\chi^2$	0.2	0.3	9.8	0.0	2.9

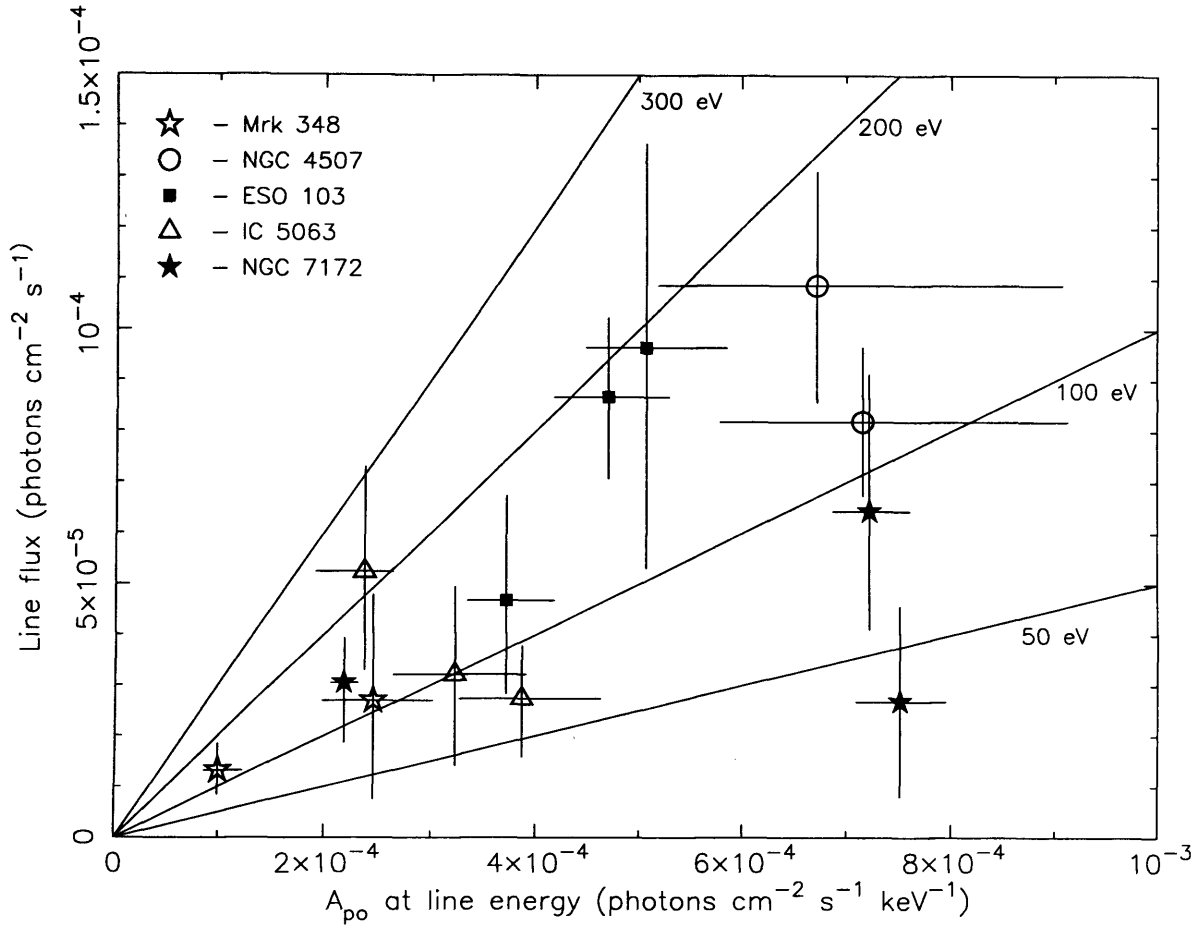


Figure 4.3: The strength of the Fe- K_{α} line versus the continuum level at the line energy. The solid straight lines are lines of constant EW.

Table 4.10: Spectral fitting of the composite *Ginga* and *ASCA* spectra: Compton reflection

Parameter	Mrk 348	NGC 4507	ESO 103-G35	IC 5063	NGC 7172
α	$0.64^{+0.15}_{-0.09}$	0.62 ± 0.15	$1.13^{+0.18}_{-0.15}$	$0.72^{+0.21}_{-0.19}$	$0.90^{+0.06}_{-0.07}$
R	$0.0^{+0.74}_{-0.0}$	$0.74^{+0.59}_{-0.50}$	$1.8^{+1.5}_{-1.0}$	$1.6^{+1.9}_{-1.1}$	$0.52^{+0.35}_{-0.27}$
χ^2	354.8	516.0	302.3	613.5	1145.1
d.o.f.	352	470	313	593	1130
$\Delta\chi^2$	0.1	7.1	13.7	7.6	9.8

4.2.4 Discussion

Thus far, reports of column density variability in type 2 AGN have been scarce. Strong evidence has been found for N_H variability in three out of the five objects in the sample of heavily obscured Seyfert 2 galaxies, increasing two fold the number of known Seyfert 2s with variable N_H . This change in column can be attributed to either geometric effects such as high column density gas clouds intersecting the line-of-sight to the central source or photoionization of the obscuring gas which reduces its opacity at low energies.

If the observed absorption is due to a cloud of gas that is assumed to be moving in a keplerian orbit around a black hole of mass M_8 at a distance r_{16} (where M_8 and r_{16} are in units of 10^8 solar masses and 10^{16} cm respectively) then the transverse velocity of the cloud is given by

$$v \approx 10^4 \sqrt{\frac{M_8}{r_{16}}} \text{ km s}^{-1} \quad (4.1)$$

The ionization state of the gas is described by the ionization parameter

$$\xi = \frac{L_{42}}{n_{10} r_{16}^2} \quad (4.2)$$

where L_{42} is the source luminosity between 0.0136 -13.6 keV in units of 10^{42} erg s^{-1} and n_{10} is its density in 10^{10} cm^{-3} . A simple sketch of how the measured column density N_H varies when a spherical cloud, of size D_{cloud} , moves in and out of the line-of-sight to the central X-ray source of size D_{src} (where $D_{src} \ll D_{cloud}$) is given in Figure 4.4. For a spherical cloud the time-scale for the column density change, T_{N_H} , is roughly the cloud radius divided by its transverse velocity.

$$T_{N_H} \approx \frac{D_{cloud}}{2v} \approx 5 \times 10^{11} \frac{\Delta N_{22}}{n_{10} v} \text{ s} \quad (4.3)$$

where ΔN_{22} is the change in column density in units of 10^{22} cm^{-2} . Substituting for v and r_{16} above using equations 4.1 and 4.2 and rearranging to get density as the term on the left hand side gives

Table 4.11: Estimates on the density, size and distance of an obscuring cloud moving into and out of the line-of-sight to the central X-ray source.

	Mrk 348	NGC 4507	NGC 7172
n_{10}	9×10^{-3}	3×10^{-2}	4×10^{-3}
r_{16}	76	51	115
$D_{cloud}(10^{16} \text{ cm})$	6×10^{-2}	3×10^{-2}	3×10^{-2}

$$n_{10} \approx 5.7 \times 10^3 \frac{\Delta N_{22}^{4/5} L_{42}^{1/5}}{T_{N_H}^{4/5} M_8^{2/5} \xi^{1/5}} \quad (4.4)$$

Similarly for the distance of the cloud from the source

$$r_{16} \approx 1.3 \times 10^{-2} \frac{T_{N_H}^{2/5} M_8^{1/5} L_{42}^{2/5}}{\Delta N_{22}^{2/5} \xi^{2/5}} \quad (4.5)$$

Assuming that the mass of the black hole is 10^8 solar masses and that the column density time-scale is equivalent to the time taken between observations (i.e. the sources were observed at points 1 and 2 on the curve in Figure 4.4) values for the density and size of the cloud plus its distance from the X-ray source can be estimated for the three sources that show evidence of column variability (Table 4.11). Since the gas is cold a value of $\xi = 1$ is assumed for the ionization parameter. The results of Table 4.11 are consistent with the conjecture that the obscuration is due to several high density, cold clouds of gas situated at a distance from the central source which is compatible with a molecular torus. It should be noted, however, that the time-scale for the column density variation could be much smaller, or even larger, than the one assumed. What is required is frequent observations of these objects (e.g. every month) over a period of several years so that the form of the N_H variation is well sampled.

Another possibility is that the size of the X-ray source, D_{src} , is comparable to the thickness of the clouds which are thin and sheet-like. In this scenario the edge of the cloud travels across the face of the source with the degree of obscuration gradually increasing until the source is completely covered. Hence in this case the time-scale for the column change is the time it takes

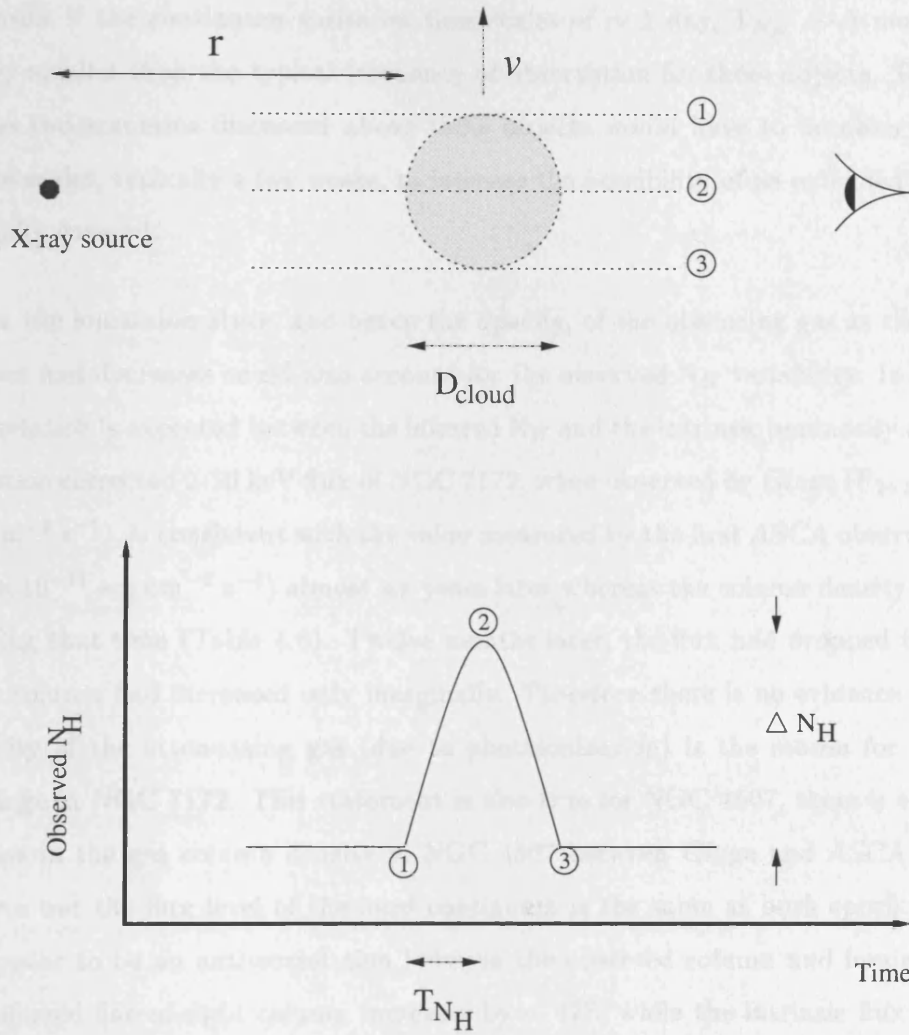


Figure 4.4: Column density variability for a cloud of gas moving across the line-of-sight to the central X-ray source.

the cloud to travel a distance D_{src} .

$$T_{N_H} = \frac{D_{src}}{v} \approx 10^{-4} D_s \sqrt{\frac{r_{16}}{M_8}} \text{ s} \quad (4.6)$$

The size of the X-ray source can be estimated from $D_{src} = c t_s$, where t_s is the continuum variability time-scale and c is the speed of light, to give

$$T_{N_H} \approx 30 t_s \sqrt{\frac{r_{16}}{M_8}} \text{ s} \quad (4.7)$$

So for example if the continuum varies on time-scales of ~ 1 day, $T_{N_H} \sim 1$ month which is considerably smaller than the typical frequency of observation for these objects. To distinguish between the two scenarios discussed above these objects would have to be observed on much shorter time-scales, typically a few weeks, to increase the possibility of an extended X-ray source being partially covered.

A change in the ionization state, and hence the opacity, of the obscuring gas as the hard X-ray flux increases and decreases could also account for the observed N_H variability. In this scenario an anti-correlation is expected between the inferred N_H and the intrinsic luminosity of the source. The absorption corrected 2-10 keV flux of NGC 7172, when observed by *Ginga* ($F_{2-10} = 7.4^{+0.5}_{-0.4} \times 10^{-11}$ erg cm $^{-2}$ s $^{-1}$), is consistent with the value measured by the first *ASCA* observation ($F_{2-10} = 7.1 \pm 0.4 \times 10^{-11}$ erg cm $^{-2}$ s $^{-1}$) almost six years later whereas the column density decreases by $\sim 16\%$ during that time (Table 4.6). Twelve months later, the flux had dropped by a factor ~ 5 while the column had increased only marginally. Therefore there is no evidence that changes in the opacity of the attenuating gas (due to photoionization) is the reason for the observed column change in NGC 7172. This statement is also true for NGC 4507, there is evidence for a 20% decrease in the gas column density in NGC 4507 between *Ginga* and *ASCA* observations of this source but the flux level of the hard continuum is the same at both epoch. There does, however, appear to be an anti-correlation between the observed column and luminosity of Mrk 348. The inferred line-of-sight column increases by $\sim 47\%$ while the intrinsic flux decreases by a factor of almost 2.5 between *Ginga* and *ASCA* observations of this object.

An important consideration is whether the observed increase/decrease in luminosity is large enough to produce the change in column. The photoionization code XSTAR (Kallman & Krolik 1997) has been used to model the observed spectra if the intrinsic continuum were absorbed by a cloud of gas with a range of ionization parameters ($-3 < \log \xi < 3.0$). The cloud, which is assumed to have a density of $n=10^6$ cm $^{-3}$, is photoionized by a source spectrum consisting of a broken power-law with an energy index of $\alpha = 0.7$ below 100 keV and $\alpha = 2.0$ above 100 keV. Each model, which represents a particular ξ and N_H , is then folded through the SIS-0 response curve to produce artificial PHA files. Each ‘faked’ PHA file is then fitted with a power-law model which is attenuated by a cold column of gas, hence for a particular value of ξ and N_H a representative column density of cold gas is obtained. Plots of the measured column density, N_{Hcold} against the ionization parameter, ξ , are shown in figure 4.5 for a true column density of

$2.0 \times 10^{23} \text{ cm}^{-2}$. Using the steepest part of the curve to obtain a change in observed column of $\sim 5 \times 10^{22} \text{ cm}^{-2}$, which is the column change in Mrk 348, requires a change in ξ of ~ 30 . From the definition of the ionization parameter $\xi = \frac{L}{nR^2}$ and assuming that the density and distance of the cloud from the photoionizing source remains constant, then the ratio $\frac{\Delta\xi}{\xi} = \frac{\Delta L}{L}$. From the curve in figure 4.5 a value of $\frac{\Delta\xi}{\xi} = \frac{30}{70} \sim 0.4$ is obtained. For Mrk 348 $\frac{\Delta L}{L} \sim \frac{1.3 \times 10^{-11}}{2.2 \times 10^{-11}} \sim 0.6$. Therefore, to a first order approximation, the inferred variation in luminosity is large enough to change the measured column density of the absorbing gas. At first this might seem rather contrived since, as can be seen from figure 4.5, for a change in the measured column density to be observed the ionization parameter of the absorbing gas must be within a narrow range of values. This, however, is not the case since all that is required is for a fraction of the material in the line-of-sight to the central source to be within the optimal range of ionization parameter. In the case of Mrk 348, the measured column density could possibly be due to several clouds of gas, with the cloud situated closest to the central source being at the required ionization state and hence very sensitive to any change in continuum flux. Another consideration is that although the gas is in an ionization state that makes it sensitive to a change in the luminosity of the central source, on what kind of time-scale does it respond to this change? Since absorption of the intrinsic flux by oxygen atoms is a major contributor to the characteristic cut-off observed at soft X-ray energies it seems reasonable to assume that the recombination time-scale of oxygen atoms will provide an adequate description of how the whole gas might respond to variation in the luminosity. From the results of modelling with XSTAR and assuming that the gas has an ionization parameter of $\log \xi \sim 2.0$, the most abundant oxygen ion in such a gas is O III. For such a gas in thermal equilibrium the recombination rate coefficient for this ion is $\sim 1.4 \times 10^{-11} \text{ cm}^3 \text{ s}^{-1}$. The recombination time-scale is defined as $T_{rec} = (n\alpha_B)^{-1}$ (Osterbrock 1989) where α_B is the case B recombination rate coefficient. For O III, $T_{rec} \sim 7 \times 10^4 n_6^{-1} \text{ s} \sim 1 \text{ day}$, the time between the *Ginga* and *ASCA* observations of Mrk 348 was ≈ 8 years, hence on these time-scales the gas would be expected to respond almost instantaneously to any change in the luminosity of the central source.

With the current data it is hard to distinguish whether the column variation in Mrk 348 is due to either cold clouds moving out of the the line-of-sight or a change in the cloud's opacity because of photoionization. Monitored observations of Mrk 348 with good signal-to-noise are required to obtain further constraints on the source of column density variation occurring in this

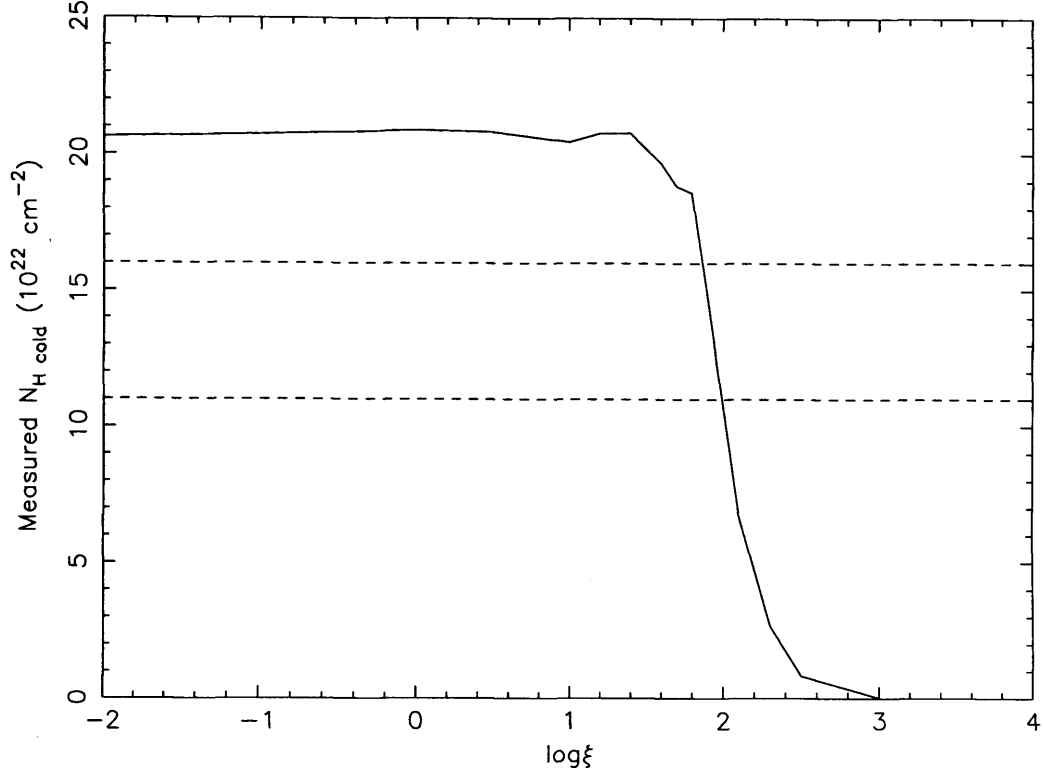


Figure 4.5: The measured cold column density of a gas with differing ionization parameters. The actual column density of the gas is $2 \times 10^{23} \text{ cm}^{-2}$. The horizontal dotted lines represent the line-of-sight column measured in Mrk 348 by *Ginga* and *ASCA* (see Table 4.6).

object. BeppoSax observations of Seyfert 2 galaxies such as those discussed here could provide, in principle, useful information on these objects. BeppoSax's broadband data would provide tighter constraints on the slope of the intrinsic continuum and hence bring less ambiguity to the measurement and variability of the column density in these sources. However, BeppoSax observation of only a few of the brightest Seyfert 2 galaxies have been published thus far (e.g. Cappi *et al.* 1999b; Bassani *et al.* 1998).

4.3 The complex absorption in NGC 4151

The Seyfert galaxy NGC 4151 is one of the most extensively observed sources in the X-ray band (e.g. Pounds *et al.* 1986; Yaqoob, Warwick & Pounds 1989; Fiore, Perola & Romano 1990; Yaqoob *et al.* 1993; Warwick, Done & Smith 1995; Weaver *et al.* 1994b). The hard X-ray spectrum of NGC 4151 is characterized by an intrinsic power-law continuum which varies both

in amplitude and spectral index, with the latter apparently correlated with the luminosity of the source in the 2-10 keV band (Yaqoob & Warwick 1991; Yaqoob *et al.* 1993). In addition, the hard continuum is attenuated in the 1-5 keV range by heavy, complex and variable absorption. A strong iron K_{α} emission line consistent with reprocessing by cold/slightly ionized gas is also observed. The soft X-ray spectrum (< 1 keV) is thought to be distinct from the hard X-ray spectrum. There is little evidence for variability of the soft excess (Weaver *et al.* 1994a; Warwick, Done & Smith 1995; Warwick *et al.* 1996), Weaver *et al.* (1994b) reported an increase of 50% in the count rate below 0.8 keV between two ASCA observations, however it is unclear whether this can be attributed to uncertainties in the calibration of the SIS instruments below 0.8 keV. This section primarily investigates the complex absorption in the 1-5 keV band of NGC 4151 using four ASCA observations, including one with a long (~ 100 ks) exposure, taken over a period of about two years.

4.3.1 Data Analysis

The BL Lac object 1E1207-9+3945 is situated about 5 arcmin north of NGC 4151, therefore because of possible contamination of the GIS spectra only SIS-0 data is used in this analysis (SIS-0 being the best calibrated out of the two SIS instruments). In the preliminary analysis the model used to describe the complex absorption present in the X-ray spectrum of NGC 4151 is the dual absorber model used by Weaver *et al.* (1994b). This model represents non-uniform absorption along the line-of-sight to the central X-ray source and consists of a column density N_{H1} of gas which covers a fraction C_{f1} of the hard power-law continuum source and a second column N_{H2} which covers a fraction C_{f2} , where $C_{f2} = 1 - C_{f1}$. In addition to the dual absorber model a gaussian line with energy $E_{K\alpha}$, width $\sigma_{K\alpha}$, and intensity $A_{K\alpha}$ is required to model iron $K\alpha$ line emission. Again, as was the case in Weaver *et al.* (1994b), the iron $K\alpha$ line is not considered in detail and its width $\sigma_{K\alpha}$ is fixed at the upper limit obtained from BBXRT data of 160 eV (Weaver *et al.* 1992) for all datasets. This value also happens to be the preferred width to the AO4 data when $\sigma_{K\alpha}$ is allowed to be free. An in-depth analysis of the iron line profile was conducted by Yaqoob *et al.* (1995) using ASCA observations performed during PV1, PV2 and AO1.

Although the complex absorption is the focus of this section, all of the results are obtained from

fits to the whole 0.7 - 10 keV band. For the purpose of this analysis a soft power-law, with the energy index tied to that of the hard continuum, and a Gaussian emission line at an energy ~ 0.9 keV, both of which are absorbed by the Galactic column of $N_{Gal} = 2.0 \times 10^{20} \text{ cm}^{-2}$, provide an adequate, although somewhat arbitrary, description of the soft X-ray spectrum of NGC 4151. A more detailed analysis of the soft X-ray spectrum is presented in § 5.3. The limited bandpass and the heavy absorption present in NGC 4151 means that the slope of the intrinsic power-law continuum is poorly constrained by *ASCA*. Several *Ginga* observations of NGC 4151 found α to lie in the range 0.4-0.7 (Yaqoob *et al.* 1993). Also, long-term monitoring of NGC 4151 by OSSE suggest that the hard X-ray spectrum is well described by a power-law with energy index $\alpha = 0.6^{+0.2}_{-0.3}$ (Warwick *et al.* 1996; Johnson *et al.* 1997). Therefore when fitting the *ASCA* data with the model described above α is fixed at a value of 0.6. The best-fit parameters for all four observations are given in Table 4.12.

The best-fitting version of the dual absorber model is plotted for each *ASCA* observation in Figure 4.6 and illustrates very well the change in the spectral shape of NGC 4151 between 1-5 keV. However, while the dual-absorber model gives a good fit to the PV1, PV2 and AO1 data the “wavy” residuals of this model to the superior signal-to-noise spectrum obtained during AO4 implies an incomplete description of the absorption. An improvement in χ^2 of 14.5 is obtained when a third absorbing medium with a covering fraction C_{f3} (such that $C_{f1} + C_{f2} + C_{f3} = 1$) is added and fit to the AO4 data (see Table 4.12, Model AO4(b)). As an alternative to the dual absorber model, Weaver *et al.* (1994b) also considered a model consisting of a hard power-law continuum attenuated by an ionized absorber plus a scattered component. In this scenario the soft flux is expected to be correlated with the intrinsic continuum as the absorbing medium becomes more/less ionized with an increase/decrease in the hard X-ray flux. To investigate the nature of the 1-5 keV spectral variation exhibited by NGC 4151, plotted in Figure 4.7 are two softness ratios versus the continuum flux at 10 keV. The first (soft1) is the ratio of the flux at 2 keV to that at 10 keV and the second (soft2) is the ratio of the flux at 3.5 keV to that at 10 keV. If the data taken during PV2 is ignored then there does seem to be a correlation between both soft1 and soft2 and the hard continuum flux (i.e. the X-ray spectrum of NGC 4151 ‘softens’ with increasing intrinsic flux as expected). The inclusion of the PV2 data, however, contradicts this trend, in the one month between the PV2 and AO1 observations the flux at 10 keV increased by 30 percent but the softness ratios decrease significantly. Therefore a simple model, in which

Table 4.12: The best-fit parameters of the hard X-ray spectrum of NGC4151 using multi-absorber models

Parameter	PV1	PV2	AO1	AO4(a)	AO4(b)
α	0.6	0.6	0.6	0.6	0.6
A_{total}^a	$4.3^{+0.4}_{-0.5}$	$5.1^{+0.8}_{-0.7}$	7.1 ± 0.8	5.8 ± 0.2	$6.0^{+2.3}_{-2.5}$
N_{H1}^b	$18.1^{+4.1}_{-2.7}$	$10.5^{+3.4}_{-2.3}$	$11.5^{+1.8}_{-1.4}$	$17.6^{+1.2}_{-1.1}$	27^{+11}_{-6}
C_{f1}	0.81	0.43	0.59	0.66	0.39
N_{H2}^b	$4.3^{+1.3}_{-1.1}$	2.3 ± 0.2	3.4 ± 0.3	4.1 ± 0.2	$9.7^{+3.5}_{-3.6}$
C_{f2}	0.19	0.57	0.41	0.34	0.39
N_{H3}^b	-	-	-	-	$3.4^{+0.4}_{-0.8}$
C_{f3}	-	-	-	-	0.22
$E_{K\alpha}^c$	$6.46^{+0.06}_{-0.05}$	6.40 ± 0.04	6.37 ± 0.04	6.36 ± 0.02	6.36 ± 0.02
$\sigma_{K\alpha}^c$	0.16	0.16	0.16	0.16	0.16
$A_{K\alpha}^d$	56.4 ± 13.5	$57.9^{+10.5}_{-10.6}$	$47.4^{+8.1}_{-8.2}$	41.9 ± 4.3	40.0 ± 4.4
A_{soft}^a	0.12 ± 0.01	0.16 ± 0.02	0.15 ± 0.01	0.162 ± 0.004	0.158 ± 0.005
E_{ga}^c	0.90 ± 0.02	0.89 ± 0.02	0.90 ± 0.01	0.89 ± 0.01	0.89 ± 0.01
A_{ga}^d	$12.3^{+5.4}_{-5.3}$	12.6 ± 5.3	14.3 ± 3.5	10.0 ± 1.8	11.0 ± 1.9
χ^2	214.0	247.4	309.9	383.2	368.7
d.o.f.	203	251	279	315	313

^a 10^{-2} photon $\text{cm}^{-2} \text{s}^{-1} \text{keV}^{-1}$.

^b 10^{22}cm^{-2} .

^c keV.

^d 10^{-5} photon $\text{cm}^{-2} \text{s}^{-1}$.

the change in the spectral shape is attributed to a change in the ionization state of a warm absorber, cannot account for the spectral changes observed in the ASCA spectra of NGC 4151. Clearly, a more complex model is needed.

Next the possibility is considered that the ionization structure of the warm absorber is stratified. This is modelled in terms of three warm absorbers (along the line-of-sight) with fixed ionization parameters of $\xi = 10, 100$ and 1000 respectively. The column density of all 3 absorbers are free parameters hence physically, in a similar manner to the dual absorber, this model represents clouds of *warm* gas moving in and out of the line-of-sight. The attraction of this model is that it does not require partial covering of the X-ray source. The data from all four observations are fitted simultaneously. To keep the number of free parameters down to a minimum, the energy

Table 4.13: The best-fit parameters of the hard X-ray spectrum of NGC4151 using a warm absorber model.

ξ	10	100	1000
PV1	$5.5^{+2.2}_{-4.8}$	$0.0^{+12.2}_{-0.0}$	$28.2^{+6.1}_{-13.3}$
PV2	$3.1^{+0.2}_{-0.3}$	$0.0^{+0.6}_{-0.0}$	$7.1^{+0.9}_{-1.0}$
AO1	$3.9^{+0.8}_{-0.9}$	$1.0^{+1.5}_{-1.0}$	$11.8^{+1.2}_{-1.3}$
AO4	$3.6^{+0.8}_{-0.6}$	$1.0^{+1.0}_{-1.0}$	$20.5^{+1.0}_{-1.0}$

Note: The column density of the 3 absorbers (in units of 10^{22} cm^{-2}) are given only.

and width of the Fe K_{α} line are tied across the four datasets and fixed at 6.4 keV and 0.16 keV respectively. The energy, width and intensity of the soft X-ray gaussian line are also tied between observations with the energy and width fixed at 0.9 keV and 0.01 keV respectively. The free parameters in this model consist of (i) the normalisation of the hard power-law, (ii) the column densities of the three warm absorbers, (iii) the strength of both the Fe K_{α} and 0.9 keV lines and (iv) the normalisation of the soft power-law. This gives a total of 25 free parameters (for the four datasets). The best-fit parameters for the above model, albeit with a rather poor chi-squared of $\chi^2/\text{dof} = 1464.6/1059$, are listed in Table 4.13. For comparison, when the data are fitted simultaneously using the dual-absorber model, with the emission line parameters fixed and tied as discussed above, the best-fit parameters give $\chi^2/\text{dof} = 1176.2/1059$. The next step was to allow the ionization parameter values for the three components of the warm absorber to be free, but tied between observations (hence requiring only 3 additional free parameters). This model produced a huge improvement in the fit, giving $\chi^2/\text{dof} = 1282.3/1056$. Figure 4.8 shows how the column density of each warm absorber varies between observations. It was found that untying the ionization parameter of the absorbers and hence invoking a further 9 free parameters gave no significant improvement to the spectral fit.

4.3.2 Discussion

It is obvious from Figure 4.6 that the continuum absorption present in the X-ray spectrum of NGC 4151 is very complex. It shows that, in addition to the intrinsic continuum flux changing,

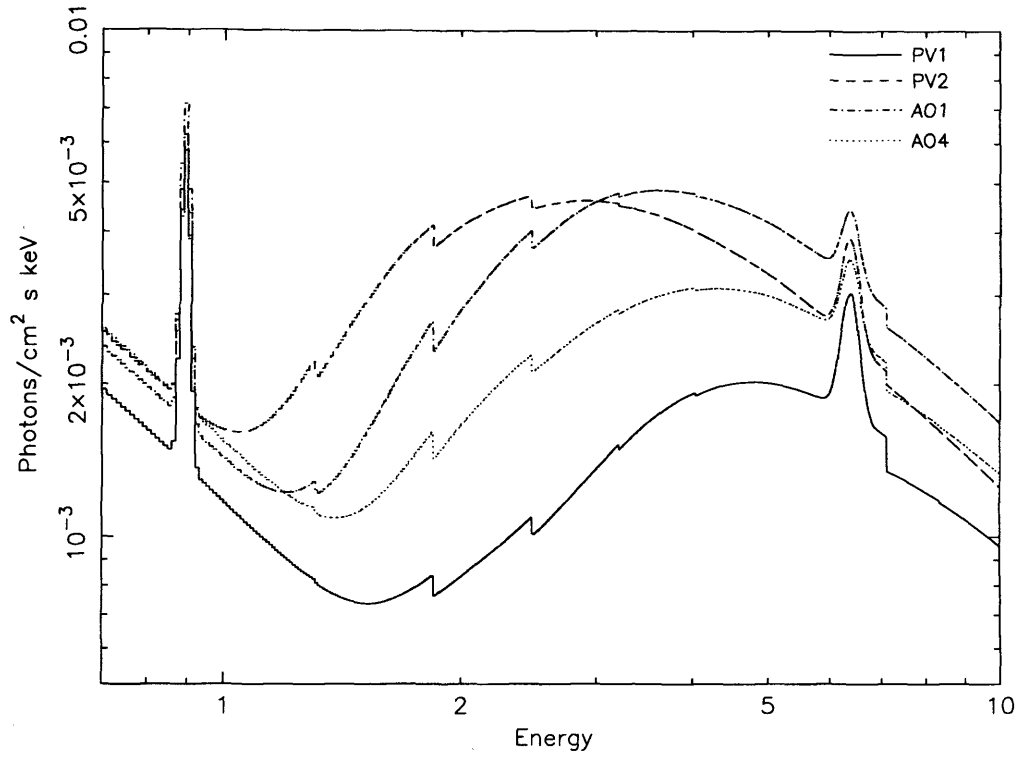


Figure 4.6: The best-fit dual-absorber model descriptions for all four ASCA spectra of NGC 4151.

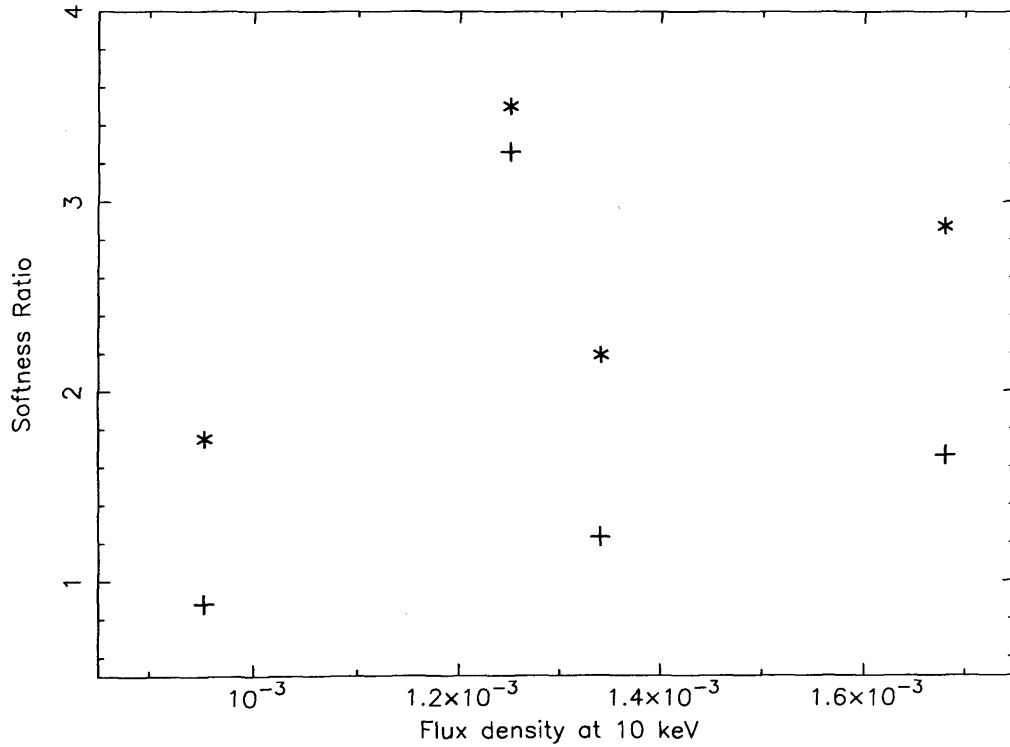


Figure 4.7: The softness ratios soft1 (crosses) and soft2 (stars) for NGC 4151 with respect to the hard continuum level. See text for definitions of ratios

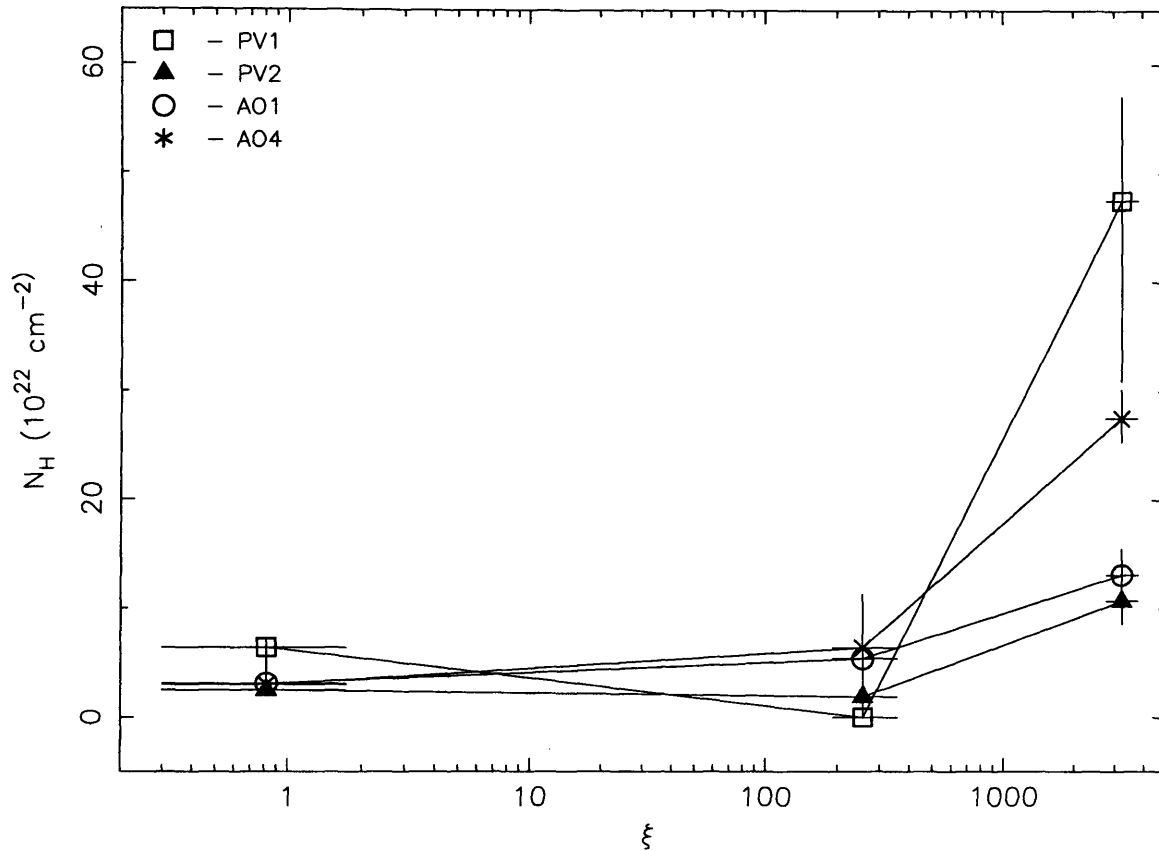


Figure 4.8: N_H variability in the stratified warm absorber model.

both the shape and flux of the 1-7 keV continuum vary with time in a complicated manner. It has been shown that a model in which the spectral variability is due to the changing opacity of a single partially ionized cloud can be ruled out. Here the X-ray spectrum of NGC 4151 has been described using two different interpretations. The first involved a model in which a fraction of the X-ray source is viewed through a line-of-sight of cold gas of column density N_{H1} while the rest is viewed through a column of N_{H2} and therefore requires that the size of the X-ray source is comparable to or greater than the absorbing clouds. This model is able to reproduce the observed spectra of NGC 4151 at different epochs fairly well. Fractional changes in column density of up to ≈ 50 percent in conjunction with large variations in the covering fraction were observed over periods as short as ~ 6 months. This implies that the X-ray source cannot be covered by a large number of smaller clouds and that the number of clouds in the line-of-sight is low. If the opposite were true the number of clouds observed at any given time would never differ greatly from a mean value and therefore a large change in the column density and covering fraction would not be expected (Reichert, Mushotzky & Holt 1986). This is also consistent with *Ginga* results

reported by Yaqoob *et al.* (1993) where the authors rejected variations in a random distribution of small clouds across the face of the X-ray source as an explanation for the apparent partial covering. Therefore, there can only be a small number of relatively large clouds responsible for the observed absorption in NGC 4151.

The alternative model considered was one in which the line-of-sight absorption is made up of several partially ionized clouds of differing ionization parameters. No more than 3 warm absorbers were required to represent the *ASCA* spectra of NGC 4151. The ionization parameters of the warm absorbers were tied across the four *ASCA* observations hence the spectral variability was accounted for by a change in the actual column density of the absorbers which can only be explained by clouds moving in and out of the line-of-sight. This model however, unlike the dual-absorber model discussed above, does not require partial covering of the X-ray source. A reasonable assumption concerning this model is that the more highly ionized gas is situated closer to the central X-ray source than the less ionized gas and therefore must have a greater transverse velocity. This in turn implies that a greater fractional variation in the column density of the highly ionized gas is expected as clouds move in and out of the line-of-sight at a greater rate. Figure 4.8 demonstrates that this does indeed seem to be the case. However, while this stratified warm absorber model has some advantages over the dual-absorber it should be noted that the dual-absorber model gives a significantly better fit, especially at higher energies. This could be due to the fact that the data cannot accommodate the high energy, smeared Fe-K edge predicted at ~ 8.4 keV by the warm absorber model. Indeed this edge energy is also inconsistent with the overall mean energy obtained from previous *Ginga* measurements of $E_{edge} = 7.34 \pm 0.02$ (Yaqoob *et al.* 1993). Also, as reported by Yaqoob *et al.* (1993), NGC 4151 was observed by *Ginga* during a very bright state in May 1990. The obvious softening of the spectrum in this observation was indicative of a marked decline in the soft X-ray absorption, but this was not accompanied by a similar decrease in the optical depth of the Fe-K edge. The upper limit on the edge energy was ~ 7.7 keV, which is significantly higher than the typical value for NGC 4151 although still lower than the value predicted by the warm absorber model. Nevertheless, it is conceivable that during this ‘bright’ state observation a relatively unobscured view of the inner region of the stratified warm absorber was obtained. Clearly more intensive monitoring observations by missions such as *XMM* will enable these competing (but undoubtedly incomplete) scenarios to be tested.

Chapter 5

Photoionization in Seyfert galaxies

5.1 Introduction

X-ray emitting plasmas can be divided into two main categories, collision dominated and photoionization dominated. For collisionally-dominated or coronal plasmas, the primary source of ionization is by collisions between electrons and ions. Astrophysical coronal plasmas are generally tenuous, optically thin and very hot ($10^6 - 10^8$ K), examples of which are supernova remnants, the diffuse interstellar medium, intergalactic gas in clusters and the coronae of late-type stars. Photoionization-dominated plasmas are those subject to a strong photoionizing source such as hot stars in the case of H II regions and planetary nebulae, or a hard power-law continuum emitted from the central nuclear region in the case of AGN. In spectroscopic terms the main differences between collision-dominated and photoionization-dominated plasmas are:

- For a given ionization level the electron temperature of a coronal plasma is much higher than in a photoionized plasma.
- A broader range of ionization is observed in photoionized plasmas than in coronal plasmas. Since the photoionizing continuum in AGN is relatively hard, there are enough high energy photons present to produce highly ionized species. In a collision-dominated plasma, however, the electron energy distribution is Maxwellian and electrons with enough energy to eject an electron from an already relatively highly ionized ion are rare.
- Some line ratios are expected to vary widely between gases which are photoionized-

dominated and collision-dominated (e.g. Liedahl *et al.* 1990). Because of the different excitation mechanisms that dominate in photoionized and coronal plasmas, certain line transitions will be more common than others for each type of plasma.

The strongest X-ray emission features from photoionized gases are observed in the 0.5 - 3.0 keV and 6.0 - 7.0 keV bands. Oxygen K, iron L and silicon K line transitions and recombination continua onto highly ionized species of O and Si dominate between 0.5 - 3.0 keV, while emission in the 6.0 - 7.0 keV range is from Fe-K fluorescence. Measuring line-like emission at soft X-ray energies is problematic because of the limited energy resolution of current instruments at these energies and the fact that, at typical Galactic column density values, emission in the softest part of the band is very often strongly attenuated. The presence of highly photoionized gas has been detected at X-ray energies in several Seyfert 1 galaxies and quasars in the form of O VII and O VIII K-edges (e.g. Reynolds 1997, George *et al.* 1998 and references therein). The low line-of-sight absorption by cold gas in most Seyfert 1 galaxies enables the central X-ray source to be seen directly down to soft X-ray energies. Emission intrinsic to photoionized gas, that might lie along the line-of-sight, is therefore swamped by the direct nuclear continuum. The intrinsic continuum in Seyfert 2 galaxies, on the other hand, is generally strongly cut-off below a few keV due to absorption in a high column density gas ($N_H > 10^{22} \text{ cm}^{-2}$) of cold gas. The soft X-ray flux observed in many Seyfert 2 galaxies is thought to be a fraction of the intrinsic continuum which is scattered into the line-of-sight by an electron scattering region which extends, in the plane of the sky, well beyond the obscuring region. The scattered continuum is typically a few percent of the intrinsic continuum and hence much weaker than the soft X-ray continuum of Seyfert 1s. Unless this scattering region is completely ionized, emission and absorption features are expected to be imprinted on the scattered continuum. The equivalent width of line-like emission features will be much greater when measured relative to the scattered continuum.

5.2 The Photoionization code XSTAR

All of the work in this thesis involving the X-ray spectra of highly photoionized gas makes use of the photoionization code XSTAR (Kallman & Krolik 1997). XSTAR is used to calculate the emission and absorption spectra produced by a gas cloud in the vicinity of a point source of continuum radiation. The relative abundance of the ions of a given element are calculated

by assuming a local balance between the ionization rate and recombination rate. The main processes involved in the ionization equilibrium are briefly mentioned below, for a more detailed discussion see Osterbrock (1989) and Kallman & McCray (1982).

5.2.1 Ionization processes

The main source of ionization is photoionization, where a photon of energy $h\nu > h\nu_0^1$ is absorbed by an ion, X^i , and an electron is released, leaving behind an excited ion of ionization state X^{i+1} . The large cross-section for elastic-scattering collisions ensures that the free electrons have a Maxwell-Boltzmann energy distribution. At X-ray energies, photoionization of the inner K-shell electron of low-intermediate Z atoms such as C, N, O and Ne provides the greatest absorption cross-section for these high-energy photons. For the higher Z ($Z \equiv$ atomic number) elements (e.g. Fe) there is a high probability that the ‘hole’ left behind in the K-shell is filled by an L-shell electron which releases a fluorescent K_α photon as it de-excites. This fluorescent photon can, however, further ionize the ion by ejecting one of the outer electrons. This ionization process is called auto-ionization or the Auger effect (Figure 5.1). Other important ionization processes are collisional ionization, which depends on the temperature and density of the gas and charge transfer. Charge transfer reactions occur when a light element such as oxygen loses one of its electrons to a proton: e.g. $O^0 + H^+ \rightarrow O^+ + H^0$

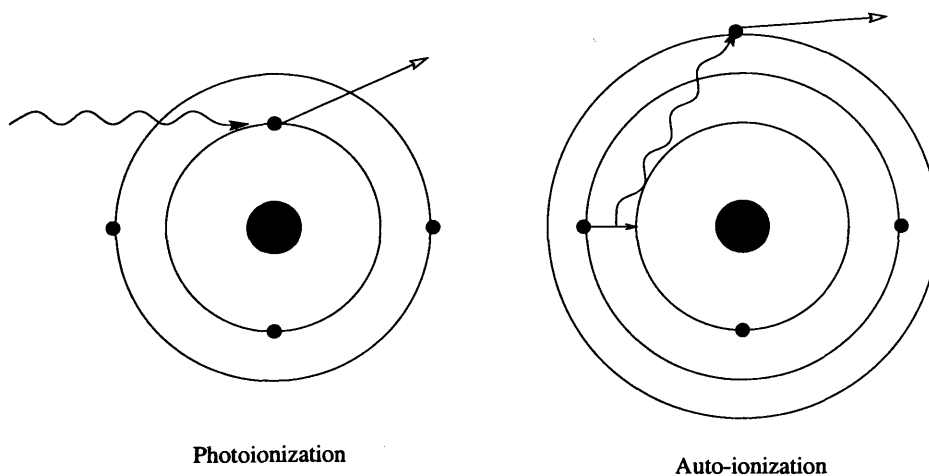


Figure 5.1: Ionization processes

¹ $h\nu_0$ is the ionization potential of an ion and is the minimum amount of energy required to remove a bound electron.

5.2.2 Recombination processes

The capture of a free electron by an ion of ionization state X^i to become X^{i-1} followed by the release of a photon is known as radiative recombination. The electron can recombine either directly into the ground state in one transition or onto excited levels of the ion and then cascade radiatively to the ground level. Dielectronic recombination occurs when a free electron recombines onto an excited level and, instead of releasing a photon, gives up its kinetic energy to excite a second bound electron resulting in a doubly excited ion. This excited state often decays into the ground state via radiative transitions. As mentioned in the previous section charge transfer can be an important ionizing process, however, it can also be important for recombination via the inverse of the reaction in section 5.2.1.

If the gas is in thermal equilibrium then the electron temperature can be calculated by equating the heating rate of the gas to the cooling rate and solving the resultant equations.

5.2.3 Heating processes

- Photoionization heating is the most important source of heating. A photon of energy $h\nu$ is absorbed by an ion and an electron of energy $(h\nu - h\nu_0)$ is ejected. This energy is then spread among the charged particles through elastic collisions.
- Compton scattering is when a photon of energy ϵ_i scatters off an electron, resulting in a photon of energy ϵ_f . The photon energy transfer per scattering is

$$\Delta\epsilon (\equiv \epsilon_f - \epsilon_i) = \frac{\epsilon}{m_e c^2} (4kT - \epsilon) \quad (5.1)$$

If the electrons are energetic enough, such that $4kT > \epsilon$, the photons may gain rather than lose energy, this is called inverse Compton scattering. Therefore, Compton scattering can contribute to both heating and cooling of the gas.

- Charge transfer reactions, as described in § 5.2.1, either input energy into the gas or take energy away depending on whether the reaction is exothermic or endothermic.
- Collisional de-excitation is the process of an inelastic collision between a free electron and an excited ion resulting in a ground-state ion and an electron with increased kinetic energy.

5.2.4 Cooling processes

- Radiative recombination. The mean energy of a recombining electron is $\sim kT$ where T is the electron gas temperature. Hence the energy loss due to radiative recombination is roughly the total number of recombinations for all ions multiplied by kT .
- Dielectronic recombination is also an important cooling mechanism for the range of gas temperature and density considered here.
- Bremsstrahlung emission is due to electron - ion interactions and is the main cooling process at temperatures $T \gtrsim 10^7$ K. A good approximation for bremsstrahlung emissivity (taken from Tucker 1975) is

$$j(T) = 2.4 \times 10^{-27} T^{1/2} n_e^2 \text{ erg cm}^{-3} \text{ s}^{-1} \quad (5.2)$$

where n_e is the electron number density in cm^{-3} .

- Collisional excitation and ionization are both cooling mechanisms since the electron gas loses energy in exciting a bound electron to a higher level which decays rapidly back into the ground state via a radiative transition in the case of collisional excitation, and due to the threshold energy required to eject an electron from an ion in the case of collisional ionization.
- Endothermic charge transfer

5.2.5 XSTAR input parameters

The input parameters required by XSTAR to produce emission and absorption spectra of a photoionized cloud of gas are:

- The source luminosity L in the 0.0136 - 13.6 keV band in erg s^{-1} .
- The element abundance in the gas (see Table 5.1).
- The spectral shape of the central source (Figure 5.2). This was taken to be the same as the one used by Krolik & Kriss (1995) and is typical of Seyfert 1 galaxies.

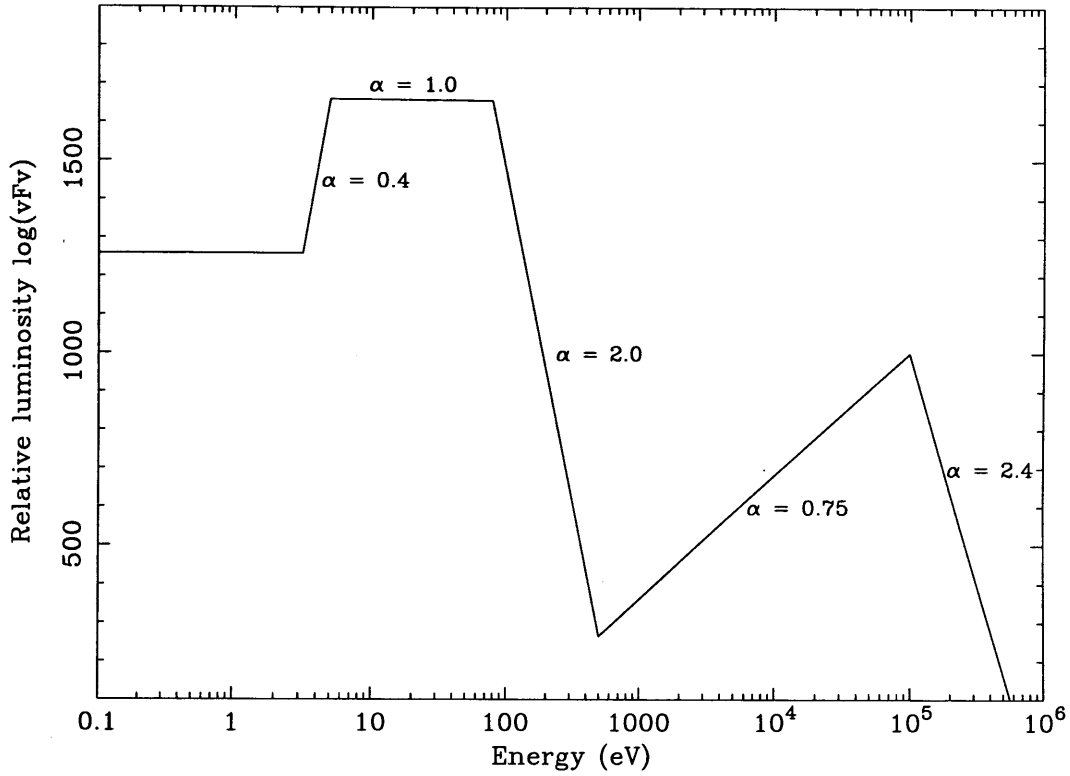


Figure 5.2: The assumed spectral shape of the central ionizing source (from Krolik & Kriss 1995).

- The temperature (T_{warm}) of the gas.
- The number of hydrogen atoms/ions (n) in the gas per cm^3 . The value used here was $n = 10^6 \text{ cm}^{-3}$.
- The ionization parameter ξ which is defined as

$$\xi = \frac{L}{nr^2} \quad (5.3)$$

where r is the distance of the inner edge of the cloud to the central source in cm. The density of the gas was set to be inversely proportional to r^2 ($n \propto r^{-2}$) so that the ionization parameter was constant throughout the cloud.

- The column density $N_{H_{warm}}$ of the cloud.

To simplify the equation of radiative transfer XSTAR assumes a plane parallel geometry for the cloud, a reasonable assumption if the thickness of the cloud is much smaller than its distance

Table 5.1: The element abundances used in XSTAR

Element	Abundance (relative to hydrogen)
Helium	1.0e-1
Carbon	3.7e-4
Nitrogen	1.1e-4
Oxygen	6.8e-4
Neon	2.8e-5
Magnesium	3.5e-5
Silicon	3.5e-5
Sulphur	1.6e-5
Argon	4.5e-6
Calcium	2.1e-6
Iron	2.5e-5
Nickel	2.0e-6

to the ionizing source. Therefore for technical reasons the luminosity was set to $L = 10^{50}$ erg s^{-1} to ensure that for any value of the ionization parameter and column density the distance r of the cloud from the source is always much greater than its thickness, Δr ($\Delta r = \frac{N_{H_{warm}}}{n}$). In the earlier study of the soft X-ray spectrum of Mrk 3 (§ 3.3.3) radiative equilibrium was not assumed but it was found empirically that the Mrk 3 data preferred a plasma temperature of 10^6 K rather than $10^{5.5}$ or 10^5 K. For a non-radiative equilibrium plasma, temperature does not necessarily depend on the ionization parameter and should be considered a free parameter. However, if thermal equilibrium is assumed then the plasma temperature can be inferred from the ionization parameter by using the radiative equilibrium curve (Figure 5.3, right panel). In practice it is possible to run XSTAR with the requirement for thermal equilibrium switched either ‘on’ or ‘off’.

5.2.6 XSTAR output

XSTAR allows the production of table models which can be used in XSPEC. For each cloud with a particular ionization parameter, ξ , and column density, $N_{H_{warm}}$, a table entry is created until a two-dimensional grid of spectral models is produced. Two types of table models are created. The **atables** represent the intrinsic emission of the photoionized plasma in either the

forward direction (i.e. in the direction of the incident continuum) or the backward direction. The **htable** represents the fraction of the incident continuum which emerges from the cloud. In the present modelling, after all effects of absorption (but not elastic scattering) are accounted for, it is assumed that only the un-illuminated side of the cloud is observed and thus the forward atable is used rather than the backward atable. The tabulated spectral information in both the atables and htable encompass an observational bandwidth from 0.1 keV up to 40 keV. In the spectral fitting the free parameters associated with these table models are the ionization parameter, the column density and the normalisation of the atable. XSPEC interpolates between the grid points to obtain the best-fitting spectral parameters.

As was mentioned above, the atable models represent emission that is generated within the cloud only. They do not include the fraction of the intrinsic continuum that is scattered into the line-of-sight by free electrons which probably accounts for the majority of the soft flux observed in Seyfert 2 galaxies. Therefore, when modelling the X-ray spectra of the Seyfert 2s, an additional ‘scattered’ power-law component is used with the photon index tied to that of the hard continuum. Assuming that the scattered flux and the diffuse emission originate in the same medium then the scattered power-law must be convolved with the htable to account for absorption by the cloud and the normalisation of the atable should, in some way, be tied, to the normalisation of the scattered power-law.

According to the XSTAR manual (Kallman & Krolik 1997) the units of the atable are in counts per bin C_n^{mod} , scaled in relation to the computed specific luminosities L_ϵ as

$$C_n^{mod} = L_\epsilon 10^{-11} \frac{\Delta\epsilon}{\epsilon} \quad (5.4)$$

where L_ϵ is the specific luminosity of the emitting region at energy ϵ in units of $10^{38} \text{ erg s}^{-1} \text{ erg}^{-1}$ and $\Delta\epsilon$ is the corresponding bandwidth (in energy units) of the bin. Assuming the spectral model is an accurate description, the observed counts per bin C_n^{obs} depends on the covering fraction f_{cov} ($\equiv \frac{\Omega}{4\pi}$) of the gas and its distance D from the observer.

$$C_n^{obs} = 10^{38} L_\epsilon \frac{\Delta\epsilon}{\epsilon} \frac{f_{cov}}{4\pi D^2} \quad (5.5)$$

Hence the normalisation K of the atable is

$$K = \frac{C_n^{obs}}{C_n^{mod}} = \frac{10^{49} f_{cov}}{4\pi D^2} \quad (5.6)$$

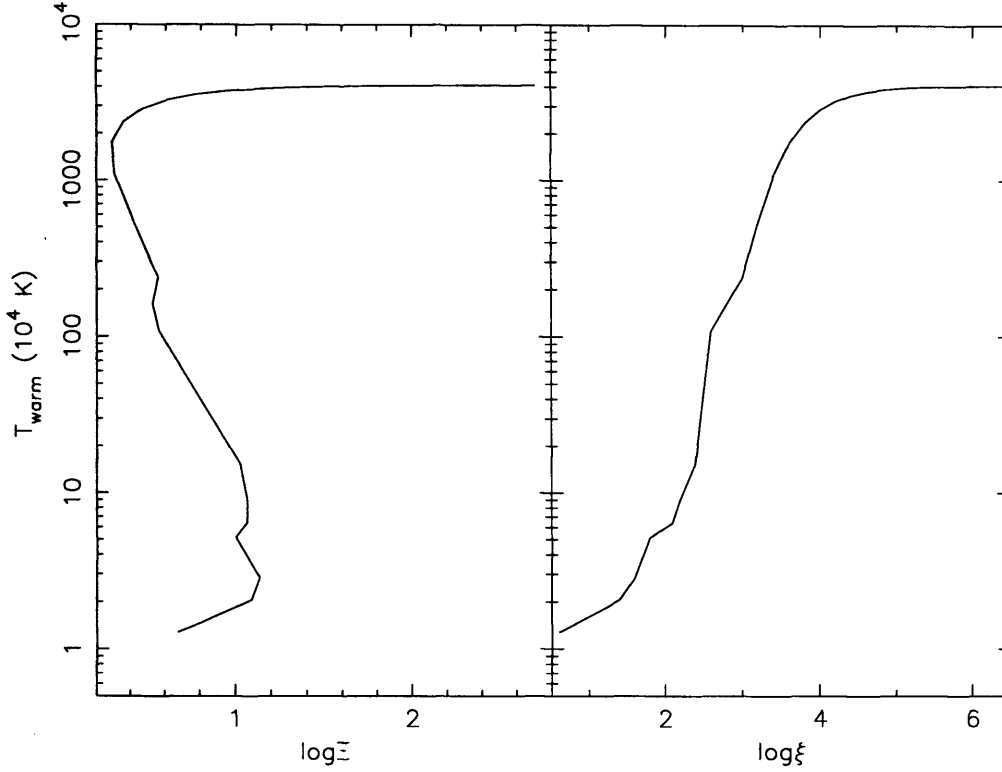


Figure 5.3: Radiative equilibrium curves, produced from the output of XSTAR, of Ξ (left panel) and ξ (right panel) versus T_{warm} for a gas of density $n = 10^6 \text{ cm}^{-3}$ and column $N_H = 10^{23} \text{ cm}^{-2}$. Note that Ξ is a version of the ionization parameter involving the pressure in the photoionized gas and is proportional to $\frac{\xi}{T_{warm}}$.

The amount of intrinsic flux scattered into the line-of-sight by the photoionized gas is dependent on both the covering fraction f_{cov} and column density $N_{H_{warm}}$ of the scattering medium. The normalisation of the scattered power-law A_{scatt} can therefore be written in terms of the hard power-law normalisation A_{int} as

$$A_{scatt} = f_{cov} 1.2 \sigma_T N_{H_{warm}} A_{int} = f_{cov} 0.08 N_{H_{23}} A_{int} \quad (5.7)$$

where $N_{H_{23}} = 10^{23} N_{H_{warm}}$. Using the input spectrum shown in Figure 5.2 the integrated flux F between 0.0136 - 13.6 keV equates to

$$F = \int_{0.0136}^{0.079} A E^{-1.0} dE + \int_{0.079}^{0.5} B E^{-2.0} dE + \int_{0.5}^{13.6} C E^{-0.75} dE \quad (5.8)$$

where A, B and C are the power-law normalisations in units of $\text{keV cm}^{-2} \text{ s}^{-1} \text{ keV}^{-1}$ at 1 keV. Substituting A and B in terms of C and integrating Equation 5.8 gives

$$F = 2.9 \times 10^{-8} C = 2.9 \times 10^{-8} A_{\text{int}} \text{ erg cm}^{-2} \text{ s}^{-1} \quad (5.9)$$

since $C \equiv A_{\text{int}}$. For the spectral models the luminosity of the photoionized gas $L = 4\pi D^2 F = 10^{50} \text{ erg s}^{-1}$ (for the technical reasons referred to earlier in § 5.2.5), hence substituting $4\pi D^2$, F and A_{int} in equation 5.6 using equations 5.7 and 5.9 gives

$$K = \frac{3.6 \times 10^{-8}}{N_{H_{23}}} A_{\text{scatt}} \quad (5.10)$$

Equation 5.10 specifies the predicted relationship between the electron scattered continuum and intrinsic emission from the photoionized gas.

Figure 5.4 shows the predicted 0.2-5.0 keV spectral forms from a photoionized plasma, in thermal equilibrium, with a range of ionization parameters ($\log \xi = 2.0-4.0$). The gas column density is taken to be $N_{H_{\text{warm}}} = 10^{23} \text{ cm}^{-2}$. At $\log \xi = 4.0$ every element is stripped of its electrons and the temperature of the gas, which is controlled by Compton heating and cooling, is $\sim 10^{7.5} \text{ K}$. Any intrinsic emission is in the form of free-free emission (or bremsstrahlung). The total expected luminosity due to bremsstrahlung emission is

$$L_{\text{brems}} = j(T) 4\pi r^2 \Delta r \quad (5.11)$$

Substituting $j(T)$ and r using equations 5.2 and 5.3 respectively and Δr with $\frac{N_{H_{\text{warm}}}}{n}$ gives

$$L_{\text{brems}} = 2.1 \times 10^{-26} T^{1/2} L N_{H_{\text{warm}}} \xi^{-1} \propto T^{1/2} \xi^{-1} \quad (5.12)$$

Therefore, as is shown above, although an increase in temperature does increase the flux produced by bremsstrahlung, a high ξ means that it is small compared to the scattered flux. Thus only purely scattered flux is expected from very highly ionized gas (Figure 5.4, panel a). If the ionization parameter is decreased by an order of magnitude ($\log \xi = 3.0$), then flux due to intrinsic emission is comparable to that from scattered emission. The temperature of the plasma is now $\sim 2 \times 10^6 \text{ K}$ and bremsstrahlung emission contributes only below 0.5 keV. There are several strong lines (e.g. O VIII K_α at 0.654 keV) but the bulk of the soft X-ray flux that is intrinsic to the photoionized plasma comes from recombination continua onto highly ionized species of carbon, nitrogen, oxygen, iron, silicon and sulphur (Figure 5.4, panel b). Note that the relatively strong, broad emission feature between 0.87-1.3 keV is the O VIII radiative recombination continuum (RRC). The width of the feature is due to the Maxwellian velocity distribution of

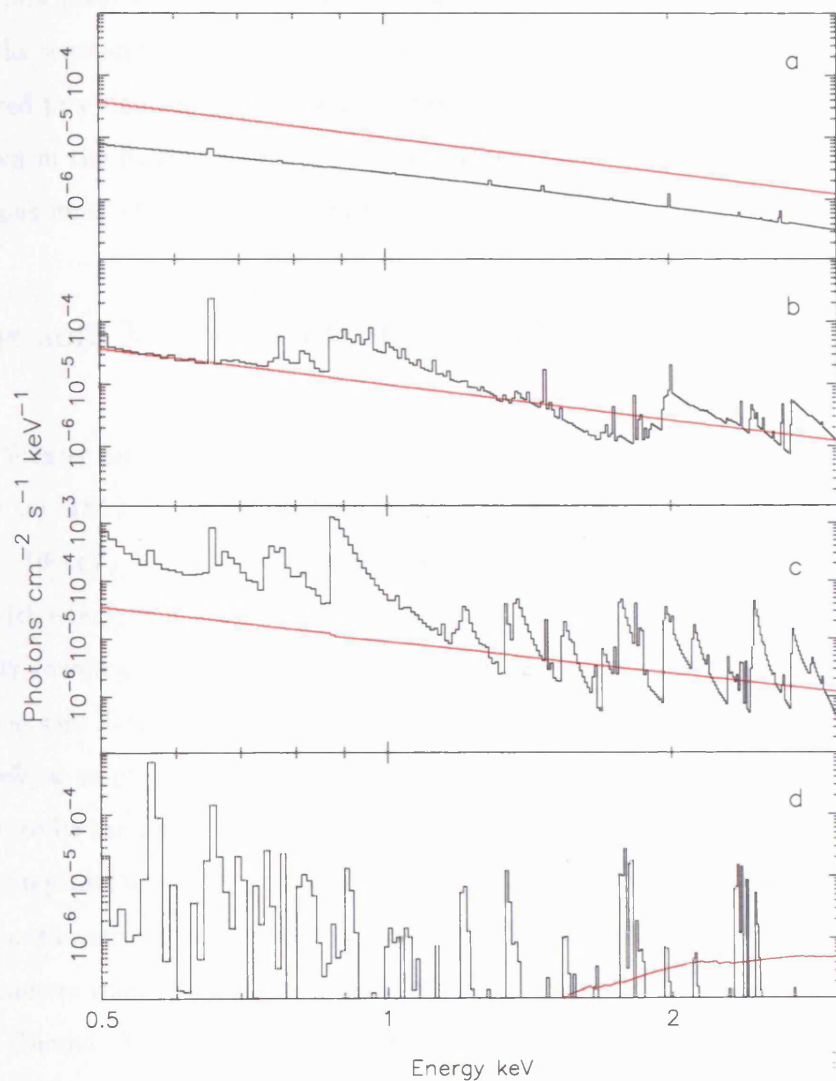


Figure 5.4: The scattered and intrinsic emission from a photoionized gas (shown respectively as the red and black components). The four panels correspond to $\log \xi$ of (a) 4.0; (b) 3.0; (c) 2.5; (d) 2.0.

the electrons in the plasma. When $\log \xi = 2.5$ the temperature of the gas is $\sim 4 \times 10^5$ K and the RRC are even stronger, reflecting the dependence of the radiative recombination rate, α_r , on the electron temperature, $\alpha_r \propto T^{-1/2}$. Panel c of Figure 5.4 shows that the widths of the RRC are narrower at the lower temperature and demonstrates that RRC can be used to measure the temperature of a plasma directly. At $\log \xi = 2.0$ there is no sign of the O VIII recombination feature and the scattered continuum is heavily absorbed (Figure 5.4, panel d). The attenuation of the scattered flux also provides an explanation for the absence of the O VIII RRC. Although it is not shown in the figure there is a very strong edge at 0.74 keV. This indicates that under these conditions most of the oxygen is in O VII and not O IX.

5.3 The soft X-ray spectrum of NGC 4151

This section focuses on the soft X-ray spectrum of NGC 4151 using SIS (S0+S1) data from a deep (~ 100 ks) ASCA observation performed in May, 1995. In the previous chapter (§ 4.3) the hard (2 - 10 keV) X-ray spectrum of NGC 4151 was described by an intrinsic power-law continuum with energy index at $\alpha = 0.6$, heavy and complex absorption, represented by up to three partially covering absorbers, and a broad iron K_α emission line. The extrapolation of this model into the soft X-ray band suggests that the direct flux makes no significant contribution below ~ 1 keV, a point which is discussed further below. The excess flux observed in the soft band is taken to be the result of scattering of the nuclear continuum. As a preliminary step this soft excess is represented by a power-law component with a spectral slope equivalent to that of the hard continuum with attenuation due to the line-of-sight Galactic gas (N_{Gal}) only. The best-fit parameters when the above model is applied to the whole 0.7 - 10.0 keV band are given in Table 5.2 (Model 1). It is immediately obvious, from the χ^2 fit and the corresponding SIS count rate residuals (Figure 5.5) that pure electron scattering alone cannot adequately describe the soft X-ray spectrum of NGC 4151. The largest discrepancy between the data and this model is the presence of a line-like feature at ~ 0.9 keV, very similar to the feature observed in Mrk 3 (see § 3.3.3).

Evidence for this line-like feature has also been found by other authors in previous ASCA observations of NGC 4151. Weaver *et al.* (1994b) reported an unresolved emission line at 0.88 ± 0.02 keV with an equivalent width of $EW \sim 45$ eV in the PV1 spectrum of NGC 4151. If the

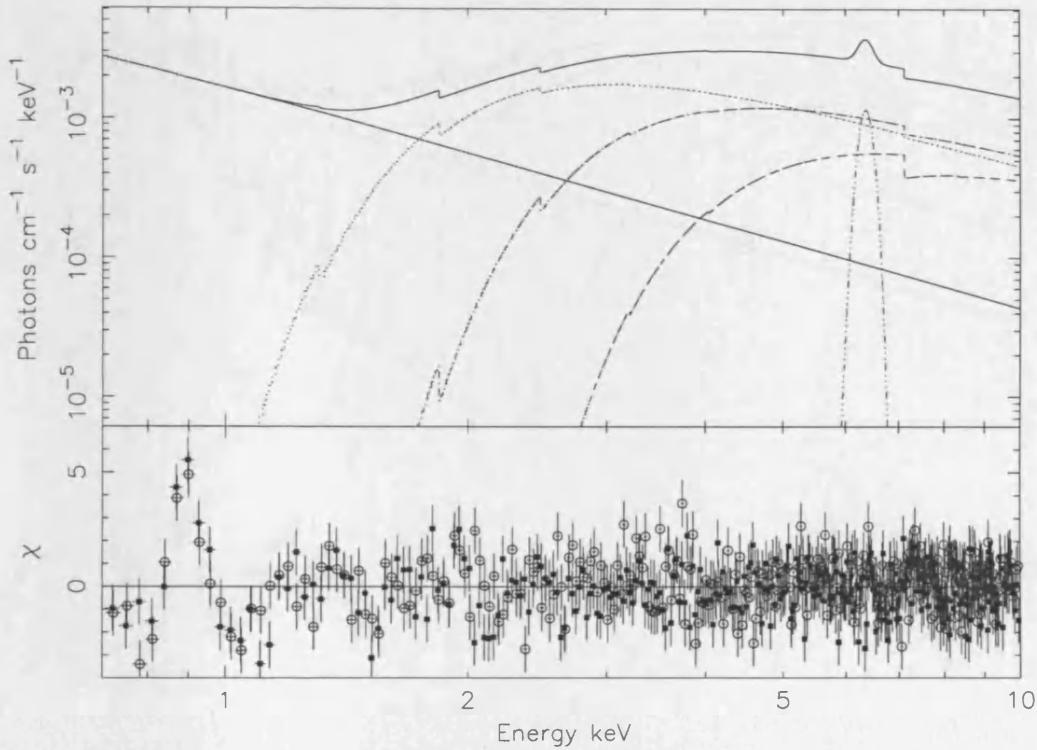


Figure 5.5: The best-fit input spectrum (upper panel) and corresponding count rate residuals (lower panel) to the S0 (filled squares) and S1 (open circles) spectra of NGC 4151 using Model 1.

feature in the present data is modelled by adding a narrow ($\sigma = 0.01$ keV) gaussian to Model 1, an energy and equivalent width of ~ 0.90 keV and ~ 54 eV respectively is obtained, entirely consistent with the results of Weaver *et al.* (1994b) mentioned above. In addition, this model (Model 2, Table 5.2) gives a huge improvement in χ^2 of $\Delta\chi^2 \sim 128$ compared to Model 1.

Model 2, however, is rather unphysical. ROSAT HRI observations of NGC 4151 (Morse *et al.* 1995) have shown that ~ 31 percent of the total 0.1 - 2.4 keV flux is extended on a scale of ~ 15 arcsec. Thermal emission from hot diffuse gas could therefore contribute significantly to the flux at 1 keV. The gaussian line was replaced, firstly, by a Raymond-Smith thermal plasma (Model 3a) and also by a MEKAL thermal component (Model 3b). While Model 3b gives a much better fit to the data than Model 3a (although a plasma temperature of ~ 0.7 keV was preferred by both; see Table 5.2), neither model describes the soft X-ray spectrum of NGC 4151 in a satisfactory manner. Warwick, Done & Smith (1995) reported that a scattered power-law continuum plus emission from a Raymond-Smith plasma only gave an acceptable fit to quasi-

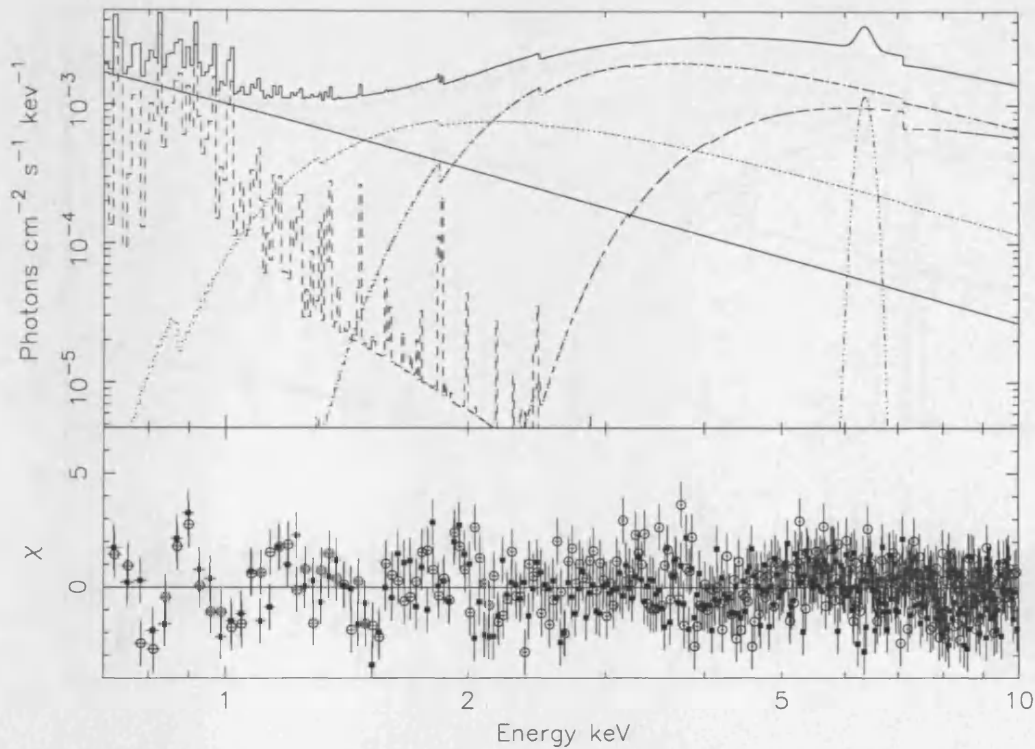


Figure 5.6: The best-fit input spectrum (upper panel) and corresponding count rate residuals (lower panel) to the SIS spectra of NGC 4151 using Model 3b.

simultaneous *ROSAT* PSPC/*Ginga* data when the metal abundance of the thermal emission was very low (~ 2 percent solar). The *ASCA* data also prefer a low metal abundance (~ 4 percent solar), however it is only loosely constrained. The problem with the thermal plasma fits seems to be that the predicted broad hump, from oxygen and iron L lines, is incompatible with the sharp feature present at ~ 0.9 keV (Figure 5.6).

Thus far it has been assumed that the scattering region is fully ionized and therefore produces a featureless scattered continuum. The next step is to consider a scenario similar to that employed earlier in the case of Mrk 3 (§ 3.3.3) where the scattering region is only partially ionized. The initial approach was to attempt to fit the soft ($\lesssim 1.5$ keV) excess flux entirely in terms of a single partially ionized scattering region with both the ionization and thermal equilibrium requirements in operation. The normalisation of the atable was determined in accordance with Equation 5.10, in effect enabling it to be tied to the normalisation of the scattered power-law. Unfortunately this model immediately ran into problems, to obtain a relatively low equivalent width for the

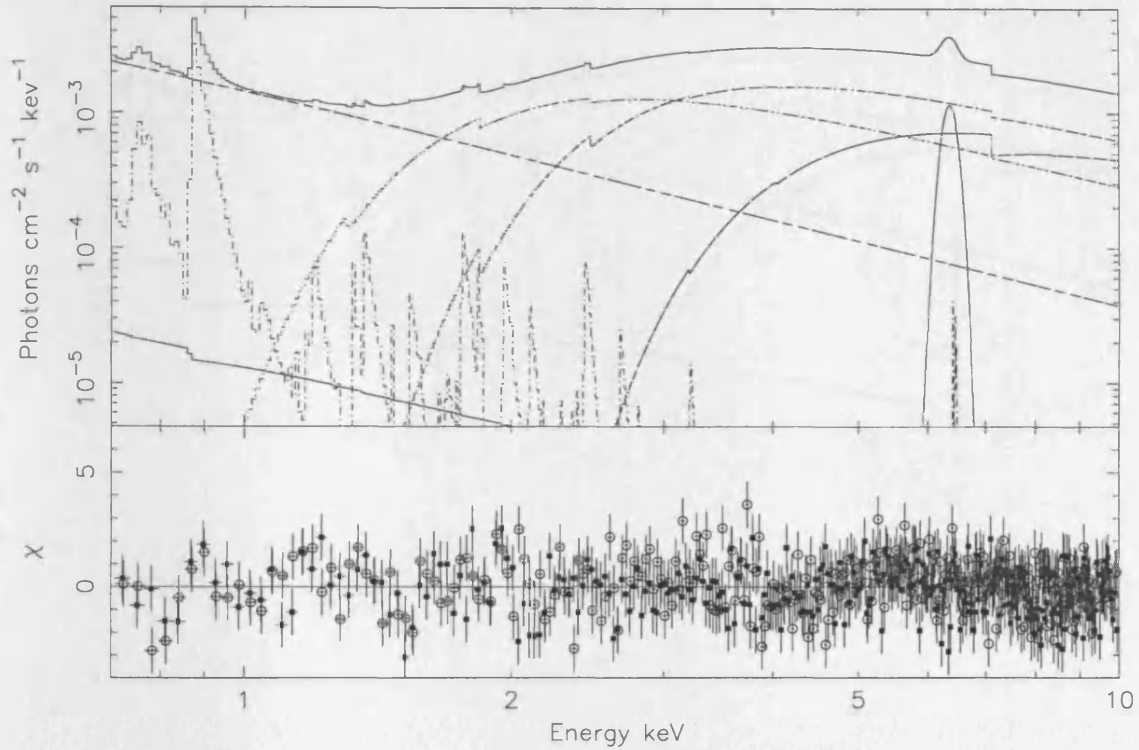


Figure 5.7: The best-fit input spectrum (upper panel) and corresponding count rate residuals (lower panel) to the SIS spectra of NGC 4151 using Model 5.

feature at ~ 0.9 keV the ionization parameter must be quite high (e.g. $\xi \gtrsim 3$ in Fig. 5.4). This leads to a broader 0.9 keV feature and therefore gives a poor fit to the spectrum. To circumvent this problem photoionization models were tried in which ionization equilibrium was assumed but not radiative equilibrium (this was the approach adopted earlier for Mrk 3). The excellent signal-to-noise ratio obtained in the long observation of NGC 4151 allows the introduction of the temperature T_{warm} of the plasma as a free parameter, in addition to the ionization parameter ξ and column density N_{Hwarm} . This photoionization model provides a much better description of the soft X-ray spectrum of NGC 4151 than either of the thermal models (Table 5.2, Model 4) and interprets the 0.9 keV feature as recombination directly into the ground state of fully ionized oxygen. The best-fit parameters for this model require the scattering region to be very highly ionized indeed ($\log \xi \sim 4.8$) but the temperature to be only $T_{warm} \sim 3 \times 10^5$ K. At these ionization parameters the emission and absorption properties of the plasma are largely independent of the gas column density. N_{Hwarm} is therefore fixed at $N_{Hwarm} = 3.0 \times 10^{23} \text{ cm}^{-2}$, the value obtained from Equation 5.7, where $\frac{A_{scatt}}{A_{int}} \equiv f_{scatt1} = 0.024$ (Model 4, Table 5.2) and a

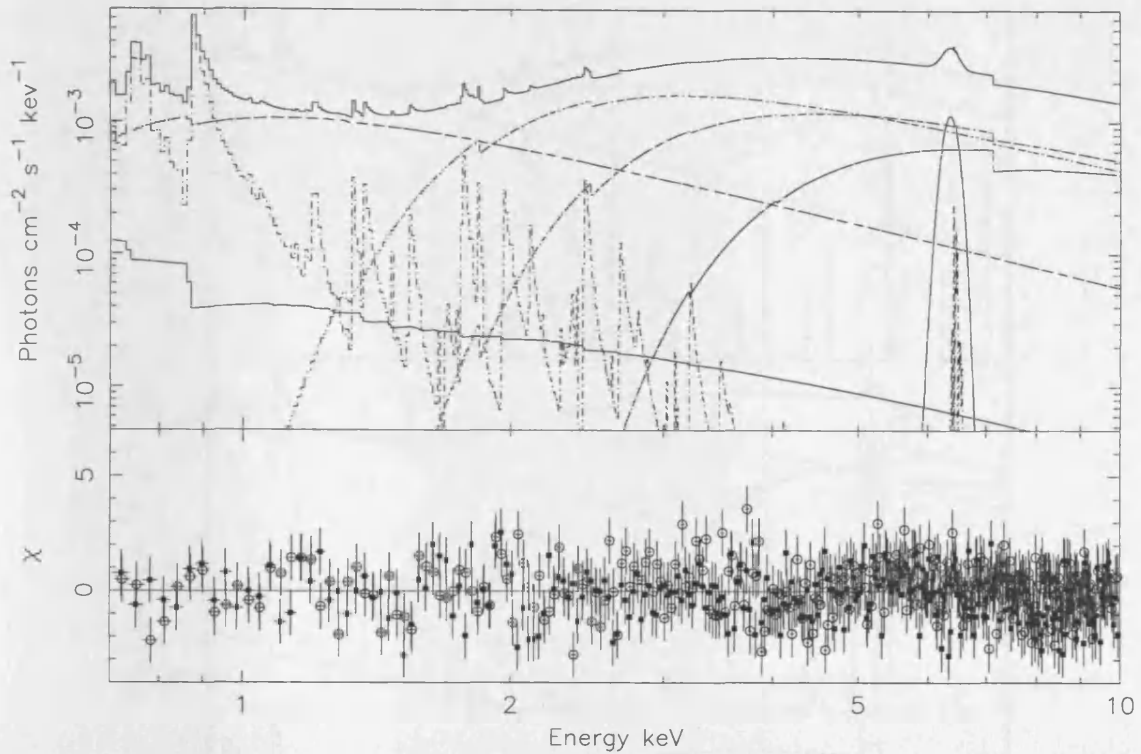


Figure 5.8: The best-fit input spectrum (upper panel) and corresponding count rate residuals (lower panel) to the SIS spectra of NGC 4151 using Model 6.

covering fraction of $f_{cov} = 0.1$ is assumed. The inferred temperature of the gas seems physically unreasonable since such a highly ionized plasma would be driven to its Compton temperature which is two orders of magnitude higher ($\sim 4 \times 10^7$ K; Fig 5.3).

The search for a physically more realistic scenario meant a return to the models that employ both ionization and thermal equilibrium; under these conditions the temperature of the gas corresponds to a certain value of ξ and is not required as a free parameter in the spectral fit. A possible explanation for the small EW of this O VIII recombination feature is that a significant fraction of the soft flux is due to scattered emission from fully ionized gas. The results of replacing the atable and mtable in Model 4 with ones that assume ionization and thermal equilibrium and the addition of a second scattered power-law are given in Table 5.2 (Model 5). Physically, this model could be interpreted in two ways; (i) as highly ionized hot gas, containing small, high density cooler clouds with a much smaller covering fraction or (ii) as two separate regions, a hot, completely ionized region and a cooler region situated further out from the source. In

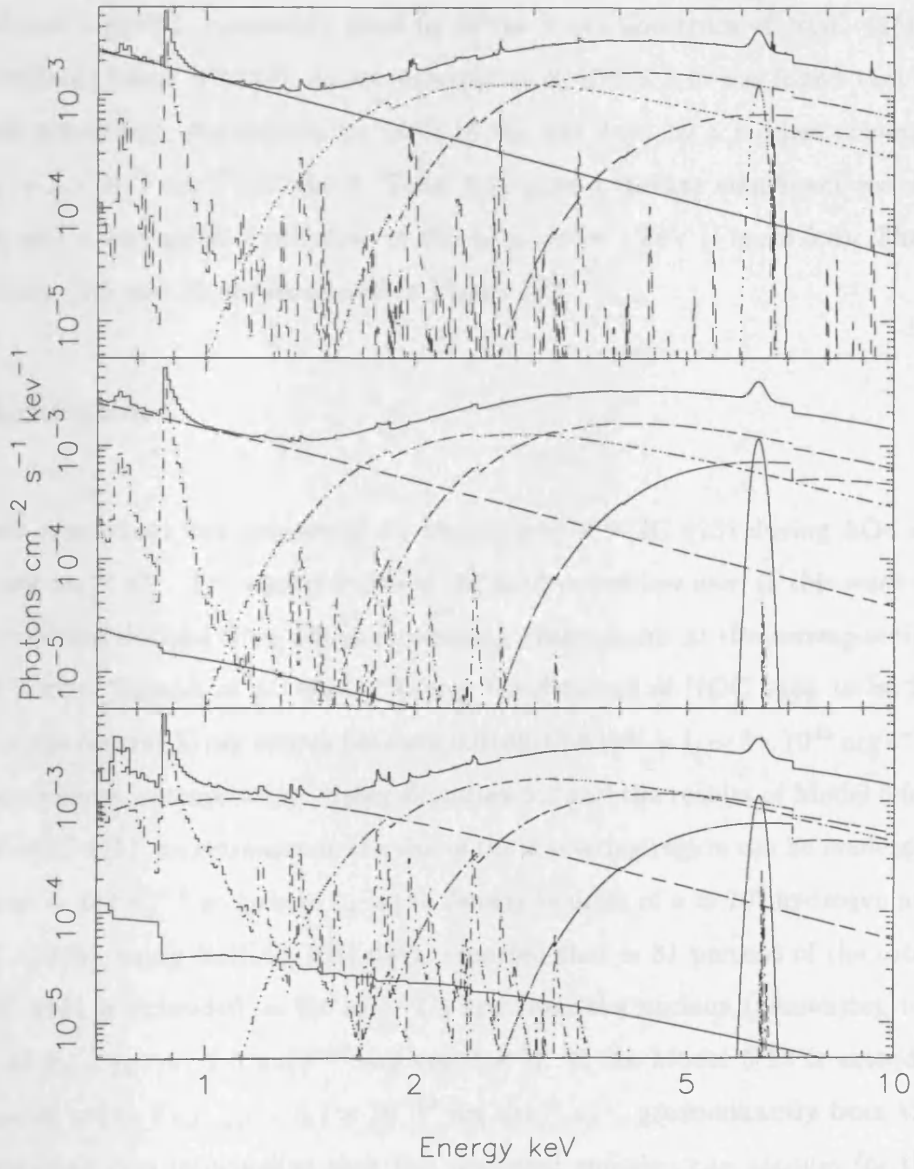


Figure 5.9: For comparison, plots of Models 4(top), 5(middle) and 6(bottom) in the 0.7-10.0 keV band.

both scenarios the hot plasma produces purely scattered flux and the cooler gas produces the O VIII recombination feature. This model (Model 5, Table 5.2) provides the best description so far ($\chi^2/\text{d.o.f.} = 761.6/605$). The best-fit value for the ionization parameter is more than two orders of magnitude lower ($\log \xi \sim 2.5$) than the one obtained with Model 4. According to the radiative equilibrium curve plotted in Figure 5.3 this ionization parameter corresponds to a temperature of $T_{\text{warm}} \sim 4 \times 10^5$ K, consistent with the temperature obtained with Model 4.

Although Model 5 gave a reasonably good fit to the X-ray spectrum of NGC 4151 there were still some residuals below 0.9 keV. As an elaboration of Model 5 it was found that attenuating the scattered power-law, responsible for most of the soft flux, by a modest column density of gas of $N_{H4} \sim 3 \times 10^{21} \text{ cm}^{-2}$ (Model 6, Table 5.2) gave a further significant reduction in the χ^2 residuals and a very good description of the data below 1 keV (Figure 5.8). The competing spectral models (4,5 and 6) are compared in Figure 5.9.

5.4 Discussion

The 2-10 keV continuum flux (corrected for absorption) of NGC 4151 during AO4 was $F_{2-10}^{int} = 3.0 \times 10^{-10} \text{ erg cm}^{-2} \text{ s}^{-1}$. The energy index of the hard power-law used in this work of $\alpha = 0.6$ is consistent with that derived from *Ginga* monitoring observations at the corresponding flux level (see Figure 2 from Yaqoob *et al.* 1993). Taking the distance of NGC 4151 to be 20 Mpc, the luminosity of the central X-ray source between 0.0136-13.6 keV is $L \sim 3 \times 10^{43} \text{ erg s}^{-1}$ (assuming that the source emits isotropically). Using Equation 5.3 and the results of Model 5 for the X-ray spectrum of NGC 4151, an estimate on the size of the scattering region can be made giving $r \sim 3 \times 10^{17} n_6^{-0.5} \text{ cm} \sim 0.2 n_6^{-0.5} \text{ pc}$ (where n_6 is the density in units of $n = 10^6$ hydrogen nuclei cm^{-3}). Morse *et al.* (1995), using *ROSAT* HRI data, reported that ~ 31 percent of the total 0.1-2 keV flux in NGC 4151 is extended as far as ~ 1.5 kpc from the nucleus (amounting to a resolved component of $F_{0.1-2.0} \sim 2.5 \times 10^{-12} \text{ erg cm}^{-2} \text{ s}^{-1}$). If the Model 5 fit is extended down to 0.1 keV it gives a flux $F_{0.1-2.0} \sim 5.7 \times 10^{-12} \text{ erg cm}^{-2} \text{ s}^{-1}$, predominantly from the scattered emission. However it is implausible that this scattered emission can account for the extended component observed by the *ROSAT* HRI (see above). An alternative possibility is that the extended emission observed in the HRI is due to ultra-soft flux below 0.6 keV, possibly from a $\sim 10^6$ K thermal plasma (Warwick, Done & Smith 1995). In fact with the inclusion of a Raymond-Smith component at a temperature $kT=0.13$ keV and normalisation $A_{kT} = 2.2 \times 10^{-4} \text{ cm}^{-5}$, parameter values that gave a good fit to the soft (0.1-1.0 keV) *ROSAT* PSPC data (Warwick, Done & Smith 1995), an additional observed flux, of $F_{0.1-2.0} \sim 2.6 \times 10^{-12} \text{ erg cm}^{-2} \text{ s}^{-1}$ is obtained. This is in excellent agreement with the amount of resolved emission measured by the HRI. This soft thermal emission has no impact on the *ASCA* spectral fits. (The Raymond-Smith model predicts a strong O VII K_α line at 0.57 keV, however the presence of such a line cannot be confirmed with the *ASCA* data).

Table 5.2: Spectral fitting of the SIS spectra of NGC 4151

Parameter	Model 1	Model 2	Model 3a	Model 3b	Model 4	Model 5	Model 6
α	0.60	0.60	0.60	0.60	0.60	0.60	0.6
A_{int}^a	$6.3^{+0.6}_{-1.1}$	$6.4^{+1.0}_{-1.2}$	$6.4^{+1.0}_{-1.2}$	$6.3^{+0.5}_{-0.7}$	$6.3^{+1.0}_{-1.1}$	$6.4^{+2.5}_{-0.9}$	$6.3^{+1.1}_{-1.8}$
N_{H1}^b	$36.0^{+6.1}_{-2.6}$	$33.8^{+7.5}_{-5.0}$	$32.4^{+7.3}_{-5.4}$	$27.2^{+4.3}_{-3.7}$	$33.1^{+6.6}_{-5.2}$	$32.7^{+6.0}_{-10.6}$	$34.3^{+8.8}_{-6.2}$
C_{f1}	0.32	0.36	0.39	0.47	0.37	0.39	0.35
N_{H2}^b	$13.0^{+2.2}_{-0.8}$	10.2 ± 1.2	$9.2^{+2.2}_{-1.0}$	$6.8^{+0.8}_{-0.9}$	$9.7^{+1.7}_{-1.6}$	$9.5^{+1.5}_{-4.7}$	$11.6^{+3.7}_{-2.8}$
C_{f2}	0.38	0.42	0.43	0.45	0.45	0.43	0.36
N_{H3}^b	4.2 ± 0.2	$3.4^{+0.3}_{-0.4}$	3.1	1.7 ± 0.3	$3.3^{+0.3}_{-0.4}$	$3.2^{+0.3}_{-0.8}$	$4.5^{+0.6}_{-0.7}$
C_{f3}	0.30	0.21	0.17	0.08	0.18	0.18	0.29
f_{scatt1}^e	2.7	2.5	2.3	1.7	2.4	0.025	0.21
f_{scatt2}^e						2.3	3.6
N_{H4}^b							$0.30^{+0.10}_{-0.13}$
E_{ga}^c		0.89 ± 0.01					
A_{ga}^d		$10.5^{+1.6}_{-1.4}$					
kT^c			$0.71^{+0.04}_{-0.02}$	$0.67^{+0.02}_{-0.03}$			
A_{kT}			$9.6^{+5.4}_{-0.9}$	$27.2^{+8.1}_{-6.2}$			
$\log \xi$					$4.73^{+0.15}_{-0.12}$	$2.44^{+0.09}_{-0.07}$	2.48 ± 0.02
N_{Hwarm}^b					30.0(fixed)	$1.0^{+1.4}_{-0.0*}$	$7.8^{+1.3}_{-2.6}$
$\log T_{warm}$					$5.45^{+0.12}_{-0.14}$		
χ^2	932.6	761.0	862.4	816.7	775.0	761.5	738.9
d.o.f.	608	606	606	606	606	605	604

^a 10^{-2} photon $\text{cm}^{-2} \text{s}^{-1} \text{keV}^{-1}$.^b 10^{22}cm^{-2} .^c keV.^d 10^{-5} photon $\text{cm}^{-2} \text{s}^{-1}$.^e scattered fraction in percentage

* reached lower limit of model

The flux density of NGC 4151 at 60 μm and 100 μm is ~ 5.64 Jy and 8.50 Jy respectively (Rush, Malkan & Spinoglio 1993). These far infra-red luminosities can be used, with the correlations discovered by David, Jones & Forman (1992), to estimate an upper limit on the contribution to the observed soft X-ray flux in NGC 4151 from starburst emission. Specifically, the maximum contribution to the 0.5-4.5 keV band expected from starburst activity is $1.6 \times 10^{-13} \text{erg cm}^{-2} \text{s}^{-1}$, approximately 0.5 percent of that observed (i.e. $F_{0.5-4.5} = 4.1 \times 10^{-11} \text{erg cm}^{-2} \text{s}^{-1}$). However a large fraction of this observed flux (about 87 percent) is probably the direct continuum (albeit absorbed). For comparison, the mekal component of Model 3b (Table 5.2) has a flux $F_{0.5-4.5} = 6.5 \times 10^{-13} \text{erg cm}^{-2} \text{s}^{-1}$, a factor of four greater than predicted. This, combined with the fact that the thermal models (Models 3a and 3b) cannot satisfactorily describe the 0.9 keV feature makes it very likely that the soft X-ray flux in NGC 4151 around 1 keV is due to photoionized plasma emission rather than thermal emission.

The first photoionization model used in § 5.3 (Model 4) does not assume that the gas is in thermal equilibrium. The best-fit parameters describing the state of the gas are an ionization parameter of $\xi \sim 10^{4.8}$ and a temperature $T \sim 3 \times 10^5$ K, much lower than that expected for a gas with an equivalent ionization parameter in thermal equilibrium. However it is not necessarily a requirement that the gas be in thermal equilibrium. If the gas expands, adiabatic cooling might keep the temperature well below the Compton temperature. Krolik & Begelman (1986) discussed this possibility in the form of an X-ray heated wind in NGC 1068. From their work the temperature of such a wind at a distance r from a source of luminosity L_{44} (in units of $10^{44} \text{erg s}^{-1}$ between 0.0136-13.6 keV) can be estimated from

$$T \approx 1 \times 10^6 L_{44}^{2/3} \left(\frac{T_{c,eff}}{1.5 \times 10^7 \text{K}} \right)^{2/3} r_{pc}^{-2/3} \text{K} \quad (5.13)$$

The results of Model 4 in Table 5.2 give a luminosity for NGC 4151 of $L_{44} \sim 0.3$ and, for $\log \xi = 4.8$, a distance $r \sim 7 \times 10^{-3} n_6^{-0.5} \text{pc}$. Substituting these values into the above equation and assuming that $T_{c,eff} = 1.5 \times 10^7 \text{K}$ gives a temperature of $T \approx 1.2 \times 10^7 \text{K}$ which is again inconsistent with that inferred in the model. This confirms an earlier conclusion that Model 4 is physically unrealistic.

When this photoionized gas is taken to be in thermal as well as ionization equilibrium the low observed EW of the O VIII RRC cannot be reproduced by a single uniform region of gas. A

way of overcoming this problem is to allow the bulk of the soft X-ray continuum to come from a hot fully ionized medium that dilutes intrinsic emission features from cooler material (Model 5). As mentioned earlier in § 5.3 there are two plausible settings in which two scattering regions could co-exist. Using the results obtained with Model 5 (Table 5.2) these scenarios are discussed further. In the first scenario (Figure 5.10), the relatively cool clouds are immersed in the hot gas, similar to the ‘two-phase model’ of emission line regions discussed by Krolik, McKee & Tarter (1981). In this two-phase model the media are assumed to be in pressure equilibrium so that

$$n_{hot}T_{hot} = n_{warm}T_{warm} \quad (5.14)$$

It is also true, from equation 5.3, that

$$\xi_{hot}n_{hot} = \xi_{warm}n_{warm} \quad (5.15)$$

therefore

$$\frac{\xi_{hot}}{\xi_{warm}} = \frac{T_{hot}}{T_{warm}} \quad (5.16)$$

In the modelling the warm gas is assumed to be in thermal equilibrium, therefore the best-fit $\xi_{warm} \sim 10^{2.5}$ corresponds to a temperature of $T_{warm} \sim 10^{5.5}$ K. If the hot gas is fully ionized then $T_{hot} \gtrsim 10^{7.5}$ K. Substituting these values into equation 5.16 gives $\xi_{hot} \sim 10^{4.5}$ hence the physical state of the hot gas is also consistent with being in thermal equilibrium (see Figure 5.3). Assuming a covering fraction $(f_{cov})_{hot} = 0.1$ for the hot gas and taking the scattered fraction $f_{scatt2} (\equiv \frac{A_{scatt}}{A_{int}}) = 0.023$ (Model 5, Table 5.2) implies a column density of $N_{Hhot} \sim 3 \times 10^{23} \text{ cm}^{-2}$. The requirement $r \gtrsim \Delta r$ means that

$$n_{hot} \gtrsim \frac{N_{Hhot}^2 \xi_{hot}}{L} \gtrsim 10^8 \text{ cm}^{-3} \quad (5.17)$$

and therefore, using equation 5.14, $n_{warm} \gtrsim 10^{10} \text{ cm}^{-3}$. This value is quite close to the assumed density of the clouds in the BLR, if this density is plugged back into equation 5.3 a distance of $r \sim 10^{15.5} \text{ cm}$ is obtained. The covering fraction of the cooler gas is $(f_{cov})_{warm} = \frac{2.5 \times 10^{-4}}{0.08 \times 0.1} \sim 0.03$, approximately a third of the covering fraction of the hot, highly ionized region. There is however a problem with this two-phase model, the cooler gas lies on the part of the thermal equilibrium curve in Figure 5.3 (left panel) that is unstable to perturbations of temperature. A small increase in the temperature of the cooler plasma would result in runaway heating and the evaporation of the gas cloud on a relatively short time-scale. For example, if the cloud lifetime is of the

same order as the bremsstrahlung cooling time for the hot gas, $t_{\text{cloud}} = 2.2 \times 10^{11} T^{0.5} n_{\text{hot}}^{-1} \sim 5$ months, therefore variability in the strength of the O VIII recombination feature would be expected on this time-scale. As is shown below, this is not observed.

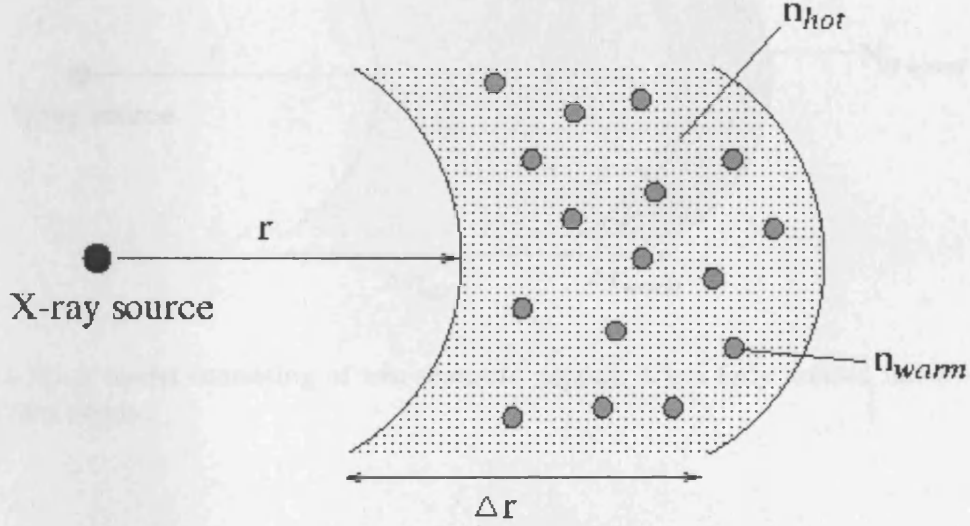


Figure 5.10: The two-phase model in which clouds of relatively cool gas are immersed in pressure equilibrium with a much hotter plasma.

In the second scenario (Figure 5.11) both the hot and warm gas have the same covering fraction, $(f_{\text{cov}})_{\text{hot}} = (f_{\text{cov}})_{\text{warm}} = 0.03$. The ratio of the two scattering fractions f_{scatt1} and f_{scatt2} therefore gives

$$\frac{N_{H\text{hot}}}{N_{H\text{warm}}} = \frac{2.3 \times 10^{-2}}{2.5 \times 10^{-4}} \sim 90 \quad (5.18)$$

Since $N_{H\text{warm}} \sim 1 \times 10^{22} \text{ cm}^{-2}$, $N_{H\text{hot}} \sim 9 \times 10^{23} \text{ cm}^{-2}$. Taking equation 5.3, $\xi_{\text{warm}} \sim 10^{2.4}$, $\xi_{\text{hot}} \gtrsim 10^{4.5}$ and assuming that the density is the same in both regions (i.e. $n_{\text{hot}} = n_{\text{warm}} = 10^8 \text{ cm}^{-3}$) gives $r_{\text{hot}} \sim 5 \times 10^{15} \left(\frac{L_{44}}{\xi_{4.5} n_8} \right)^{1/2} \text{ cm} \sim 3 \times 10^{15} \text{ cm}$ and $r_{\text{warm}} \sim 5 \times 10^{16} \left(\frac{L_{44}}{\xi_{2.5} n_8} \right)^{1/2} \text{ cm} \sim 3 \times 10^{16} \text{ cm}$. The thickness of both regions can also be calculated from $\Delta r = \frac{N_H}{n}$ giving $\Delta r_{\text{hot}} \sim 9 \times 10^{15} \text{ cm}$ and $\Delta r_{\text{warm}} \sim 1 \times 10^{14} \text{ cm}$. Interestingly, from a statistical investigation using the number ratio of Seyfert 2 galaxies with and without a hidden broad line region, Taniguchi & Anabuki (1999) derived a location for the electron scattering region of between $\sim 3 \times 10^{16} - 3 \times 10^{17} \text{ cm}$ from the central engine.

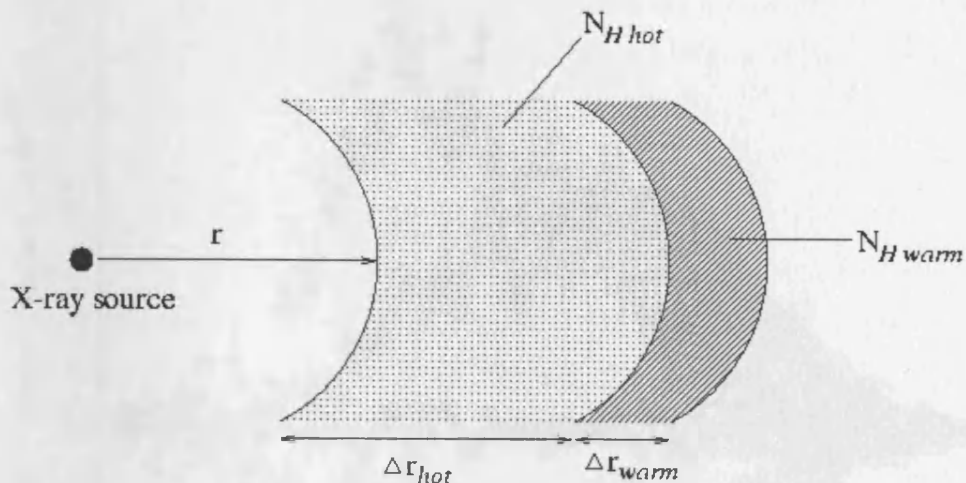


Figure 5.11: A model consisting of two separate regions, a hot fully ionized inner region and a cooler outer region.

As can be seen from Table 5.2, Model 6 gives a better fit to the ASCA data of NGC 4151 than Model 5. The improvement in χ^2 comes about from the slight difference in the description of the data below 1 keV. The major distinction between the two models is that the power-law which contributes significantly to the soft flux is absorbed by low column density gas ($N_H \sim 3 \times 10^{21} \text{ cm}^{-2}$) in Model 6. This results in slightly more line-like emission being required at energies below 0.9 keV hence the increase in the column density of the photoionized gas. The fact that the soft power-law continuum in Model 6 is absorbed brings about the question whether it is in actual fact a small fraction of the intrinsic X-ray source that is very weakly absorbed. Scattered flux would not be expected to vary on time-scales of a couple of years, therefore a comparison of Model 6 with SIS-0 data during PV1, PV2 and AO1 observations of NGC 4151 might provide more information on the origin of this soft emission. The residuals of all four datasets, when compared to Model 6, are shown in Figure 5.12. All of the data below 1 keV agrees with Model 6 to within ~ 10 percent and are therefore consistent with the conjecture that this emission is from an extended photoionized region. The scatter power-law in Model 6, however, dominates the X-ray spectrum up to ~ 1.5 keV. If the scattered emission does not vary on the time-scales between these observations the soft flux would not be expected to drop below this minimum scattered emission level. PV2 and AO1 observations are in agreement with this hypothesis but PV1 data is consistently below the scattered emission model between 1-1.5

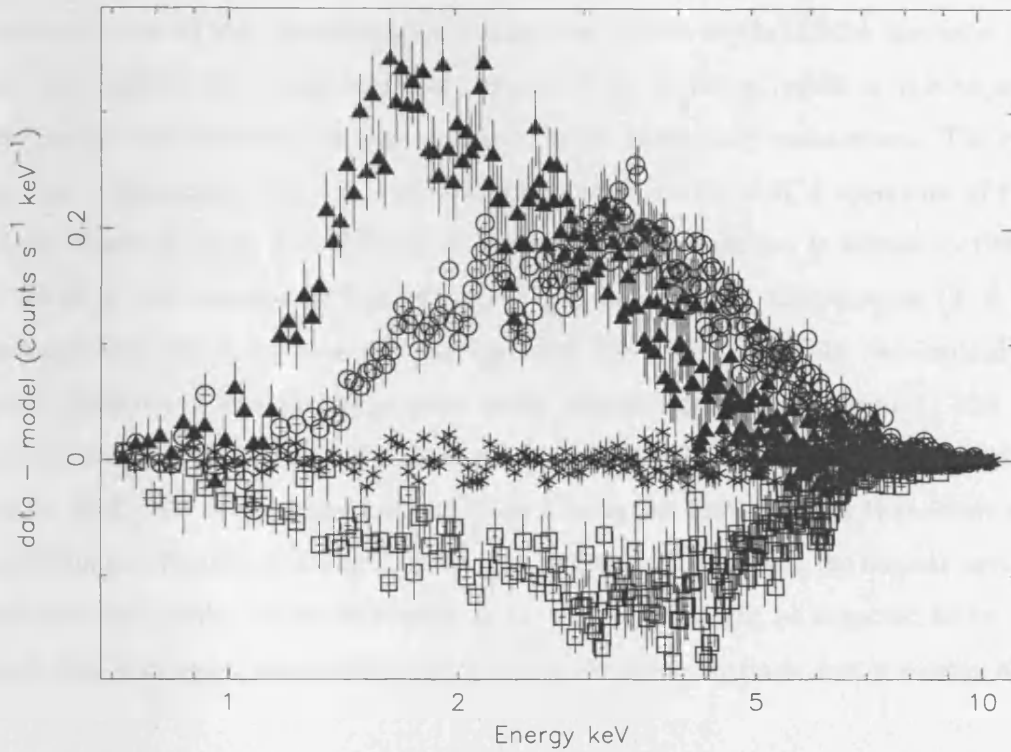


Figure 5.12: Residuals for PV1 (open squares), PV2 (filled triangles), AO1 (open circles) and AO4 (stars) data when compared to Model 6.

keV. This might indicate that emission in this band is due to leakage of direct flux. The other possibility is, of course, that it is flux from a scattering region situated close enough to the central source that the line-of-sight to it is intercepted by the outer boundaries of the obscuring region. Such a region would also respond to changes in the hard continuum in relatively short time-scales. It should also be noted here that the current analysis assumes the hard power-law continuum extrapolates into the soft band (hence the reason for tying the slopes of the intrinsic and scattered power-law components) and that all other features observed in the soft X-ray band arise in the scattering medium as intrinsic emission. It is also possible that some features could be emission from the central engine itself which is then scattered into the line-of-sight in a similar manner to the hard continuum. Indeed a recent paper by Vaughan *et al.* (1999) on the narrow-line Seyfert 1 galaxy Ark 564 reports possible evidence for reflection from an ionized disk which might also produce a strong O VIII RRC (Ross, Fabian & Young 1999). However, because of the quality of the data from current X-ray satellites and the very complex nature of NGC 4151, further investigations along these lines is not warranted.

The detection of an O VIII recombination continuum feature in the *ASCA* spectrum of NGC 4151 not only allowed the temperature of the soft X-ray emitting region in this object to be measured simply and directly but also enabled it to be reasonably constrained. The radiative recombination continuum of S XVI was recently detected in the *ASCA* spectrum of the High Mass X-ray Binary Cygnus X-3 (Liedahl & Paerels 1996; Kawashima & Kitamoto 1996). The narrow shape of this continuum feature, implying a low electron temperature ($T \lesssim 4 \times 10^5$ K), confirmed that the X-ray line-emitting region in this object is highly over-ionized relative to coronal equilibrium and therefore must be in photoionization equilibrium. The analysis presented here also confirms the very similar nature of the central region in the Seyfert galaxy NGC 4151. NGC 4151 is the second object (Mrk 3 being the first) thus far that shows evidence for a recombination feature at 0.9 keV. According to the Unified scheme the nuclear environment in Seyfert are very similar, if this is correct an O VIII feature might be expected to be observed in other Seyfert 2 galaxies, especially those in which the direct intrinsic flux is heavily absorbed.

5.5 Soft X-ray features in Seyfert 2 galaxies

Soft X-ray emission features from a partially ionized plasma, similar to those observed in the spectra of NGC 4151 (previous section) and Mrk 3 (Chapter 3) might be expected in the sample of Seyfert 2 galaxies analysed in Chapter 4. As was the case for Mrk 3, the hard continuum in all of these objects does not contribute to the soft X-ray flux because of heavy absorption and the bulk of the soft flux may be interpreted as nuclear emission scattered into the line-of-sight. Non-simultaneous *ASCA* SIS and *Ginga* data have been used to investigate such possibilities, with the SIS-0 and SIS-1 data combined in order to improve the signal-to-noise ratio of these relatively weak soft X-ray sources. The preferred cut-off continuum plus scattered power-law description (i.e. Model 3a,b,c or d; see § 4.2.3) for the hard X-ray spectrum of each object was taken and compared to SIS data below 1.5 keV down to 0.6 keV. Excess emission below 1 keV was present in two out of the five Seyfert 2 galaxies discussed in chapter 4 namely, Mrk 348 and NGC 4507. In addition to these two objects NGC 7582 also shows evidence for a sharp feature in the *ASCA* spectrum (see Figure 5.13). Unfortunately the *Ginga* spectrum of this object is contaminated by emission from the cluster Sersic 159-03 (Charles & Phillips 1982) and is, therefore, not used here. Warwick *et al.* (1993) did attempt to analyse the *Ginga* spectrum of NGC 7582 by including a thermal bremsstrahlung component to account for the cluster emission.

They found that a fixed spectral slope of $\alpha = 0.7$ was a reasonable assumption and consistent with the value inferred from HEAO-1/A2 observations (Mushotzky 1982). Thus when fitting the ASCA spectrum of NGC 7582 the slope is also fixed at this value.

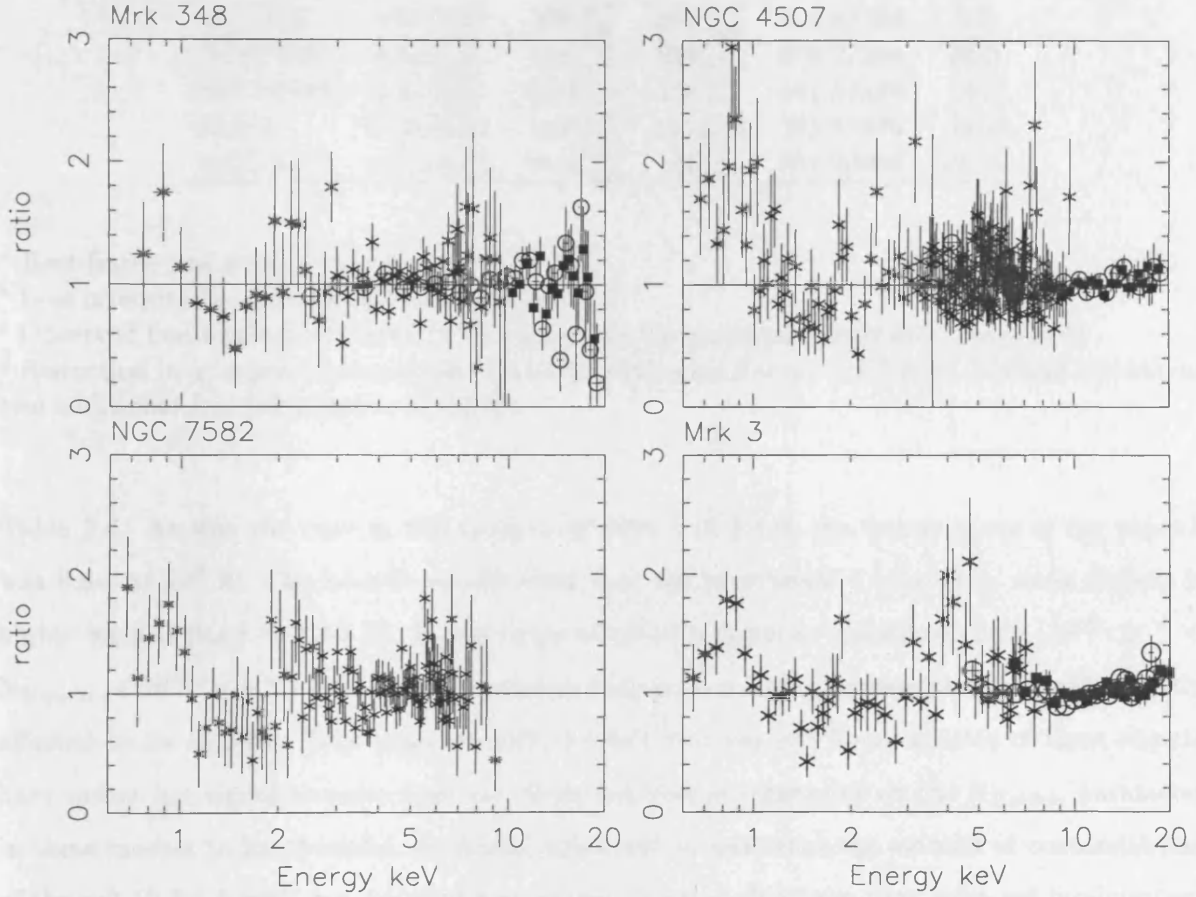


Figure 5.13: Ratio plot of the data compared the ‘scatter power-law’ model for each object. The data points correspond to *Ginga* top-layer (open circles), *Ginga* mid-layer (filled squares) and combined ASCA SIS0+SIS1 (stars).

The features in these three objects can be parameterised by adding a narrow gaussian at ~ 0.9 keV. The best-fitting line energy E_{ga} (in the source’s rest frame) and intensity A_{ga} plus its equivalent width with respect to the scattered continuum are listed in Table 5.3. For comparison, the corresponding values for Mrk 3 and NGC 4151 (AO4 only) are also shown. A range of equivalent widths $EW \sim 60\text{--}280$ eV are observed. It is striking how consistent the best-fit line energies are with each other and suggests that the same physical process is responsible for the 0.9 keV features in all of the sources. The results of replacing the gaussian component with the same photoionization model that was used for NGC 4151 (i.e. in Model 4) are given in

Table 5.3: Parameterisation of the 0.9 keV feature in Seyfert 2 galaxies.

Name	E_{ga}^a	A_{ga}^b	EW^c	χ^2/dof	$\Delta\chi^2{}^d$
Mrk 348	$0.91^{+0.06}_{-0.09}$	$0.8^{+0.7}_{-0.6}$	202^{+167}_{-146}	114.8/100	5.3
NGC 4507	$0.89^{+0.01}_{-0.02}$	$3.8^{+1.2}_{-1.0}$	280^{+87}_{-73}	273.2/254	38.5
NGC 7582	$0.93^{+0.05}_{-0.06}$	3.2 ± 1.5	195^{+93}_{-91}	141.3/109	14.2
Mrk 3	0.88 ± 0.01	$4.9^{+0.9}_{-1.0}$	135 ± 36	501.8/376	79.2
NGC 4151	0.89 ± 0.01	$10.5^{+1.6}_{-1.4}$	60^{+9}_{-8}	761.0/606	171.6

^a Rest-frame line energy in keV

^b Line intensity in units of 10^{-5} photons $\text{cm}^{-2} \text{s}^{-1}$

^c Observed line equivalent width (with respect to the scattered power-law continuum)

^d Reduction in χ^2 upon the inclusion of a narrow gaussian line at ~ 0.9 keV. The line introduces two additional free parameters to the fit.

Table 5.4. As was the case in the analysis of Mrk 3 (§ 3.3.3) the temperature of the plasma was fixed at 10^6 K. The best-fit results infer that the photoionized plasma in these objects is highly ionized ($\log \xi \sim 3.3\text{--}3.7$). In the range of column densities considered here ($10^{22} \text{ cm}^{-2} < N_{H\text{warm}} < 10^{23.6} \text{ cm}^{-2}$) the intrinsic emission from such a highly ionized plasma is only slightly affected by its column. This together with the fact that the soft X-ray spectra of these objects have rather low signal-to-noise does not allow any sort of constraint on the $N_{H\text{warm}}$ parameter in these models to be obtained. It is also important to note that the amount of contamination of the soft (0.5–4.5 keV) flux by starburst emission², estimated from their infra-red luminosities, for Mrk 348, NGC 4507 and NGC 7582 are 5, 75 and 34 percent respectively, which is, in the case of NGC 4507 and NGC 7582, significantly greater than for Mrk 3 and NGC 4151.

Evidence for a narrow feature at 0.9 keV in the ASCA spectrum of NGC 4507 was first reported by Comastri *et al.* (1998). These authors attribute the feature to a K_{α} transition in helium-like Neon resulting in a line at a rest energy of 0.92 ± 0.02 keV. In this case O VIII recombination at 0.87 keV is formally inconsistent (at the 3σ level) with the observed line energy. However, as is shown from the above analysis, Comastri *et al.* (1998) note that in a 10^6 K plasma, the broadening of the O VIII feature would have the effect of shifting the centroid to higher energy and therefore could be made consistent with the NGC 4507 observations. The ASCA data of these objects, although of not good enough quality to confirm the presence of O VIII RRC at

² values taken from Turner *et al.* (1997a).

Table 5.4: The best-fit ionization parameter and column density of the photoionized gas.

Name	$\log\xi$	$N_{H_{warm}}^a$	χ^2/dof
Mrk 348	$3.7^{+0.6}_{-0.4}$	$0.4^{+3.6*}_{-0.3**}$	112.8/100
NGC 4507	$3.3^{+0.07}_{-0.08}$	$4.0^{+0.0*}_{-0.8}$	268.8/254
NGC 7582	$3.5^{+0.3}_{-0.2}$	$4.0^{+0.0*}_{-3.9**}$	133.2/109

^a 10^{23} cm^{-2} .

* reached upper limit of model.

** reached lower limit of model.

0.9 keV do provide promising results that such a feature could be a common phenomenon in the soft X-ray spectra of Seyfert 2 galaxies.

Chapter 6

Future Prospects with *XMM*

The next generation of X-ray satellites to be launched over the next couple of years will have hugely improved capabilities compared to current and previous X-ray missions. These are the X-ray Multi Mirror (*XMM*) observatory, a cornerstone mission of the European Space Agency's (ESA) Horizon 2000 programme, Chandra (previously known as AXAF) and ASTRO-E. This chapter briefly discusses the instruments on-board these observatories and their salient properties and then focuses on *XMM* and how it might be utilized to further the investigations carried out in this thesis. It is certainly possible that several of the scientific uncertainties surfaced in the current study will be resolved by *XMM* observations.

6.1 *XMM*

XMM is scheduled to be launched on December 10th 1999 into a highly elliptical orbit, with an apogee and perigee of $\sim 114,000$ km and 7000 km respectively, enabling targets to be observed continuously for up to ~ 70 ks. The *XMM* observatory consists of three identical, co-aligned Wolter type-1 X-ray telescopes that focus light onto three X-ray CCD cameras (EPIC) and two Reflection Grating Spectrometer (RGS units), plus a 30-cm optical/UV telescope. There are two types of EPIC cameras, one EPIC pn and two EPIC MOS. The EPIC MOS cameras do not receive all of the X-rays collected by the telescopes. These two telescopes are also equipped with an RGS each. The RGS consists of a Reflection Grating Assembly (RGA), located in the telescope light path that disperses ≈ 50 percent of the radiation onto a strip of CCDs, the RGS Focal

Cameras. The effective area of the X-ray telescopes combined with the quantum efficiency of the EPIC cameras is comparable to that of non-imaging satellites such as *Ginga* and XTE (Figure 6.1). However the EPIC instruments also offer higher resolution spectroscopy and imaging capabilities (HPD ~ 15 arcsec) that, because of the lower background, make them considerably more sensitive. In addition all of the instruments on-board *XMM* operate simultaneously and will therefore provide huge amounts of data, allow concurrent X-ray and optical/UV monitoring of X-ray sources and facilitate the identification of sources in the field of view. In the next sections the properties and characteristics of individual X-ray instruments on-board *XMM* are briefly discussed, for a full description see the *XMM Users' Handbook* (Dahlem 1999).

6.1.1 EPIC

The EPIC pn detector has a field of view of ~ 30 arcmin and consists of 12 pn CCDs, each 13.6×4.4 arcmin, arranged in two rows of six chips. The EPIC MOS instruments also have a field of view of ~ 30 arcmin. The 7 MOS CCDs, with dimensions 10.9×10.9 arcmin each, are arranged so that the central chip is surrounded by the other six. The spectral coverage of all three EPIC cameras is between 0.1-15 keV. The pn detector is, however, more sensitive than the MOS detectors because of its superior quantum efficiency (the pn CCDs are back-illuminated, providing greater low energy response) and the fact that the effective area of the MOS are affected by the presence of the gratings. The angular resolution of both the EPIC pn and MOS instruments is determined by the point spread function (PSF) of the mirrors (Half Power Diameter (HPD) ~ 15 arcsec at 1.5 keV) and is about twice as good as the *ROSAT* PSPC. The spectral resolution of both the pn and MOS are also similar and comparable to that of the SIS detectors on-board *ASCA* when it was first launched (FWHM ~ 130 eV at 6.4 keV).

6.1.2 RGS

The RGS is sensitive between 0.35-2.5 keV with an effective area for one RGS (1st order) of ~ 70 cm² at 1 keV, a factor of three smaller than the *ROSAT* PSPC. The RGS Focal Cameras, which detect X-rays reflected by the RGA, consists of 9 MOS CCD chips located along the dispersion direction of the RGA. The RGS will, for the first time ever, provide high resolution X-ray spectroscopy (1st order FWHM ~ 6 eV at 1 keV), however its low effective area will

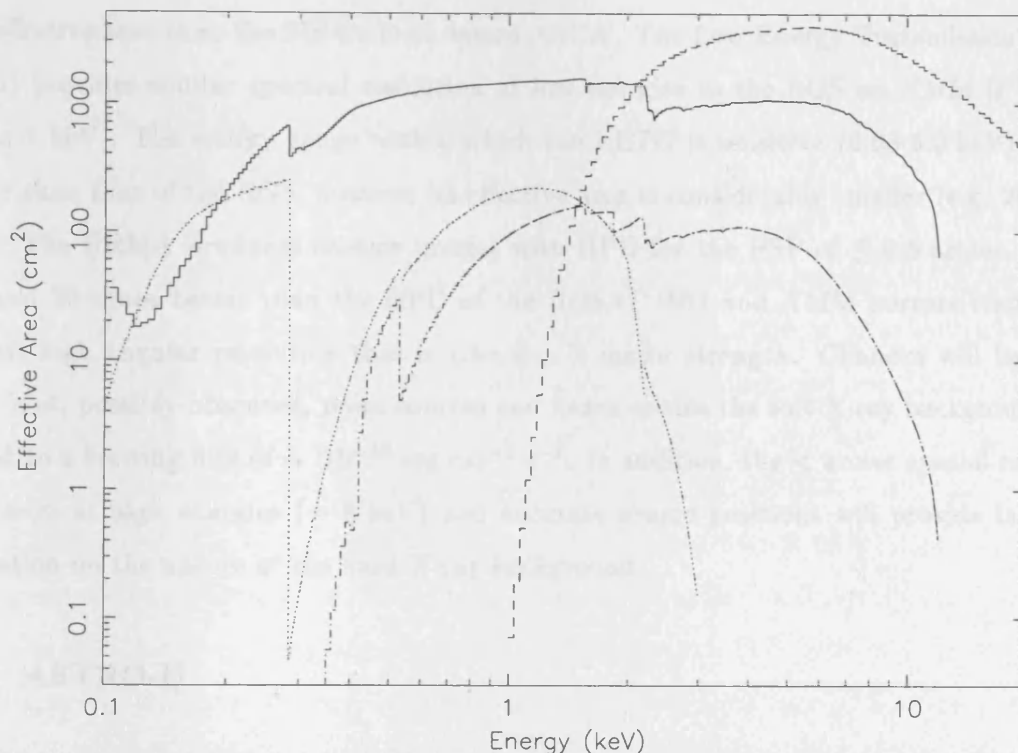


Figure 6.1: The effective area of various instruments between 0.1-20.0 keV: EPIC pn (solid curve), *Ginga* (dashed curve), ASCA SIS (dash-dot curve) and ROSAT PSPC (dot curve).

prohibit the full energy resolution from being utilised for all but the brightest AGN and longest exposure times.

6.1.3 Chandra

Chandra was launched on July 23rd 1999 and is the third of NASA's Great Observatories. The *Chandra* observatory consists of a High Resolution Mirror Assembly (HRMA) that focuses X-rays onto one of four focal plane detectors, two AXAF CCD Imaging Spectrometers (ACIS-I and ACIS-S) and two microchannel plate detectors called the High Resolution Cameras (HRC-I and HRC-S). In addition two transmission gratings can be placed to intersect the HRMA X-ray beam which, when used in conjunction with either the ACIS-S or HRC-S, will provide high resolution spectroscopy between 0.08-10.0 keV. The High Energy Transmission Grating (HETG) is sensitive between 0.5-10.0 and yields a spectral resolution (FWHM ~ 50 eV at 6.4 keV) that is ≈ 3 times better than that obtained via normal CCD spectroscopy but, unfortunately, has a

lower effective area than the SIS CCD on-board ASCA . The Low Energy Transmission Grating (LETG) provides similar spectral resolution at low energies to the RGS on *XMM* (FWHM ~ 5 eV at 1 keV). The energy range within which the LETG is sensitive (0.08-6.0 keV) is much broader than that of the RGS, however its effective area is considerably smaller (e.g. 25 cm² at 1 keV). The HRMA produces on-axis images with HPD for the PSF of $\lesssim 0.5$ arcsec, a factor of 10 and 30 times better than the HPD of the *ROSAT* HRI and *XMM* mirrors respectively. It is this high angular resolution that is *Chandra* 's major strength. *Chandra* will be able to detect faint, possibly obscured, point sources and hence enable the soft X-ray background to be resolved to a limiting flux of $\sim 10^{-16}$ erg cm⁻² s⁻¹. In addition, the $< \text{arcsec}$ spatial resolution of *Chandra* at high energies (~ 8 keV) and accurate source positions will provide invaluable information on the nature of the hard X-ray background.

6.1.4 ASTRO-E

ASTRO-E will be the fifth Japanese X-ray astronomy satellite and has a planned launch date of January 24th 2000. It consists of three types of co-aligned scientific instrument, the X-ray Spectrometer (XRS), four X-ray Imaging Spectrometers (XIS) and the Hard X-ray Detector (HXD). All five of the X-ray telescopes that focus light onto the XRS and XISs are similar to those on ASCA in that they have conical foil mirrors but with improved angular resolution (HPD ~ 2 arcmin). This, however, is still much poorer than the resolution of either *Chandra* or *XMM* . The primary instrument on-board *ASTRO-E* is the XRS. It is a cryogenically cooled calorimeter and therefore has a limited lifespan of approximately 2 years. The XRS and XISs are sensitive between 0.4-12.0 keV. The XRS provides high spectral resolution (FWHM ~ 10 eV across the whole band), comparable to that obtained with the RGS on *XMM* and the LETG on *Chandra* . The advantage that the XRS has over these instruments is its broad energy range and relatively high effective area (~ 200 cm² at 1 and 6.4 keV). Each XIS has a similar spectral resolution to the EPIC cameras on-board *XMM* but much poorer spatial resolution and lower effective area (e.g. ~ 200 cm² at 6.4 keV compared to 900 cm² for the EPIC pn). The HXD is a non imaging instrument, has an energy range between 10-600 keV and will be more sensitive than any other current or past mission in the energy range from a few tens to several hundred keV.

6.2 Future Work with *XMM*

6.2.1 Is O VIII recombination a prominent feature in the soft X-ray spectrum of Seyfert 2 galaxies?

The feature at ~ 0.9 keV in the soft X-ray spectrum of Mrk 3 was represented in § 3.3.3 as either thermal emission, possibly from a starburst component (Model 4, Table 3.3), or intrinsic emission from a partially ionized plasma (Model 5, Table 3.3). Even though the photoionization model was the preferred description, it is not possible to discriminate, with any certainty, between the two models with the currently available data. Evidence for an O VIII RRC in the soft X-ray spectrum of NGC 4151 is considerably stronger than for Mrk 3 since a thermal emission component, consisting of Fe-L and Ne-K line blends cannot satisfactorily account for the narrow feature observed in the very high signal-to-noise *ASCA* spectrum (§ 5.3). In addition to these two objects, the Seyfert 2 galaxies Mrk 348, NGC 4507 and NGC 7582 (see § 5.5) show evidence for a feature at 0.9 keV (although considerably weaker). The detection of an O VIII recombination continuum in these galaxies would confirm the hypothesis that scattering is the dominant process giving rise to the excess flux which characterises the soft X-ray spectra of Seyfert 2 galaxies and provide a useful diagnostic of the physical state (i.e. temperature) of this medium. In the case of Mrk 3, the high resolution reflection grating on *XMM* will enable the two competing models, mentioned above, to be easily distinguished (see Figure 6.2). Both models predict a strong O VIII Ly α line at 0.65 keV. The grating is able to resolve emission between 0.7-1.0 keV as Ne IX K α and Fe XVII-XX L line transitions from the thermal plasma which is totally different to the O VIII radiative recombination continuum expected from a photoionized plasma. Even for the weaker Seyfert 2s, the high throughput of *XMM* will provide excellent signal-to-noise EPIC spectra, for reasonable exposure times (~ 40 ks), making it possible to carry out a detailed study of whether the *XSTAR* photoionization models better match the EPIC data than other plausible alternatives such as emission produced in an optically thin coronal plasma.

6.2.2 What is the temperature of the photoionized scattering medium?

The analysis of a deep (~ 100 ks) *ASCA* observation of NGC 4151 has shown that the sharp feature at 0.9 keV, similar to that observed for Mrk 3, in the soft X-ray spectrum of this object

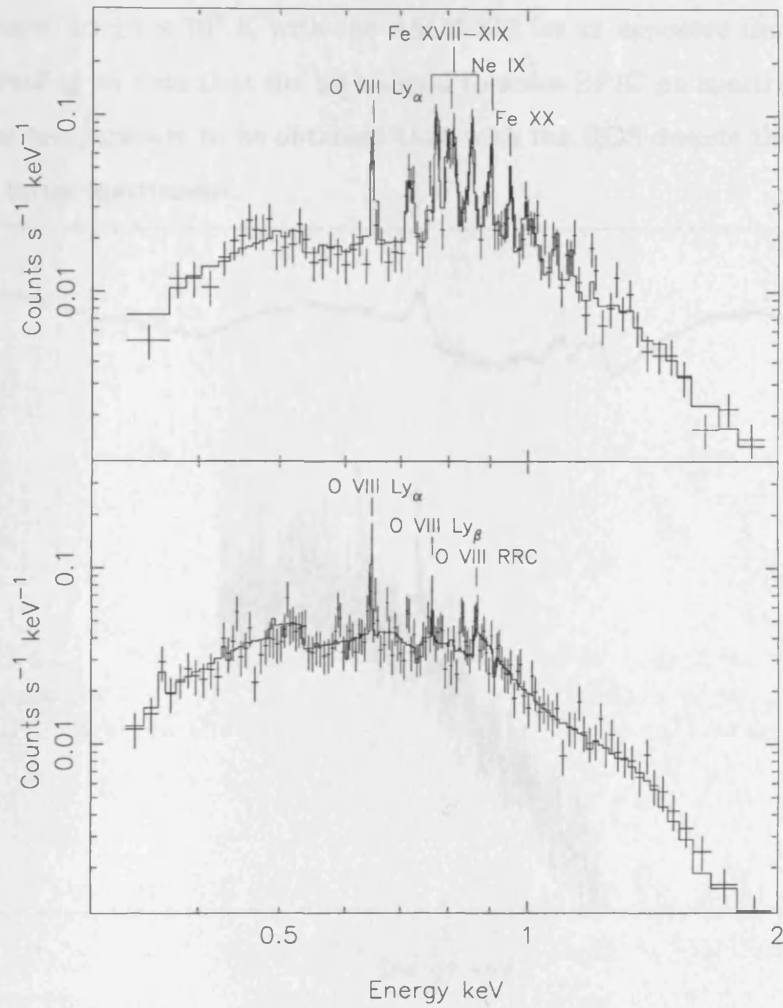


Figure 6.2: A 100 ks simulated RGS spectrum for Mrk 3 using either a scattered power-law continuum plus a Raymond-Smith thermal plasma component (Model 4; § 3.3.3) or scattered plus intrinsic emission from a photoionized plasma (Model 5; § 3.3.3).

is due to the radiative recombination of O VIII in a photoionized plasma. The intrinsic width of the feature is a result of the Maxwellian velocity distribution of the electrons in the plasma and hence reflects the electron temperature. EPIC pn and RGS simulations for NGC 4151 are shown in Figure 6.3 using Model 4 of § 5.3. Note the excellent signal-to-noise obtained for the pn spectrum. Although this model is not the preferred description of the soft X-ray spectrum of NGC 4151 (see Table 5.2) it is useful for the present purpose. The change in the best-fit χ^2 residuals with electron temperature for both EPIC pn and RGS data is shown in Figure 6.4. It demonstrates that within the constraints of the photoionized scatterer model, for a 40 ks exposure the plasma temperature can be measured to within $\pm 3 \times 10^4$ K with the EPIC pn

instrument compared to $\pm 1 \times 10^5$ K with the *ASCA* SIS for an exposure time that is 2.5 times longer. It is interesting to note that the high signal-to-noise EPIC pn spectrum enables tighter constraints on the temperature to be obtained than with the RGS despite the superior spectral resolution of the latter instrument.

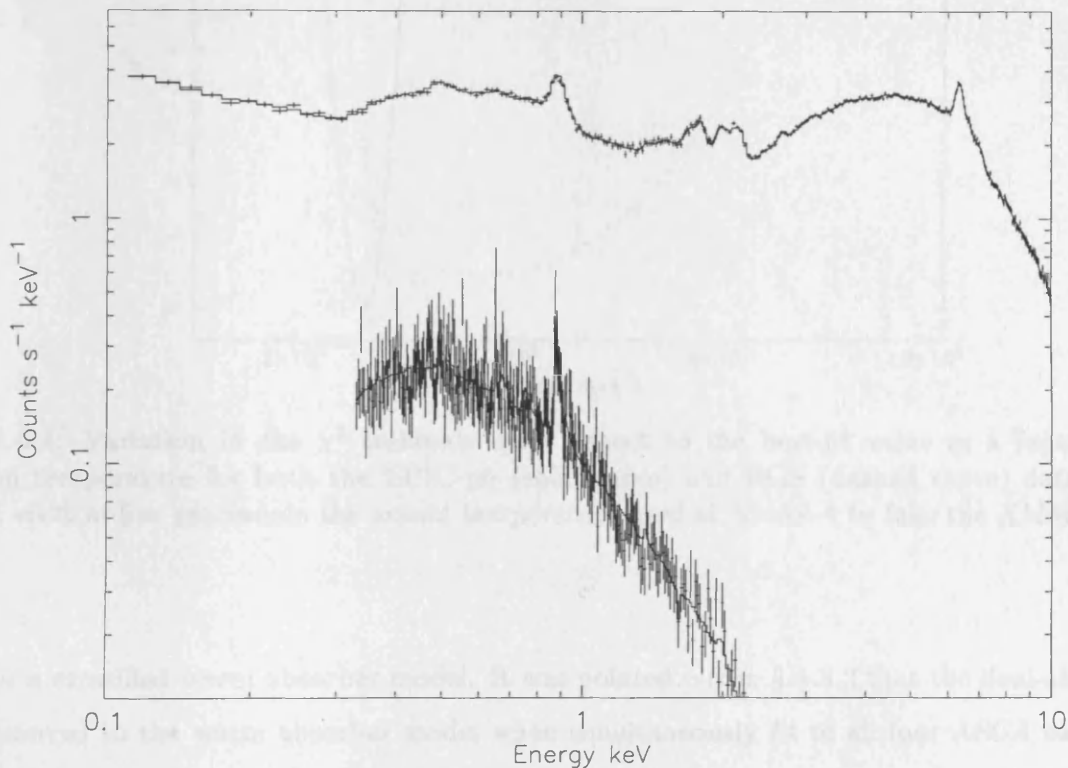


Figure 6.3: 40 ks EPIC pn and RGS simulations for NGC 4151. See text for details of model.

The temperature of the photoionized plasma used to describe the soft X-ray spectrum of Mrk 3 was assumed to be 10^6 K and was found to give a better fit than plasma temperatures of either $10^{5.5}$ K or 10^5 K. Optical data, however, implies that the temperature of the electron scattering region is less than 4×10^5 K (Tran 1995). Confirmation of an electron temperature of 10^6 K via *XMM* observations will, therefore, probably require the scattering region in Mrk 3 to be thermally stratified.

6.2.3 The nature of the complex absorption in NGC 4151.

In § 4.3 the complex absorption in NGC 4151 was represented by either a partial covering model (with up to 3 partially covering absorbers, although the dual-absorber model is used

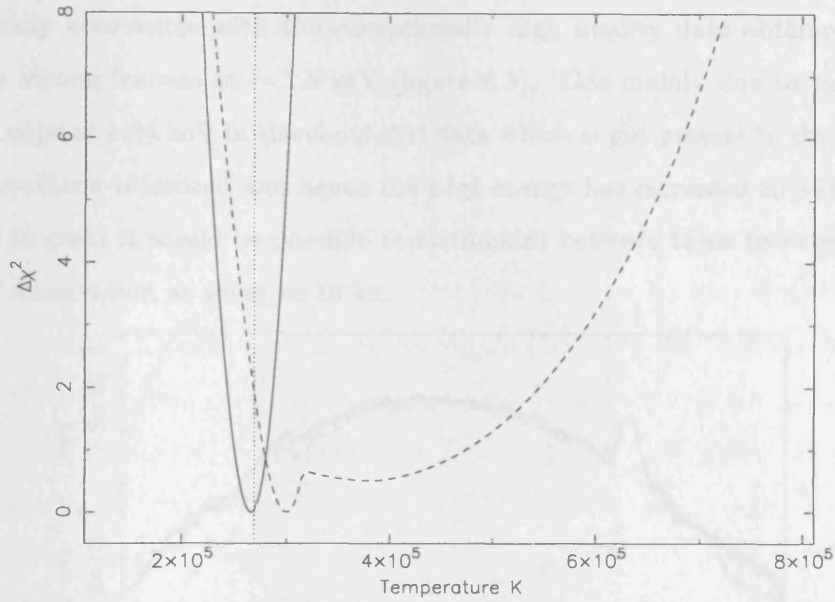


Figure 6.4: Variation in the χ^2 residuals with respect to the best-fit value as a function of electron temperature for both the EPIC-pn (solid curve) and RGS (dashed curve) data. The dotted vertical line represents the actual temperature used in Model 4 to fake the XMM data.

here) or a stratified warm absorber model. It was pointed out in § 4.3.2 that the dual-absorber was preferred to the warm absorber model when simultaneously fit to all four *ASCA* datasets. When *Ginga* observed NGC 4151 (Yaqoob *et al.* 1993) during a very bright state, although the spectrum softened, which is indicative of a change in the observed line-of-sight gas column density, there was no corresponding decline in the observed optical depth of the iron K-edge. There was, however, an increase in the edge energy, hinting at the possible presence of a warm absorber in the line-of-sight. Indeed for the *ASCA* AO1 data, when the observed hard (4-10 keV) flux of NGC 4151 was at its brightest state out of the four observations (see Figure 4.6), both the warm absorber and dual-absorber model give very similar χ^2 fits. Here the best-fit dual-absorber model to the AO1 data has been used to create a faked EPIC pn spectrum which is then fitted with the warm-absorber model. The ratio of the data to the model is shown in Figure 6.5 (bottom panel). As is obvious from the figure, these two models will be easily discriminated with XMM data. The main difference is in the shape and energy of the iron K-edge. The gas in the dual-absorber is cold and hence produces a sharp K-edge at an energy of 7.1 keV due to absorption by neutral iron atoms. The iron in the warm absorber model has a range of ionization states (Fe V-XXIII) resulting in a broad K-edge between ~ 7.3 -8.5 keV. This

difference is easily observable with the exceptionally high quality data obtained with *XMM*. There is also a strong feature at ~ 1.8 keV (figure 6.5). This mainly due to the presence of a neutral silicon edge at 1.84 keV in the simulated data which is not present in the warm-absorber model since the silicon is ionized and hence the edge energy has increased to ~ 1.95 keV. These differences are so great it would be possible to distinguish between these two competing models with an *XMM* observation as short as 10 ks.

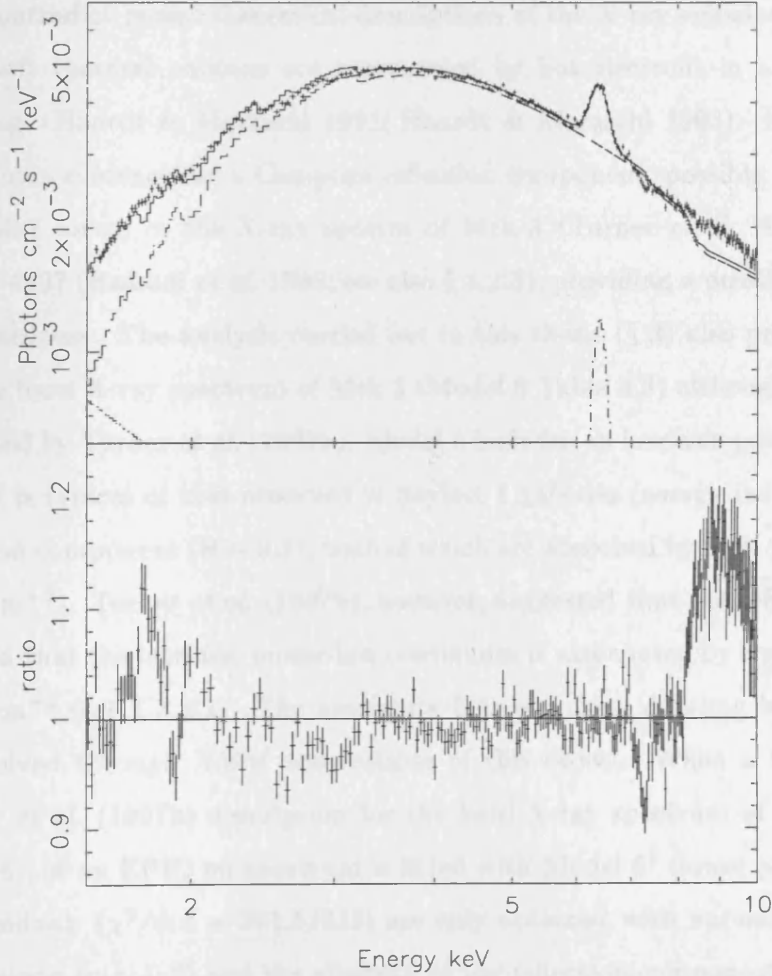


Figure 6.5: Top panel: The unfolded EPIC pn spectrum of NGC 4151 between 1.5-10.0 keV (created from the dual-absorber model) and the corresponding best-fit description using the warm-absorber model. Bottom panel: The ratio of the data to the model.

6.2.4 The hard X-ray spectrum of Seyfert 2 galaxies.

Although there is evidence that Seyfert 2 galaxies have intrinsic hard power-law slopes similar to the typical range ($\alpha \sim 0.9-1.0$) observed for Seyfert 1s (Smith & Done 1996) there are some exceptions. NGC 5252 (Cappi *et al.* 1996), Mrk 3 (Awaki *et al.* 1990) and NGC 4507 (Smith & Done 1996) have observed spectral indices that are flatter than the canonical value for Seyfert 1s and seem to contradict recent theoretical descriptions of the X-ray emission from radio-quiet AGN in which soft thermal photons are reprocessed by hot electrons in a corona above an accretion disk (e.g. Haardt & Maraschi 1991; Haardt & Maraschi 1993). More recent work, however, have shown evidence for a Compton reflection component, possibly from an accretion disk or a molecular torus, in the X-ray spectra of Mrk 3 (Turner *et al.* 1997b; Cappi *et al.* 1999a) and NGC 4507 (Bassani *et al.* 1998; see also § 4.2.3), providing a possible explanation for their apparent hardness. The analysis carried out in this thesis (§ 3) also provided a plausible description of the hard X-ray spectrum of Mrk 3 (Model 6 Table 3.3) although slightly different to the one proposed by Turner *et al.* (1997b). Model 6 includes an intrinsic power-law continuum with a slope that is typical of that observed in Seyfert 1 galaxies (energy index $\alpha \sim 0.8$) and a Compton reflection component ($R \sim 0.8$), both of which are absorbed by high column density gas ($N_H \sim 7 \times 10^{23} \text{ cm}^{-2}$). Turner *et al.* (1997b), however, suggested that the reflection component is unabsorbed and that the intrinsic power-law continuum is attenuated by a gas column density $N_H \approx 1 \times 10^{24} \text{ cm}^{-2}$ (see § 3.4.1). The ambiguity between these differing interpretations will definitely be resolved through *XMM* observations of this object. When a 100 ks simulation, using the Turner *et al.* (1997b) description for the hard X-ray spectrum of Mrk 3¹ (see upper panel of figure 6.6), of an EPIC pn spectrum is fitted with Model 6² (lower panel of figure 6.6), reasonable χ^2 residuals ($\chi^2/\text{dof} = 381.5/313$) are only obtained with unrealistic values for the hard continuum slope ($\alpha \sim 0.2$) and the strength of the reflection component ($R \sim 87$).

The intensity and profile of Fe K_α line emission can provide invaluable clues on the geometry and origin of the reprocessing region from where the iron emission emanates. Several of the objects analysed in this thesis show evidence of a broad iron line (e.g. Mrk 3, NGC 4151, ESO 103-G35 and possibly NGC 7172) that could possibly be a result of either additional line

¹Here the soft X-ray spectrum is characterised by a power-law component with a slope equivalent to that of the intrinsic continuum (i.e. $\alpha = 1.0$).

²Again this version of Model 6 has only a power-law to represent the soft flux.

components from highly ionized iron or doppler, gravitational and Compton scattering effects from an accretion disk. XMM EPIC observations will define the hard X-ray spectra of these sources with unprecedented precision. For Mrk 348, the weakest object in the sample, a 40 ks exposure will provide more than 15000 counts above 2 keV in the EPIC pn spectrum alone, enabling the structure of the Fe K_α /K-edge complex and the slope of the high energy continuum to be investigated in great detail. In addition, more accurate measurements of the form of the low-energy cut-off will provide tighter constraints on the line-of-sight gas column density to these heavily absorbed Seyfert 2 galaxies and therefore on possible column variability reported in several of these objects (see § 4.2.3). Indeed simulations for Mrk 348 and NGC 4507, using Model 3b (Table 4.6), have shown that a single EPIC pn spectrum (with a 40 ks exposure) provides better constraints on the spectral slope and column density in these objects than composite *Ginga* /*ASCA* data. This together with an accurate measurement of the Fe K-edge energy will provide a much deeper insight into the nature of the obscuring gas.

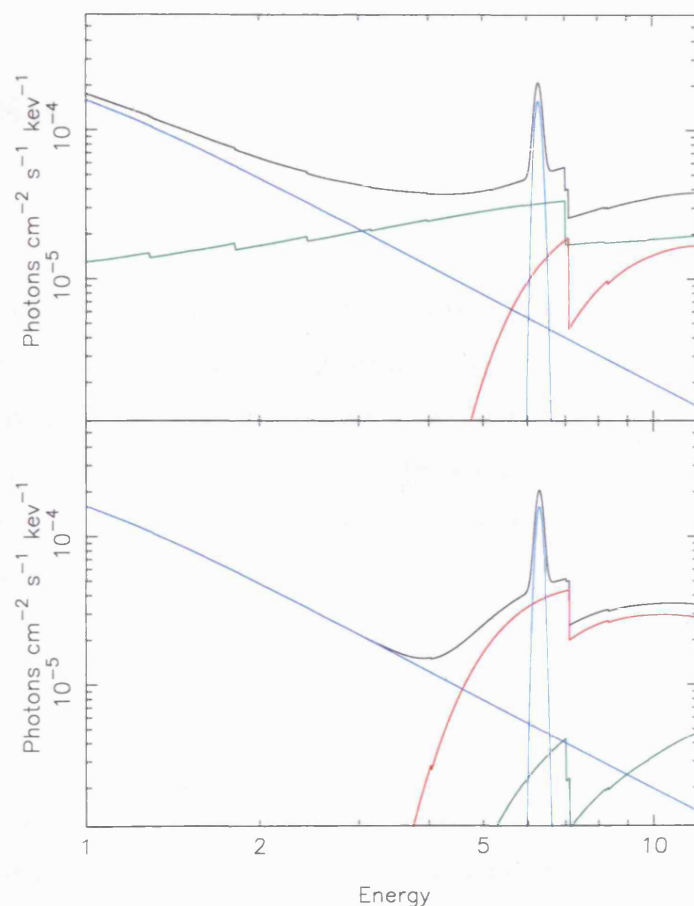


Figure 6.6: The competing descriptions of the hard X-ray spectrum of Mrk 3: the Turner *et al.* (1997b) model (upper panel) and Model 6 (lower panel). Both models consist of a heavily absorbed hard power-law (red curve), a reflection component (green curve), Fe K_{α} emission (light blue curve) and a soft power-law (dark blue curve).

Chapter 7

Conclusions

This thesis is concerned with the spectroscopic properties of heavily obscured Seyfert 2 galaxies and the Seyfert 1.9 NGC 4151 in the X-ray regime. Despite the obscuration that is present in these sources, X-ray observations, nevertheless, allow the inner regions to be probed directly and have provided a wealth of information about the geometry and physical state of the central engine and its surrounding environment. This chapter summarises the main conclusions of the work described in this thesis.

7.1 Mrk 3

(i) The broad-band 0.1–30 keV X-ray spectrum of Mrk 3 is rather stable with only the level of the hard X-ray continuum and the iron K_α line-flux showing clear evidence of variability on a time-scale of years.

(ii) The iron K_α line energy is consistent with neutral iron. A component of this line emission may originate in the fluorescence of an extensive cold gas distribution, which has a column density $N_H \sim 7 \times 10^{23} \text{ cm}^{-2}$ along our line of sight to the active nucleus; it is plausible that this gas is associated with a molecular torus in Mrk 3. Photoionization of the inner reaches of this medium may give rise to the “warm” absorption edge observed near 8 keV. The observed changes in the line equivalent width demonstrate that the iron line has a delayed response with respect to the continuum variations but, nevertheless, that iron-line reprocessing, possibly in an accretion disk, occurs within \sim a light-year of the active nucleus in Mrk 3.

(iii) The measured iron line width of $\sigma_{K\alpha} \approx 0.1$ keV provides a hint of underlying complexity in composition of the iron $K\alpha$ line, possibly similar to the situation in NGC 1068.

(iv) The inferred slope of the intrinsic hard X-ray continuum is model dependent with either a modest reflection component or the inclusion of an inner warm-absorber component both serving to steepen the derived spectral index. The continuum appears *not* to be anomalously flat compared to the norm for Seyfert 1 galaxies.

(v) The soft X-ray spectrum below ~ 3 keV is quite complex and may represent a blend of two or more separate components. A possible scenario is that the emission arises from the scattering of the nuclear continuum by a hot photoionized plasma which imprints both absorption and emission features on the emergent spectrum. In this setting the spectral feature present in the ASCA spectrum near 0.9 keV is identified with O VIII recombination.

7.2 The sample of Seyfert 2 galaxies

(i) The energy indices, α , of the hard power-law continuum derived for Mrk 348, ESO 103-G35, IC 5063 and NGC 7172 are consistent with those typically observed for Seyfert 1 galaxies, however the continuum slope of NGC 4507 is somewhat harder.

(ii) It has been shown that changes in the flux level of the hard X-ray continuum and the intensity of the iron $K\alpha$ line alone cannot account for the observed spectral variability that has occurred in three of the Seyfert 2 galaxies analysed in the sample of five (i.e. Mrk 348, NGC 4507 and NGC 7172) over time-scales of a few years between individual *Ginga* and ASCA observations of these objects. The preferred explanation for this variability seems to be a change, of between $1.4 \times 10^{22} \text{ cm}^{-2} - 9.4 \times 10^{23} \text{ cm}^{-2}$, in the gas column density that is situated in the line-of-sight to the central X-ray source, thus doubling the number of known Seyfert 2s that show N_H variability. Two possible causes of this column variability were considered, namely high column density gas clouds intersecting the line-of-sight to the central source and a reduction in the opacity of the absorbing gas due to photoionization.

(iii) The energy and EW of the Fe $K\alpha$ line in all five Seyfert 2 galaxies is consistent with a spherical distribution of cold gas surrounding the continuum source as a possible origin for the

emission as discussed by Leahy & Creighton (1993). However the EW for Mrk 348 and ESO 103-G35 remains constant while the intrinsic continuum varies by up to 60 percent and 17 percent respectively. In addition the iron line in ESO 103-G35 is broad and implies that the reprocessed emission, in this object at least, emanates from an accretion disk.

(iv) The addition of a Compton reflection component of significant strength provides a reasonable improvement in the spectral fit to four out of the five galaxies, the exception being Mrk 348. With the inclusion of reflection, the inferred slope of the intrinsic continuum in NGC 4507 increases significantly to within the range of values that are observed for Seyfert 1 galaxies.

(v) The soft X-ray spectrum of these sources is relatively weak, however, evidence for a sharp feature at ~ 0.9 keV, in the same mould as for Mrk 3 and NGC 4151, is found for Mrk 348, NGC 4507 and NGC 7582, a Seyfert 2 galaxy that wasn't considered in the initial sample.

7.3 NGC 4151

(i) Four *ASCA* observations of NGC 4151, taken over a period of approximately two years, demonstrate that the X-ray continuum of this object, in the 1-7 keV band, varies with time in a complicated manner. This change in spectral shape can only be explained as an effect of the absorption that is present in the spectrum of NGC 4151. A model in which the spectral variability is wholly due to the changing opacity of a single partially ionized cloud is ruled out. Two spectral models are able to reproduce the observed spectra fairly well, a model consisting of up to three partially covering absorbers with changes in both the column density and covering fraction accounting for the spectral variability and a stratified warm absorber model in which clouds of partially ionized gas move across the line-of-sight. The latter model is attractive since it doesn't require partial covering of the X-ray source however the former does provide a better description of the observed spectra.

(ii) Using the deepest (~ 100 ks) *ASCA* observation of NGC 4151 it was established that the sharp emission feature at 0.9 keV is due to the recombination of an electron directly into the ground state of fully ionized oxygen. This emission is thought to originate in gas that also scatters nuclear continuum into the line-of-sight, however, the rather low EW of this O VIII feature makes it difficult to physically explain all of the soft flux between 0.6-1.0 keV as emission from one

single partially ionized scattering region. This difficulty is resolved if a significant fraction of the flux is purely scattered emission from fully ionized gas with the cooler gas accounting for the remaining flux including the O VIII RRC. Two physical interpretations of this model were discussed; (1) small, high density warm clouds immersed in a highly ionized hot plasma and (2) two separate regions with the inner region being highly ionised and the cooler region situated further out from the X-ray source. The latter scenario was the preferred interpretation because of the unstable nature of the cooler gas in the former.

Clearly there is much to be learnt about Seyfert 2 type galaxies from X-ray spectral observations affording an appropriate combination of high spectral resolution, high sensitivity and broad-bandwidth coverage. As discussed in chapter 6, future missions such as *XMM*, *Chandra* and *ASTRO-E* will provide the essential tools required to further our knowledge on the Seyfert phenomenon.

References

- Alloin, D. *et al.*, 1995. **293**, 293.
- Antonucci, R. R. J. & Miller, J., 1985. *Astrophys. J.*, **297**, 621.
- Antonucci, R. R. J., 1993. *Ann. Rev. Astron. Astrophys.*, **31**, 473.
- Arnaud, K. A. *et al.*, 1985. *Mon. Not. R. astr. Soc.*, **217**, 105.
- Awaki, H., Koyama, K., Kunieda, H. & Tawara, Y., 1990. *Nature*, **346**, 544.
- Awaki, H., Koyama, K., Inoue, H. & Halpern, J. P., 1991. *Pub. Astr. Soc. Japan.*, **43**, 195.
- Band, D. L., Klein, R. I., Castor, J. I. & Nash, J. K., 1990. *Astrophys. J.*, **362**, 90.
- Barr, P. & Mushotzky, R. F., 1986. *Nature*, **320**, 421.
- Bassani, L. *et al.*, 1998. In: *Dal nano-al tera-eV: tutti i colori degli AGN*.
- Butcher, J. A. *et al.*, 1997. *Mon. Not. R. astr. Soc.*, **291**, 437.
- Capetti, A., Macchetto, F., Axon, D. J., Sparks, W. B. & Boksenberg, A., 1995. *Astrophys. J.*, **448**, 600.
- Cappi, M., Mihara, T., Matsuoka, M., Brinkmann, W., Prieto, M. A. & Palumbo, G. G. C., 1996. *Astrophys. J.*, **456**, 141.
- Cappi, M. *et al.*, 1999a. *Astr. Astrophys.*, **344**, 857.
- Cappi, M. *et al.*, 1999b. *advspr*, in press.
- Charles, P. A. & Phillips, M. M., 1982. *Mon. Not. R. astr. Soc.*, **200**, 263.
- Charles, P. A. & Seward, F. D., 1995. *Exploring the X-ray Universe*, Cambridge University Press.
- Comastri, A., Vignali, C., Cappi, M., Matt, G., Audano, R., Awaki, H. & Ueno, S., 1998. *Mon. Not. R. astr. Soc.*, **295**, 443.
- Czerny, B. & Elvis, M., 1987. *Astrophys. J.*, **321**, 305.
- XMM Users' Handbook*. 1999.

- David, L. P., Jones, C. & Forman, W., 1992. *Astrophys. J.*, **388**, 82.
- Done, C. & Fabian, A. C., 1989. *Mon. Not. R. astr. Soc.*, **240**, 81.
- Elvis, M., Matsuoka, M., Siemiginowska, A., Fiore, F., Mihara, T. & Brinkmann, W., 1994. *Astrophys. J. Letts.*, **436**, 55.
- Fabian, A. C., Rees, M. J., Stella, L. & White, N. E., 1989. *Mon. Not. R. astr. Soc.*, **238**, 729.
- Fabian, A. C. *et al.*, 1994. *Pub. Astr. Soc. Japan.*, **46**, L59.
- Fabian, A. C., 1994. *Astrophys. J. Suppl.*, **92**, 555.
- Fiore, F., Perola, G. C. & Romano, M., 1990. *Mon. Not. R. astr. Soc.*, **243**, 522.
- Ford, H. C. *et al.*, 1994. *Astrophys. J. Letts.*, **435**, 27.
- Georgantopoulos, I., Papadakis, I., Warwick, R. S., Smith, D. A., Stewart, G. C. & Griffiths, R. G., 1999. *Mon. Not. R. astr. Soc.*, submitted.
- George, I. M. & Fabian, A. C., 1991. *Mon. Not. R. astr. Soc.*, **249**, 352.
- George, I. M., Turner, T. J., Netzer, H., Nandra, K., Mushotzky, R. F. & Yaqoob, T., 1998. *Astrophys. J. Suppl.*, **114**, 73.
- Ghisellini, G., Haardt, F. & Matt, G., 1994. *Mon. Not. R. astr. Soc.*, **267**, 743.
- Grandi, P., Tagliaferri, G., Giommi, P., Barr, P. & Palumbo, G. G. C., 1992. *Astrophys. J. Suppl.*, **82**, 93.
- Griffiths, R. G., Warwick, R. S., Georgantopoulos, I., Done, C. & Smith, D. A., 1998. *Mon. Not. R. astr. Soc.*, **298**, 1159.
- Haardt, F. & Maraschi, L., 1991. *Astrophys. J. Letts.*, **380**, 51.
- Haardt, F. & Maraschi, L., 1993. *Astrophys. J.*, **413**, 507.
- Halpern, J. P., 1984. *Astrophys. J.*, **281**, 90.
- Harms, R. J. *et al.*, 1994. *Astrophys. J. Letts.*, **435**, 35.
- Hasinger, G., Turner, T. J., George, I. M. & Boese, G., 1992a. Technical Report, MPE and NASA/GSFC. CAL/ROS/92-001.

- Hasinger, G., Turner, T. J., George, I. M. & Boese, G., 1992b. Technical Report, MPE and NASA/GSFC. CAL/ROS/92-001a.
- Hayashida, K. *et al.*, 1989. *Pub. Astr. Soc. Japan.*, **41**, 373.
- Holt, S. S., Mushotzky, R. F., Becker, R. H., Boldt, E. A., Serlemitsos, P. J., Szymkowiak, A. E. & White, N. E., 1980. *Astrophys. J. Letts.*, **241**, 13.
- Iwasawa, K., Yaqoob, T., Awaki, H. & Ogasaka, Y., 1994. *Pub. Astr. Soc. Japan.*, **46**, L167.
- Iwasawa, K., Fabian, A. C. & Matt, G., 1997. *Mon. Not. R. astr. Soc.*, **289**, 443.
- Johnson, W. N. *et al.*, 1997. *Astrophys. J.*, **482**, 173.
- Kallman, T. R. & Krolik, J. H. *XSTAR : A Spectral Analysis Tool. Version 1.40 of the User's Guide.* 1997.
- Kallman, T. R. & McCray, R., 1982. *Astrophys. J. Suppl.*, **50**, 263.
- Kawashima, K. & Kitamoto, S., 1996. *Pub. Astr. Soc. Japan.*, **48**, L113.
- Kay, L., 1990. *PhD thesis*, University of California.
- Koyama, K., Inoue, H., Tanaka, Y., Awaki, H., Takano, S., Ohashi, T. & Matsuoka, M., 1989. *Pub. Astr. Soc. Japan.*, **41**, 731.
- Krolik, J. H. & Begelman, M. C., 1986. *Astrophys. J. Letts.*, **308**, 55.
- Krolik, J. H. & Kallman, T. R., 1987. *Astrophys. J. Letts.*, **320**, 5.
- Krolik, J. H. & Kriss, G. A., 1995. *Astrophys. J.*, **447**, 512.
- Krolik, J. H., Madau, P. & Życki, P. T., 1994. *Astrophys. J. Letts.*, **420**, 57.
- Krolik, J. H., McKee, C. . F. & Tarter, C. B., 1981. *Astrophys. J.*, **249**, 422.
- Lampton, M., Margon, B. & Bowyer, S., 1976. *Astrophys. J.*, **208**, 177.
- Laor, A., Netzer, H. & Piran, T., 1990. *Mon. Not. R. astr. Soc.*, **242**, 560.
- Laor, A., 1991. *Astrophys. J.*, **376**, 90.
- Leahy, D. A. & Creighton, J., 1993. *Mon. Not. R. astr. Soc.*, **263**, 314.

- Liedahl, D. A. & Paerels, F., 1996. *Astrophys. J. Letts.*, **468**, 33.
- Liedahl, D. A., Kahn, S. M., Osterheld, A. L. & Goldstein, W. H., 1990. *Astrophys. J. Letts.*, **350**, 37.
- Lightman, A. P. & White, T. R., 1988. *Astrophys. J.*, **335**, 57.
- Magdziarz, P. & Zdziarski, A. A., 1995. *Mon. Not. R. astr. Soc.*, **273**, 837.
- Makino, F. *et al.*, 1987. *Astrophys. Letters Commun.*, **25**, 223.
- Makishima, K. *et al.*, 1996. *Pub. Astr. Soc. Japan.*, **48**, 171.
- Makishima, K., 1986. In: *The Physics of Accretion onto Compact Objects*, Mason, K. O., Watson, M. G. & White, N. E., eds., Springer-Verlag, Berlin, p. 249.
- Malizia, A. *et al.*, 1997. *Astrophys. J. Suppl.*, **113**, 311.
- Malkan, M. A. & Sargent, W. L. W., 1982. *Astrophys. J.*, **254**, 22.
- Marshall, F. E. *et al.*, 1992. In: *Frontiers of Astrophysics*, Tanaka, Y. & Koyama, K., eds., Universal Academy Press, Tokyo, p. 233.
- Marshall, F. E. *et al.*, 1993. *Astrophys. J.*, **405**, 168.
- Matt, G., Brandt, W. N. & Fabian, A. C., 1996. *Mon. Not. R. astr. Soc.*, **280**, 823.
- Matt, G., Perola, G. C. & Piro, L., 1991. *Astr. Astrophys.*, **247**, 25.
- Miller, J. S. & Goodrich, R. W., 1990. *Astrophys. J.*, **355**, 456.
- Miller, J. S., Goodrich, R. W. & Mathews, W. G., 1991. *Astrophys. J.*, **378**, 47.
- Morini, M., Anselmo, F. & Molteni, D., 1989. *Astrophys. J.*, **347**, 750.
- Morrison, R. & McCammon, D., 1983. *Astrophys. J.*, **270**, 119.
- Morse, J. A., Wilson, A. S., Elvis, M. & Weaver, K. A., 1995. *Astrophys. J.*, **439**, 121.
- Mulchaey, J. S., Colbert, E., Wilson, A. S., Mushotzky, R. F. & Weaver, K. A., 1993. *Astrophys. J.*, **414**, 144.
- Mushotzky, R. F., Done, C. & Pounds, K. A., 1993. *Ann. Rev. Astron. Astrophys.*, **31**, 717.

- Mushotzky, R. F., 1982. *Astrophys. J.*, **256**, 92.
- Mushotzky, R. F., 1984. *Adv. Space Res.*, **3**, 10.
- Nandra, K. & Pounds, K. A., 1992. *Nature*, **359**, 215.
- Nandra, K. & Pounds, K. A., 1994. *Mon. Not. R. astr. Soc.*, **268**, 405.
- Nandra, K., George, I. M., Mushotsky, R. F., Turner, T. J. & Yaqoob, T., 1997. *Astrophys. J.*, **477**, 602.
- Netzer, H., 1993. *Astrophys. J.*, **411**, 594.
- Netzer, H., 1996. *Astrophys. J.*, **473**, 781.
- Ohashi, T. *et al.*, 1996. *Pub. Astr. Soc. Japan.*, **48**, 157.
- Osterbrock, D. E., 1989. *Astrophysics of Gaseous Nebulae and Active Galactic Nuclei*, University Science Books.
- Otani, C. *et al.*, 1996. *Pub. Astr. Soc. Japan.*, **48**, 211.
- Pan, H. C., Stewart, G. C. & Pounds, K. A., 1990. *Mon. Not. R. astr. Soc.*, **242**, 177.
- Peterson, B. M., 1997. *An introduction to active galactic nuclei*, Cambridge University Press.
- Pogge, R. W., 1988. *Astrophys. J.*, **328**, 519.
- Pounds, K. A., Warwick, R. S., Culhane, J. L. & De Korte, P. A. J., 1986. *Mon. Not. R. astr. Soc.*, **218**, 685.
- Pounds, K. A., Nandra, K., Stewart, G. C., George, I. M. & Fabian, A., 1990. *Nature*, **344**, 132.
- Rees, M. J., 1984. *Ann. Rev. Astron. Astrophys.*, **22**, 471.
- Reichert, G. A., Mushotzky, R. F. & Holt, S. S., 1986. *Astrophys. J.*, **303**, 87.
- Reynolds, C. S., Fabian, A. C., Nandra, K., Inoue, H., Kunieda, H. & Iwasawa, K., 1995. *Mon. Not. R. astr. Soc.*, **277**, 901.
- Reynolds, C. S., 1997. *Mon. Not. R. astr. Soc.*, **286**, 513.
- Ross, R. R., Fabian, A. C. & Young, A. J., 1999. *Mon. Not. R. astr. Soc.*, in press.

- Rush, B., Malkan, M. A. & Spinoglio, L., 1993. *Astrophys. J. Suppl.*, **89**, 1.
- Schmidt, G. D. & Miller, J. S., 1985. *Astrophys. J.*, **290**, 517.
- Shields, G. A., 1978. *Nature*, **272**, 706.
- Smith, D. A. & Done, C., 1996. *Mon. Not. R. astr. Soc.*, **280**, 355.
- Snowden, S. L., McCammon, D., Burrows, D. N. & Mendenhall, J. A., 1994. *Astrophys. J.*, **424**, 714.
- Stark, A. A., Gammie, C. F., Wilson, R. W., Bally, J., Linke, R. A., Heiles, C. & Hurwitz, M., 1992. *Astrophys. J. Suppl.*, **79**, 77.
- Storchi-Bergmann, T., Mulchaey, J. S. & Wilson, A. S., 1992. *Astrophys. J. Letts.*, **395**, 73.
- Sun, W. H. & Malkan, M. A., 1989. *Astrophys. J.*, **346**, 68.
- Sunyaev, R. A. & Titarchuk, L. G., 1980. *Astr. Astrophys.*, **86**, 121.
- Svensson, R., 1994. *Astrophys. J. Suppl.*, **92**, 585.
- Tanaka, Y. *et al.*, 1995. *Nature*, **375**, 659.
- Tanaka, Y., Inoue, H. & Holt, S. S., 1994. *Pub. Astr. Soc. Japan.*, **46**, L37.
- Taniguchi, Y. & Anabuki, N., 1999. *Astrophys. J. Letts.*, in press.
- Tran, H. D., Miller, J. S. & Kay, L. E., 1992. *Astrophys. J.*, **397**, 452.
- Tran, H. D., 1995. *Astrophys. J.*, **440**, 597.
- Tucker, W. H., 1975. *Radiation Processes in Astrophysics*, MIT Press.
- Turner, T. J. & Pounds, K. A., 1989. *Mon. Not. R. astr. Soc.*, **240**, 833.
- Turner, M. J. L. *et al.*, 1989. *Pub. Astr. Soc. Japan.*, **41**, 345.
- Turner, T. J., Weaver, K. A., Mushotzky, R. F., Holt, S. S. & Madejski, G. M., 1991. *Astrophys. J.*, **381**, 85.
- Turner, T. J., George, I. M., Nandra, K. & Mushotzky, R., 1997a. *Astrophys. J. Suppl.*, **113**, 23.

- Turner, T. J., George, I. M., Nandra, K. & Mushotzky, R., 1997b. *Astrophys. J.*, **488**, 164.
- Turner, T. J., Urry, C. M. & Mushotzky, R. F., 1993. *Astrophys. J.*, **418**, 653.
- Ueno, S., Mushotzky, R. F., Koyama, K., Iwasawa, K., Awaki, H. & Hayashi, I., 1994. *Pub. Astr. Soc. Japan.*, **46**, L71.
- Ulrich, M. H. *et al.*, 1984. *Mon. Not. R. astr. Soc.*, **206**, 221.
- Vaughan, S., Pounds, K. A., Reeves, J., Warwick, R. S. & Edelson, R., 1999. *Mon. Not. R. astr. Soc.*, in press.
- Ward, M. J., Wilson, A. S., Penston, M. V., Elvis, M., Maccacaro, T. & Tritton, K. P., 1978. *Astrophys. J.*, **223**, 788.
- Warwick, R. S., Done, C. & Smith, D. A., 1995. *Mon. Not. R. astr. Soc.*, **275**, 1003.
- Warwick, R. S., Sembay, S., Yaqoob, T., Maishima, K., Ohashi, T., Tashiro, M. & Kohmura, Y., 1993. *Mon. Not. R. astr. Soc.*, **265**, 412.
- Warwick, R. S. *et al.*, 1996. *Astrophys. J.*, **470**, 349.
- Warwick, R. S., Pounds, K. A. & Turner, T. J., 1988. *Mon. Not. R. astr. Soc.*, **231**, 1145.
- Weaver, K. A. *et al.*, 1992. *Astrophys. J. Letts.*, **401**, 11.
- Weaver, K. A. *et al.*, 1994a. *Astrophys. J.*, **423**, 621.
- Weaver, K. A., Yaqoob, T., Holt, S. S., Mushotzky, R. F., Matsuoka, M. & Yamauchi, M., 1994b. *Astrophys. J. Letts.*, **436**, 27.
- Wilson, A. S., Elvis, M., Lawrence, A. & Bland-Hawthorn, J., 1992. *Astrophys. J. Letts.*, **391**, 75.
- Xue, S. J., Otani, C., Mihara, T., Cappi, M. & Matsuoka, M., 1999. *Pub. Astr. Soc. Japan.*, **50**, 519.
- Yaqoob, T. & Warwick, R. S., 1991. *Mon. Not. R. astr. Soc.*, **248**, 773.
- Yaqoob, T., Warwick, R. S., Makino, F., Otani, C., Sokoloski, J. L., Bond, I. A. & Yamauchi, M., 1993. *Mon. Not. R. astr. Soc.*, **262**, 435.

Yaqoob, T., Edelson, R., Weaver, K. A., Warwick, R. S., Mushotzky, R. F., Serlemitsos, P. J. & Holt, S. S., 1995. *Astrophys. J. Letts.*, **453**, 81.

Yaqoob, T., Warwick, R. S. & Pounds, K. A., 1989. *Mon. Not. R. astr. Soc.*, **236**, 153.

Zdziarski, A. A., Ghisellini, G., George, I. M., Svensson, R., Fabian, A. C. & Done, C., 1990. *Astrophys. J. Letts.*, **363**, 1.

Zdziarski, A. A., Johnson, W. N., Done, C., Smith, D. & Naron-Brown, K. M., 1995. *Astrophys. J. Letts.*, **438**, 63.

Zdziarski, A. A., Lightman, A. P. & Maciołek-Niedźwiecki, A., 1993. *Astrophys. J. Letts.*, **414**, 93.